

國立交通大學

電信工程學系

博士論文

頻寬-空間-極化於寬頻多輸入多輸出無線電  
通道影響之研究

Effects of Bandwidth-Space-Polarization on  
UWB/Wideband Multiple-Input Multiple-Output  
Channels

研究生：張維儒

指導教授：唐震寰 博士

中華民國九十七年六月

頻寬-空間-極化於寬頻多輸入多輸出無線電  
通道影響之研究

Effects of Bandwidth-Space-Polarization on  
UWB/Wideband Multiple-Input  
Multiple-Output Channels

研究生：張維儒  
指導教授：唐震寰 博士

Student: Wei-Ju Chang  
Advisor: Dr. Jenn-Hwan Tarnng



A Dissertation  
Submitted to Institute of Communication Engineering  
College of Electrical and Computer Engineering  
National Chiao Tung University  
in Partial Fulfillment of the Requirements  
for the Degree of Doctor of Philosophy  
in  
Communication Engineering  
Hsinchu, Taiwan

2008 年 6 月

# 頻寬-空間-極化於寬頻多輸入多輸出無線電 通道影響之研究

研究生：張維儒

指導教授：唐震寰 博士

國立交通大學電信工程學系

## 中文摘要

為滿足下一代(B3G)無線通信系統的高傳輸速率需求，使用高頻寬並搭配多輸入多輸出(MIMO)天線技術是未來無線通信系統的發展趨勢，而其通道特性的掌握與適當模型的建構更是 B3G 無線通信系統發展之初的首要課題。

對寬頻 MIMO 通道而言，頻寬、天線間距及天線極化是影響其通道模型參數的主要因素。頻寬的增加代表系統時間解析度變好，多路徑延遲(multipath delay)及群聚(clustering)現象越明顯，窄頻之多路徑延遲模型必須修正以滿足寬頻系統通道之需求；而在多天線部份，除空間天線陣列架構外，極化天線的應用有助於在無線終端設備上實現多天線架構，因此，完整考量 Space-Polarization 相關性的 MIMO 通道模型，是 MIMO 技術設計發展所必需。

本論文完整探討 Bandwidth-Space-Polarization 對寬頻 MIMO 通道之影響，發展一創新之寬頻通道模型參數預估方法，可由窄頻通道模型參數預估寬頻通道參數模型。另外吾人也針對室內環境，發展三維空間幾何散射模型，該模型結合幾何圓模型與幾何橢圓模型之概念並將之拓展至三維空間，可用以模擬空間/極化陣列天線 MIMO 通道的相關性。除此，吾人也透過實測數據分析，探討 UWB-MIMO 於身域環境(BAN)之效能。本研究所發展之寬頻通道模型參數預估方法與 MIMO 通道相關性模型，皆經由實測數據分析獲得驗證，實測環境包含室外寬頻(120 MHz)、室內及身域環境之超寬頻(3-10 GHz 頻段)通道量測，完全符合下一代無線通信系統之需求。



# Effects of Bandwidth-Space-Polarization on UWB/Wideband Multiple-Input Multiple-Output Channels

Student: Wei-Ju Chang

Advisor: Dr. Jenn-Hwan Tarn

Institute of Communication Engineering  
National Chiao Tung University



To achieve high data rate requirements of systems beyond 3rd generation (B3G), development and standardization of enhanced radio access technologies with wide bandwidth and multiple-input multiple-output (MIMO) antennas are sustained. In wireless communication systems, radio channels play an important role on system performance. Therefore, a through understanding of wideband MIMO channel characteristics is essential for B3G wireless systems developing and realization.

Compared to traditional narrowband single-input single-output (SISO) channels, bandwidth, array spacing and antenna polarization effects should be taking into account in the models of wideband MIMO channels. For systems with larger bandwidth, it is possible

to observe more multipath components, and therefore stronger clustering effects due to its better time resolution. For MIMO systems, in addition to spatial arrays, the utilization of polar arrays is of great interest recently due to its benefit to the device compactness. Therefore, a complete MIMO channel model should include the space factor as well as the polarization factors.

In this research, effects of bandwidth-space-polarization on UWB/wideband MIMO channels are investigated. Here, a novel method for wideband model parameters estimation is developed. Through this method, the model parameters of a wideband signal can be determined from those of a narrowband signal. Furthermore, a three-dimensional Geometrically Based Single Bounce Model (3D GBSBM), is proposed for indoor wideband MIMO channel correlation modeling. This model is extended from a 2D model, which combines the concept of the Geometrically Based Single Bounce Circle Model (GBSBCM) and the Geometrically Based Single Bounce Ellipse Model (GBSBEM). In this model, the effect of 3D multipath on sub-channel correlation of the spatial/polar arrays is taken into account. Finally, the performance of UWB-MIMO for body area networks (BANs) is investigated through channel measurements.

The newly developed method and models are validated by broadband channel (120-MHz bandwidth) measurements in outdoors as well as ultra-wideband channels (3-10 GHz) in indoors and BANs, which is agreeable to the requirements of B3G systems.

# 誌 謝

本論文得以順利完成，有賴生命中許許多多貴人的指導、協助、包容與相伴，於此，以感恩之心，謹將此論文獻給您們！

首先，我要以最誠摯的敬意感謝我的指導老師 唐震寰教授，承蒙老師自大學、碩士至博士多年來的指導，讓我在無線電傳播的專業知識領域多有成長，並能在相關研究上有所突破，老師嚴謹認真的治學精神與謙沖的待人處事態度更是學生的典範。

其次，本論文相關研究工作得以順利進行，也有賴實驗室瑞榮學長的指導，以及學弟妹豐誠、鳴君、孟勳、思云等人的共同努力，感謝他們。當然，也要特別感謝梁小姐麗君多年來在各項事務上的熱心協助。

另外，也要感謝本論文的口試委員李大嵩教授、李學智教授、張道治教授、彭松村教授、楊成發教授，能在百忙當中撥冗費心審查，對論文內容提出懇切的意見與指導，讓本論文能更臻完善。

於此，也要特別感謝陳榮義主任的提攜與推薦，讓我有機會完成博士學位的進修。計畫主管與同事在工作上給予的包容與協助，我更是銘感於心，每位同事的專業素養，也讓我在通訊知識上能不斷成長。

最後，我要將此喜悅與我最親愛的家人分享。母親自小全心全意的照顧與教誨，讓我能以樂觀進取之心平順克服學業與職場的挑戰，而我親愛的老婆欣怡與女兒詠瑜，更是我精神上最大的支柱，有妳們陪伴的每一天，生活中總是歡樂喜悅與滿滿的幸福，我愛妳們也謝謝妳們。

# Contents

中文摘要 .....	III
Abstract .....	V
誌 謝 .....	VII
Contents.....	VIII
List of Tables.....	X
List of Figures .....	XI
Abbreviations.....	XV
<b>Chapter 1 Introduction .....</b>	<b>1</b>
1.1 Motivation and Contributions .....	2
1.2 Thesis Overview .....	5
<b>Chapter 2 Overview of Channel Models for B3G Systems.....</b>	<b>7</b>
2.1 Introduction.....	8
2.2 Multipath models for wideband channels .....	10
2.2.1 $\Delta$ -K model .....	11
2.2.2 Saleh-Valenzuela model .....	13
2.3 Spatial channel models .....	16
2.3.1 Overview of Developed Spatial Channel Models .....	16
2.3.2 MIMO Channel Models in Standards.....	22
<b>Chapter 3 Measurement and Modeling of Wideband SISO Channels .....</b>	<b>32</b>
3.1 Introduction.....	33
3.2 A novel method for wideband model parameter estimation .....	34
3.2.1 Bandwidth on observable multipath-clustering.....	35
3.2.2 Bandwidth on multipath power decay and amplitude fading.....	39
3.3 Measurement setup and environments.....	44
3.3.1 Outdoor environments .....	44
3.3.2 Indoor environments.....	47



3.4 Validation and Discussions .....	50
3.4.1 Measurement data processing and analysis.....	50
3.4.2 Validation Results.....	54
3.5 Summary.....	68
<b>Chapter 4 Measurement and Modeling of Space Correlation for Indoor Wideband MIMO Channels.....</b>	<b>69</b>
4.1 Introduction.....	70
4.2 A New Model for Wideband MIMO Channel Correlation.....	72
4.2.1 3D Geometrically Based Single Bounce Model.....	74
4.2.2 Space Correlation of Spatial/Polar Arrays.....	78
4.3 Measurement and Validation.....	87
4.3.1 Measurement Setup and Environment .....	87
4.3.2 Validation and Discussions.....	90
4.4 Summary.....	95
<b>Chapter 5 Measurements and Analysis of UWB MIMO Performance for Body Area Network Applications.....</b>	<b>96</b>
5.1 Introduction.....	97
5.2 Measurement Setup and Sites.....	99
5.3 Observations and Discussions.....	103
5.3.1 Effect of Propagation Condition.....	104
5.3.2 Effect of Bandwidth .....	105
5.3.3 Effect of Array Spacing.....	107
5.3.4 Effect of Antenna Polarization .....	110
5.4 Summary.....	113
<b>Chapter 6 Conclusions .....</b>	<b>114</b>
<b>References .....</b>	<b>118</b>
<b>Author's Publications (2003~2008).....</b>	<b>122</b>

# List of Tables

## Chapter 2 Overview of Channel Models for B3G Systems.....7

Table 2-1	The channel parameters of 3GPP SCM for link level simulations.....	28
Table 2-2	The channel parameters of 3GPP SCM for system level simulations...	29
Table 2-3	Sub-paths to mid-paths assignment and resulting angle spread in 3GPP SCME.....	30

## Chapter 3 Measurement and Modeling of Wideband SISO Channels.....32

Table 3-1	Setup and environments for the broadband outdoor channel measurements.....	46
Table 3-2	Values of $m_{e-\lambda}$ , $\sigma_{e-\lambda}$ , $m_{e-P}$ and $\sigma_{e-P}$ for $n=2$ .....	61
Table 3-3	Values of $m_{e-\lambda}$ , $\sigma_{e-\lambda}$ , $m_{e-P}$ and $\sigma_{e-P}$ for $n=4$ .....	61
Table 3-4	Values of measured and computed $NP_{20dB}$ .....	62



# List of Figures

<b>Chapter 1 Introduction.....</b>	<b>1</b>
Fig. 1-1 A diagram of 3GPP standard evolution.....	4
<b>Chapter 2 Overview of Channel Models for B3G Systems.....</b>	<b>7</b>
Fig. 2-1 The illustration of the $\Delta$ - $K$ process.....	13
Fig. 2-2 The illustration of exponential decay of mean cluster power and ray power within clusters.....	15
Fig. 2-3 The illustration of the geometry of Lee's model.....	17
Fig. 2-4 The illustration of the geometry of GBSBCM.....	18
Fig. 2-5 The illustration of the geometry of GBSBEM.....	20
Fig. 2-6 The illustration of the procedure for generating MIMO channels.....	30
Fig. 2-7 The illustration of multipath angle parameters at BS and MS sides.....	31
Fig. 2-8 A diagram of the mid-path approach of SCME.....	31
<b>Chapter 3 Measurement and Modeling of Wideband SISO Channels.....</b>	<b>32</b>
Fig. 3-1 A diagram for bandwidth effect on the observed multipath propagation channels.....	34
Fig. 3-2 A diagram for the arrival of multipath when bandwidth changes from $F$ to $f$ for $n=2$ .....	38
Fig. 3-3 The averaged power delay profile of a 500 MHz-bandwidth UWB signal at an indoor environment and under NLOS condition. The wavy line shows the measured profile. The straight line, which is obtained by a best-fit procedure, represents an exponential decay line.....	40
Fig. 3-4 Rician factors of the first 15 bins of each measured point at indoor environments with 2-GHz bandwidth are shown. The total numbers of measured points are 24.....	41
Fig. 3-5 System diagram of the RUSK wideband vector channel sounder.....	45

Fig. 3-6	Schematic diagram of the UWB indoor channel measurement system.....	49
Fig. 3-7	Layouts of four sites where the UWB indoor channel measurements were performed. Locations of the transmitter (Tx) and the receiver are shown by “★” and “●”, respectively.....	49
Fig. 3-8	Comparisons of the measured and computed results of (a) the path arrival rate $\lambda_i$ ; and (b) the path occurrence probability $P_i$ of “Urban 1” site with 60-MHz bandwidth for $n=2$ .....	58
Fig. 3-9	Comparisons of the measured and computed results of (a) the path arrival rate $\lambda_i$ ; (b) the path occurrence probability $P_i$ of “Indoor NLOS” site with 1 GHz bandwidth for $n=2$ .....	59
Fig. 3-10	Comparisons of the measured and computed results of (a) the path arrival rate $\lambda_i$ ; (b) the path occurrence probability $P_i$ of “Urban 1” site with 120 MHz bandwidth for $n=4$ .....	60
Fig. 3-11	The measured $k_i$ of “Indoor NLOS” site with 1 GHz bandwidth.....	62
Fig. 3-12	$\bar{K}$ value of the measurement sites: (a) outdoor environments; and (b) indoor environments.....	63
Fig. 3-13	Decay constant versus measured point number for signal bandwidths of 500MHz, 1GHz, and 2GHz at “Indoor LOS” and “Indoor NLOS” sites...	65
Fig. 3-14	Power ratio versus measured point number for signal bandwidths of 500 MHz, 1GHz, and 2GHz at “Indoor LOS” and “Indoor NLOS” sites.....	66
Fig. 3-15	Comparisons between the measured and computed results of the power ratio for all measured points at “Indoor LOS” and “Indoor NLOS” sites with 1GHz bandwidth.....	66
Fig. 3-16	Rician factor versus measured point number for signal bandwidths of 500MHz, 1GHz, and 2GHz at “Indoor LOS” and “Indoor NLOS” sites...	67
Fig. 3-17	Comparisons between the measured and computed results of the Rician factor for all measured points at “Indoor LOS” and “Indoor NLOS” sites with 1GHz bandwidth.....	67

**Chapter 4 Measurement and Modeling of Space Correlation for Indoor Wideband MIMO Channels..... 69**

Fig. 4-1	Per tap MIMO correlation metrics.....	73
Fig. 4-2	The illustration of the geometry of the 3D GBSBEM.....	76
Fig. 4-3	The geometry for the scatter region of different taps.....	77
Fig. 4-4	The illustration of the geometry of the 3D GBSBM for the 1 <sup>st</sup> tap: (a) the effective scatter region; (b) the effective scatterers.....	77
Fig. 4-5	The illustration of the geometry of the 3D GBSBM for the 2nd tap: (a) the effective scatter region; (b) the effective scatterers.....	78
Fig. 4-6	The geometrical configuration of a 1-by-2 channel of the 3D GBSBM....	84
Fig. 4-7	The illustration of the 3D GBSBM in cylindrical coordinates.....	85
Fig. 4-8	The illustration of the 3D GBSBM for the $n^{\text{th}}$ tap.....	85
Fig. 4-9	The simulated spatial correlation of the co-polarized antenna case based on the 2D GBSBM.....	86
Fig. 4-10	The simulated spatial correlation of the co-polarized antenna case based on the 3D GBSBM for the 1 <sup>st</sup> tap.....	86
Fig. 4-11	The simulated spatial correlation of the cross-polarized antenna case based on the 3D GBSBM for the 1 <sup>st</sup> tap.....	87
Fig. 4-12	The simulated spatial correlation of the cross-polarized antenna case based on the 3D GBSBM for the 5 <sup>th</sup> tap.....	87
Fig. 4-13	Layouts of the wideband MIMO channel measurement site.....	89
Fig. 4-14	The virtual antenna array configuration for MIMO channel measurements.....	90
Fig. 4-15	The measured and fitted CDFs of the normalized power of the 1 <sup>st</sup> tap.....	92
Fig. 4-16	The measured and fitted CDFs of the normalized power of the 2 <sup>nd</sup> tap.....	92
Fig. 4-17	The measured and simulated space correlation of the 1 <sup>st</sup> tap for co-polarized antenna case.....	93
Fig. 4-18	The measured and simulated space correlation of the 2 <sup>nd</sup> tap for co-polarized antenna case.....	93
Fig. 4-19	The measured and simulated space correlation of the 1 <sup>st</sup> tap for cross-polarized antenna case.....	94
Fig. 4-20	The measured and simulated space correlation of the 2nd tap for cross-polarized antenna case.....	94

**Chapter 5 Measurements and Analysis of UWB MIMO Performance for  
Body Area Network Applications.....96**

Fig. 5-1 Measured antenna return loss versus frequency.....101

Fig. 5-2 The locations of Tx and Rx antennas for MIMO measurements.....101

Fig. 5-3 Floor layouts of measurement sites. (a) Sites A and B; (b) Site C.....102

Fig. 5-4 The measured 2x2 MIMO channel capacity at different sites for frequency band of 3-10 GHz.....105

Fig. 5-5 The measured 2x2 MIMO channel capacity at site C.....106

Fig. 5-6 One sub-channel frequency response at Site C.....106

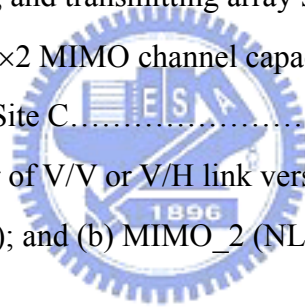
Fig. 5-7 MIMO channel capacities versus receiving array spacing at Site A.....108

Fig. 5-8 Spatial correlation coefficients versus receiving array spacing at Site A..109

Fig. 5-9 Maximum value of the power differences between any two sub-channels versus receiving and transmitting array spacing at Site A.....109

Fig. 5-10 The measured 2x2 MIMO channel capacity of the polar array and the spatial array at Site C.....111

Fig. 5-11 Received power of V/V or V/H link versus frequency at Site C for (a) MIMO\_1 (LOS); and (b) MIMO\_2 (NLOS).....112



## Abbreviations

Abbreviation	Description
3G	third generation
3GPP	3 <sup>rd</sup> generation partnership project
3GPP2	3 <sup>rd</sup> generation partnership project 2
AoA	angle of arrival
AoD	angle of departure
aPDP	averaged power delay profile
AS	angle spread
B3G	beyond third generation
BAN	body area network
BS	base station
DS	delay spread
GBSBM	geometrically based single bounce model
GBSBCM	geometrically based single bounce circular model
GBSBEM	geometrically based single bounce ellipse model
HSDPA	high speed downlink packet access
IFFT	inverse fast Fourier transform
i.i.d.	independently and identically distributed
iPDP	instantaneous power delay profile
ISI	inter-symbol interference
LOS	line-of-sight
LTE	long-term evolution
METRA	multi-element transmit receive antennas
MIMO	multiple-input multiple-output
MPC	multipath component
MS	mobile station
NLOS	non line-of-sight
PAS	power azimuth spectrum

PDF	probability density function
PDP	power delay profile
S-V	Saleh-Valenzuela
SCM	spatial channel model
SCME	spatial channel model extension
SF	shadow fading
SISO	single-input single-output
SNR	signal-to-noise ratio
TDL	tapped-delay-line
TOA	time of arrival
ULA	uniform linear array
UWB	ultra-wideband
VAN	vector network analyzer
WAN	wide area network
WLAN	wireless local area network





---

# Chapter 1 Introduction

In this chapter, the motivation and contributions of this research and the overview of this thesis are presented.



---

## 1.1 Motivation and Contributions

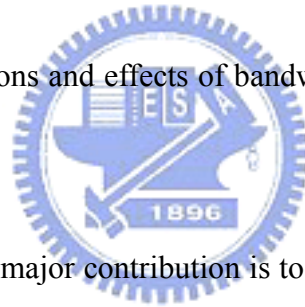
Recently, systems beyond 3G (B3G) have been actively discussed in various forum and organizations. According to the ITU-R preliminary recommendation [1], new radio interfaces of B3G systems will support high data rate transmissions up to approximately 100 Mbps for high mobility and 1 Gbps for low mobility, respectively. To achieve the high data rate requirements, standardization and development of enhanced radio access technologies with wide bandwidth and multiple antennas are sustained.

For instance, 3GPP is in the process of defining the long-term evolution (LTE) [2] and LTE-Advanced for B3G services. Fig. 1-1 shows the evolution path of 3GPP standards. Compared to the high-speed downlink packet access (HSDPA) [3] that introduced in 3GPP release 5, LTE improves the downlink peak data rate from 14.4 Mbps to approximately 300 Mbps by using 4×4 multiple-input multiple-output (MIMO) antenna technologies along with a wide bandwidth of 20 MHz, which is four times the bandwidth of HSDPA. In addition to that, to meet the 1-Gbps peak data rate requirements of B3G systems, 3GPP begins to process the feasibility studies of technologies using 8×8 MIMO along with a bandwidth of 40 MHz. Furthermore, for short-range communications, ultra-wideband (UWB) radio technology has attracted great interest in commercial and military sectors due to its potential strength to provide high channel capacity with an extreme wide

---

transmission bandwidth of 500 MHz at least [4].

The performance of wireless communications is greatly influenced by the radio propagation channels. Consequently, a thorough understanding of UWB/wideband MIMO channel characterizations is essential for the realization of B3G systems. To model UWB/wideband MIMO channels, the statistical properties in frequency (bandwidth) and spatial domains have to be carefully investigated. Furthermore, cross-polarized antennas are of interest for MIMO applications due to its potential benefit for the device compactness. Therefore, a complete investigation of UWB/wideband MIMO channels should cover the characterizations and effects of bandwidth, space and polarization, which is also the goal of this research.



For bandwidth effect, our major contribution is to develop a novel method to estimate the model parameters of a wideband signal from those of a narrowband signal. Through this approach, the proper model parameters for B3G systems can be determined from those of current models of 3G systems, which support system bandwidth up to 5 MHz. Furthermore, for space and polarization effect on MIMO channels, a three-dimensional Geometrically Based Single Bounce Model (3D GBSBM) is proposed for the space correlation modeling of indoor wideband MIMO channels. This model is extended from a 2D model, which combines the concept of the Geometrically Based Single Bounce Circle Model (GBSBCM) and the Geometrically Based Single Bounce Ellipse Model (GBSBEM).

---

In this model, the effect of 3D multipath on sub-channel correlation of the spatial/polar arrays is taken into account.

Finally, UWB-MIMO performance in body area networks (BAN) is investigated through channel measurements. It is found that in BAN the MIMO channel capacity is mainly determined by the power imbalance between sub-channels compared to the sub-channel correlation for spatial arrays, which is different from that in wide-area networks (WAN) and wireless local area networks (WLAN).

In this research, the newly developed method and models are validated by extensive broadband channel (120-MHz bandwidth) measurements in outdoors as well as UWB channels (3-10 GHz) in indoors and BANs, which is agreeable to the requirements of B3G systems.

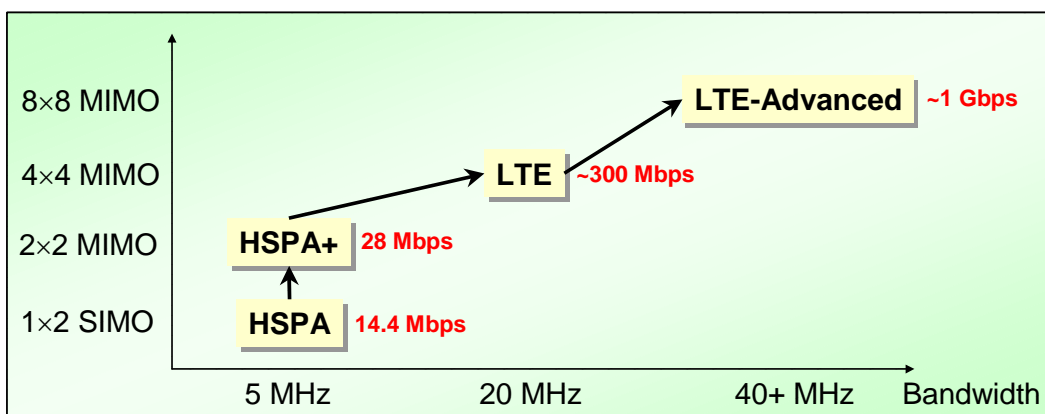
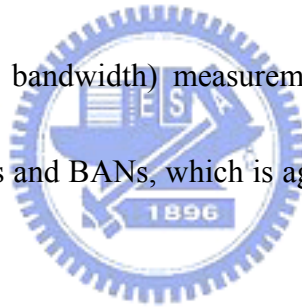


**Fig. 1-1 A diagram of 3GPP standard evolution.**

---

## 1.2 Thesis Overview

In Chapter 2, some of the well-known models for wideband multipath delay propagations and for MIMO channels are introduced. For UWB/wideband propagations, multipath arrivals in cluster rather than in continuum as is customary for narrowband channels. The  $\Delta$ - $K$  model [5] and the Saleh-Valenzuela (S-V) model [6] are two well-recognized models to characterize the multipath-clustering phenomenon in delay domain. For MIMO channels, correlation between sub-channels, which is dependent on the multipath power-angle spectrum and array architecture, is significant to MIMO channel capacity. The spatial channel models proposed in IEEE 802.11n [7] and 3GPP/3GPP2 [8] are two representative models for MIMO channels in indoor and cellular environments, respectively.

In Chapter 3, measurement and modeling of UWB/wideband multipath channels for single-input single-output (SISO) is described. Here, a novel method is proposed to estimate the model parameters of a wideband signal from those of a narrowband signal. Through this approach, effect of bandwidth on the observable multipath-clustering is explored. Our proposed method is extensively validated by measured channels of 1.95 GHz and 2.44 GHz broadband radios in metropolitan and suburban areas, and of 3-5 GHz UWB signals in indoors.

---

In Chapter 4, a newly developed 3D GBSBM for indoor environments is introduced. Based on this model, we derived the correlation between MIMO sub-channels of spatial/polar arrays and discuss its sensitivity to a variety of different azimuth and elevation angle spreads. By combining this 3D GBSBM scattering model with the deterministic rays, site-specific indoor MIMO channels are well modeled.

In Chapter 5, the performance of UWB-MIMO applications in BANs is presented. Here, the effects of bandwidth, array spacing, and antenna polarization on UWB-MIMO channel capacity are experimentally investigated and discussed.

Finally, conclusions of this thesis are presented in Chapter 6.



---

# **Chapter 2 Overview of Channel Models for B3G Systems**



**In this chapter, first the well-known models for multipath-clustering are introduced. Then some MIMO channel models presented in literature and standards are introduced.**

---

## 2.1 Introduction

Because of multipath propagation due to reflections, refractions, and/or scattering by obstacles or scatters in propagation environments, radio propagation channels are usually modeled as a linear filter with a complex-valued lowpass equivalent impulse response that is expressed as

$$h(\tau) = \sum_k a_k \delta(\tau - \tau_k) \quad (2-1)$$

where  $a_k$  and  $\tau_k$  are the random complex-valued path gain and propagation delay of the multipath components (MPCs), respectively; and  $\delta$  is the Dirac delta function. However, in practice, bandwidth of a signal is finite consequently the multipath resolution duration is nonzero and is equal to the reciprocal of the signal bandwidth. Therefore, the number of resolved multipath and its path gain is dependent on signal bandwidth.

In addition to the time dispersion phenomenon, angular dispersion effects are described by the double-directional channel impulse response [9]

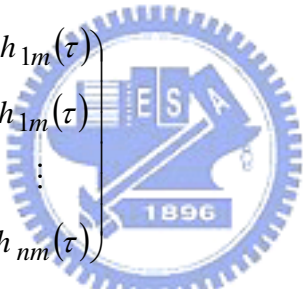
$$h(\tau, \phi, \psi) = \sum_l a_l \delta(\tau - \tau_l) \delta(\phi - \phi_l) \delta(\psi - \psi_l) \quad (2-2)$$

where,  $a_l$ ,  $\tau_l$ ,  $\phi_l$  and  $\psi_l$  denoting the complex amplitude, the excess delay, the angle of



departure (AoD) and the angle of arrival (AoA), respectively. It is noted that the double-directional channel impulse response describes only the propagation channel and is thus independent of antenna.

For MIMO systems, the channel response has to be described for all transmit and receive antenna pairs. Let us consider MIMO system with  $m$  transmit antennas and  $n$  receive antennas, then the time-invariant MIMO channel is represented by a  $n \times m$  channel matrix:

$$\mathbf{H}(\tau) = \begin{pmatrix} h_{11}(\tau) & h_{12}(\tau) & \dots & h_{1m}(\tau) \\ h_{21}(\tau) & h_{22}(\tau) & \dots & h_{2m}(\tau) \\ \vdots & \vdots & \ddots & \vdots \\ h_{n1}(\tau) & h_{n2}(\tau) & \dots & h_{nm}(\tau) \end{pmatrix} \quad (2-3)$$


where,  $h_{ij}(\tau)$  denote the impulse response between the  $j$ th transmit antenna and the  $i$ th receive antenna. It is noted that  $h_{ij}(\tau)$  includes the effects of propagation channel and antennas. The relationship between  $h_{ij}(\tau)$  in (2-3) and  $h(\tau, \phi, \psi)$  in (2-2) is shown as

$$h_{ij}(\tau) = \int_{\phi} \int_{\psi} h(\mathbf{r}_{\text{Tx}}^{(j)}, \mathbf{r}_{\text{Rx}}^{(i)}, \tau, \phi, \psi) G_{\text{Tx}}(\phi) G_{\text{Rx}}(\psi) d\phi d\psi \quad (2-4)$$

where,  $\mathbf{r}_{\text{Tx}}^{(j)}$  and  $\mathbf{r}_{\text{Rx}}^{(i)}$  are the coordinates of the  $j$ th transmit and  $i$ th receive antenna, respectively. Furthermore,  $G_{\text{Tx}}(\phi)$  and  $G_{\text{Rx}}(\psi)$  represent the transmit and receive antenna

pattern, respectively.

For cross-polarized antenna applications, the polarization can be take into account by extending the impulse response to a polarimetric (2×2) matrix [10] that describes the coupling between vertical (V) and horizontal (H) polarizations:

$$\begin{aligned} \mathbf{H}_{\text{pol}}(\tau, \phi, \psi) &= \begin{pmatrix} h^{VV}(\tau, \phi, \psi) & h^{VH}(\tau, \phi, \psi) \\ h^{HV}(\tau, \phi, \psi) & h^{HH}(\tau, \phi, \psi) \end{pmatrix} \\ &= \sum_l \begin{pmatrix} a_l^{VV} & a_l^{VH} \\ a_l^{HV} & a_l^{HH} \end{pmatrix} \delta(\tau - \tau_l) \delta(\phi - \phi_l) \delta(\psi - \psi_l) \end{aligned} \quad (2-5)$$

From (2-4) and (2-5), it is found that the bandwidth, array spacing and antenna polarization effects should be taking into account in the modeling of wideband MIMO channels.

## 2.2 Multipath models for wideband channels

For narrowband/wideband radio channels, the tapped-delay-line (TDL) model is a well-recognized model for multipath delay propagations. In this model, the axis of excess delay times is partitioned into bins and the bin width is equal to the reciprocal of the signal bandwidth. It assumes multipath arrive at every bins with average power profile that decays exponentially.

---

Multipath-clustering, the phenomenon that multipath arrivals in cluster, has been found in outdoor broadband channels as well as in indoor UWB channels [5-6, 11-16]. It is caused by the fact that scatterers tend to group together in realistic environments and are resolved in groups by the system with fine or very fine time resolution. Modeling of this phenomenon helps the design of an equalizer or Rake receiver, such as design of equalizers with unequal tap spacing or design of a selective Rake receiver and partial Rake receivers [12]. In addition, in [17], it shows that unclustered models tend to overestimate the channel capacity as comparing with the case that multipath components are indeed clustered. Here, two well-recognized models to characterize the multipath-clustering phenomenon, the  $\Delta$ - $K$  model and the S-V model, are introduced.



### **2.2.1 $\Delta$ - $K$ model**

The  $\Delta$ - $K$  model is initiated by Turin et al. [18], [19] and developed by Suzuki [5] to describe the ToAs of MPCs by taking multipath-clustering into account. In the model, the axis of excess delay times (relative to the propagation delay of the direct path between transmitting and receiving antennas) is partitioned into bins with width  $\Delta$  [5]. The probability of having a path in bin  $i$  is a function of whether or not an arrival occurred in the previous bin, and is a function of the empirical probability of path occurrences at different delays, which is based on measurements. It can be stated as the branching process

---

of Fig. 2-1: the probability of having a path in bin  $i$  is equal to  $\lambda_i$  if there is no path in the  $(i-1)^{\text{st}}$  bin; otherwise, it is increased by a factor  $K$  due to multipath-clustering effect. Note that, both the path occurrence probabilities,  $\lambda_i$  and  $K \cdot \lambda_i$ , are equal to or less than 1. When  $K > 1$ , the process exhibits a clustering property and large  $K$  represents a large clustering effect. For  $K=1$ , this process reverts to a standard Poisson process.

It is noted that this model is applicable upon replacing  $K$  by  $k_i$ , which is a function of the bin number  $i$  [5, 20-21]. From the branching process shown in Fig. 2-1 with replacing  $K$  by  $k_i$ , it is found that,  $P_i$ , the probability of having a path in bin  $i$ , is equal to the sum of the probabilities  $(1-P_{i-1}) \cdot \lambda_i$  and  $P_{i-1} \cdot k_i \cdot \lambda_i$ . After some derivations,  $\lambda_i$  is given as

$$\lambda_i = \frac{P_i}{(k_i - 1) \cdot P_{i-1} + 1}, \quad i \geq 2 \quad (2-6)$$

where  $\lambda_1 = P_1$ .

It is noted that  $\Delta$  is a model parameter to be chosen [5,18]. However, according to the assumption in these papers that each bin contains either one path or no path, it is reasonable to set  $\Delta$  as the signal time resolution, which is reciprocal of the signal bandwidth, of the specific radio system [11, 21-22]. This is because two or more paths arriving within the same time resolution interval cannot be resolved as distinct paths for a band-limited radio system [11]. Based on this fact, it is expected that systems with different

bandwidths may observe different multipath-clustering phenomenon and yield different channel model parameters for a specific environment because that the number of resolvable MPCs and clusters are changed with signal time resolution.

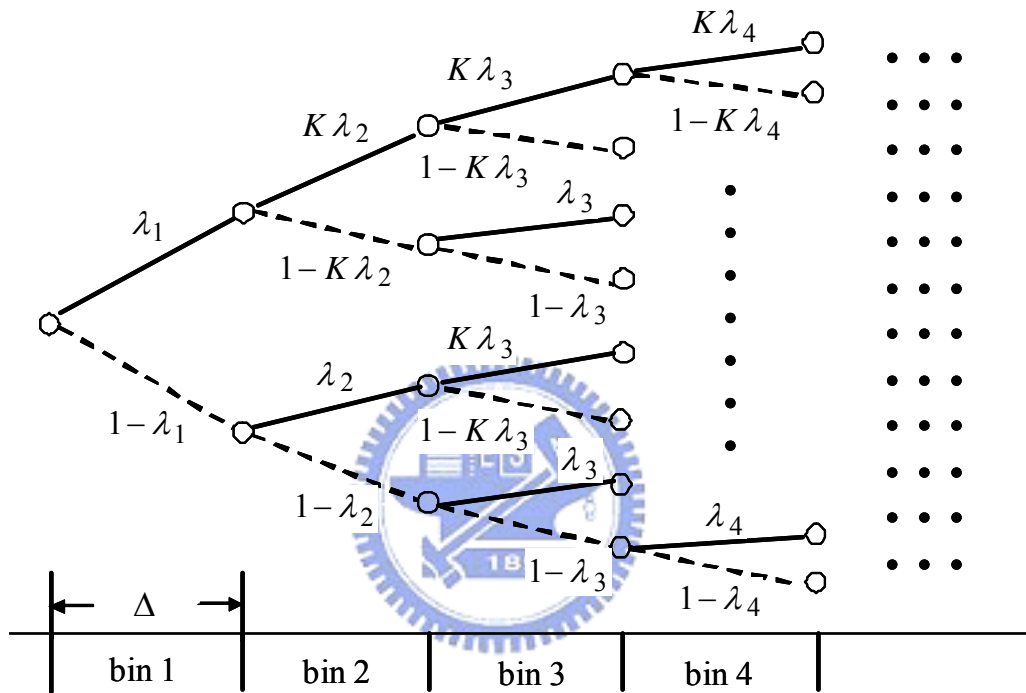


Fig. 2-1 The illustration of the  $\Delta$ - $K$  process.

### 2.2.2 Saleh-Valenzuela model

The S-V model was introduced first by Saleh-Valenzuela [6] to characterize the multipath-clustering phenomenon, and later verified, extended, and elaborated upon by many other researchers in [14-15]. The major difference between S-V model and Tapped-delay-line model is that S-V model doesn't assume the arrival of paths on each

---

time interval. Instead, two Poisson models are employed in the modeling of the arrival time.

The first Poisson model is for the first path of each path cluster and the second Poisson model is for the paths (or rays) within each cluster. Following the terminology in [6], we define

$T_l$  = the arrival time of the first path of the  $l$ -th cluster;

$\tau_{k,l}$  = the delay of the  $k$ -th path within the  $l$ -th cluster relative to the first path arrival time,  $T_l$ ;

$\Lambda$  = cluster arrival rate;

$\lambda$  = ray arrival rate, i.e., the arrival rate of path within each cluster.

By definition, we have  $\tau_{0l} = T_l$ . The distribution of cluster arrival time and the ray arrival time are given by (2-2) and (2-3), respectively

$$p(T_l|T_{l-1}) = \Lambda \exp[-\Lambda(T_l - T_{l-1})], \quad l > 0 \quad (2-7)$$

$$p(\tau_{k,l}|\tau_{(k-1),l}) = \lambda \exp[-\lambda(\tau_{k,l} - \tau_{(k-1),l})], \quad k > 0 \quad (2-8)$$

The magnitude of the  $k$ -th path within the  $l$ -th cluster is denoted by  $\beta_{kl}$ . It is Rayleigh distributed with a mean given by

$$\overline{\beta_{k,l}^2} = \overline{\beta^2(0,0)} \exp(-T_l/\Gamma) \exp(-\tau_{k,l}/\gamma) \quad (2-9)$$

---

where  $\Gamma$  and  $\gamma$  are the cluster and ray decay constants, respectively.  $\overline{\beta^2(0,0)}$  is the average power of the first arrival of the first cluster. Illustrations of the double exponential decay model in Fig. 2-2.

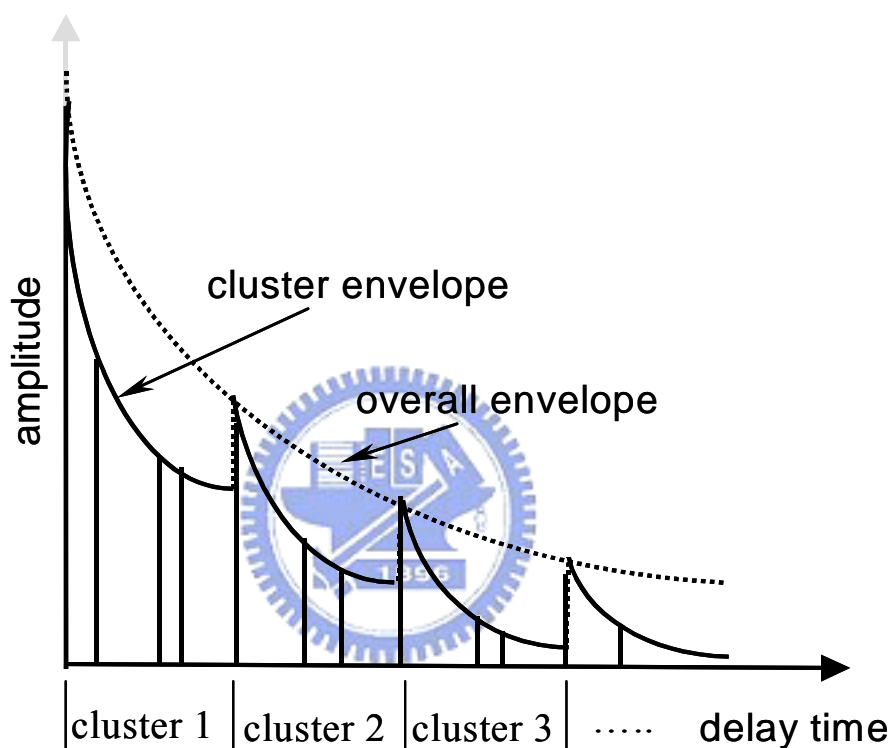


**Fig. 2-2** The illustration of exponential decay of mean cluster power and ray power within clusters.

---

## 2.3 Spatial channel models

### 2.3.1 Overview of Developed Spatial Channel Models

#### A. *Ray tracing models*

In the past few years, a deterministic model, called ray tracing, has been proposed based on the geometric theory and reflection and diffraction models. By using site-specific information, this technique deterministically models the propagation channel, including the path loss, the multipath delay and angle spread. However, the high computational burden and lack of detailed terrain and building databases make ray tracing models difficult to use. For computation efficiency, some physical-based models, such as Lee's model and geometrically based single bounce models, and analytical-based models, such as correlation-based model, are developed.

#### B. *Lee's model*

In Lee's model, scatterers are evenly spaced on a circular ring about the mobile as shown in Fig. 2-3 [23, 24]. Each of the scatterers is intended to represent the effect of many scatterers within the region, and hence are referred to as effective scatterers.

Assuming that  $N$  scatterers are uniformly placed on the circle with radius  $R$  and oriented such that a scatterer is located on the LOS, the discrete AoAs are



$$\phi_i \approx \frac{R}{D} \sin\left(\frac{2\pi}{N}i\right), \quad i = 0, 1, \dots, N-1 \quad (2-10)$$

From the discrete AoAs, the correlation of the signals between any two elements of the array can be found using

$$\rho(d, \theta_0, R, D) = \frac{1}{N} \sum_{i=0}^{N-1} \exp[-j2\pi d \cos(\theta_0 + \theta_i)] \quad (2-11)$$

where  $d$  is the element spacing and  $\theta_0$  is measured with respect to the line between the two elements as shown in Fig. 2-3.

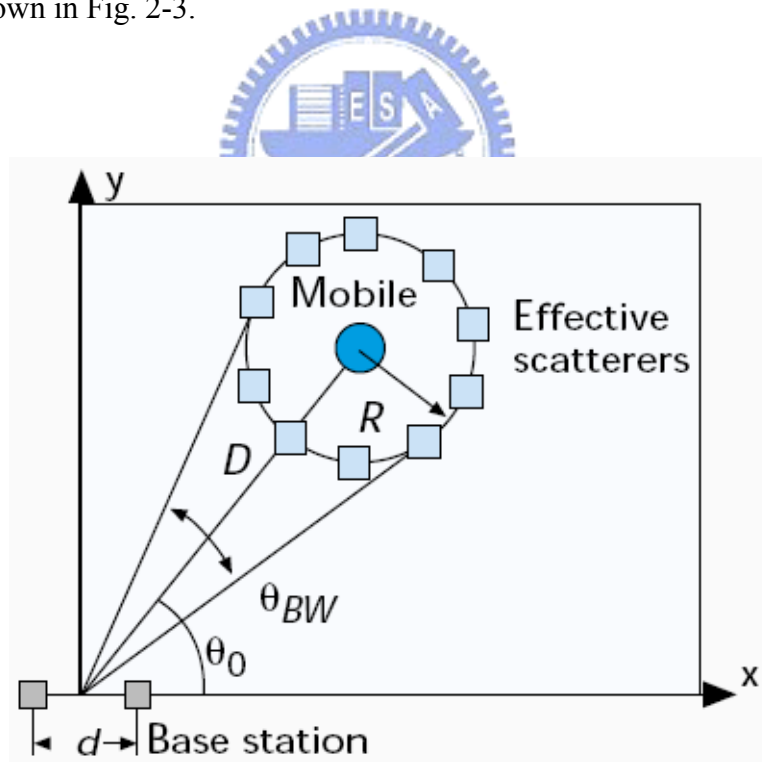


**Fig. 2-3** The illustration of the geometry of Lee's model.

### C. Geometrically Based Single Bounce Circular Model

The Geometrically Based Single Bounce Circular Model (GBSBCM) is applicable to macro-cell scenarios. The geometry of the GBSBCM is shown in Fig. 2-4. It assumes that the scatterers lie within radius  $R_m$  about the mobile. Often the requirement that  $R_m < D$  is imposed. Furthermore, it assumes that there is no scatterer near the base station since the height of base station antenna is very large relative to scatterers in macro-cell environments. The idea of a circular region of scatterers centered about the mobile was originally proposed by Jakes [25] to derive theoretical results for the correlation observed between two antenna elements. The joint ToA and AoA density function at the mobile unit is [26]

$$f_{\tau, \phi}(\tau, \phi) = \begin{cases} \frac{(D^2 - \tau^2 c^2)(D^2 c - 2D\tau c^2 \cos \phi + \tau^2 c^3)}{4\pi R_m^2 (D \cos \phi - \tau c)^3} & \frac{D^2 - \tau^2 c^2}{D \cos \phi - \tau c} \leq 2R_m \\ 0 & \text{otherwise} \end{cases} \quad (2-12)$$

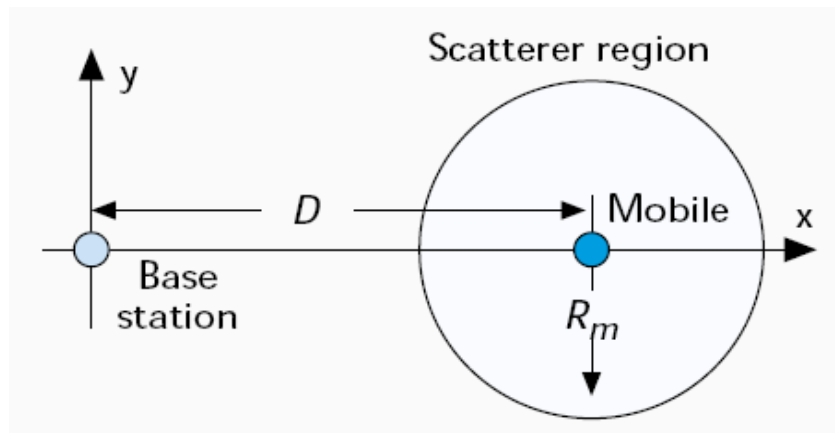


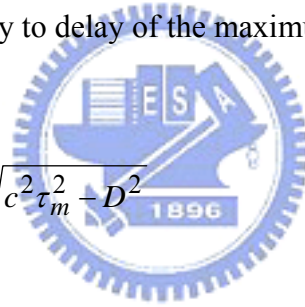
Fig. 2-4 The illustration of the geometry of GBSBCM.

---

#### D. Geometrically Based Single Bounce Elliptical Model

For micro-cell environments where the base station antenna is at the same height as the surrounding scatterers, the Geometrically Based Single Bounce Elliptical Model (GBSBEM) is developed to take into account the effect of scatterers around the base station antennas [27-28]. In the GBSBEM, it assumes that scatterers are uniformly distributed within an ellipse, as shown in Fig. 2-5, where the base station and mobile are the foci of the ellipse. The parameters  $a_m$  and  $b_m$  are the semi-major axis and semi-minor axis values, which are implicitly to delay of the maximum ToA to be considered,  $\tau_m$ , by

$$a_m = c\tau_m/2, \quad b_m = \sqrt{c^2\tau_m^2 - D^2} \quad (2-13)$$



where  $c$  is the speed of light.

A nice attribute of the elliptical model is the physical interpretation that only multipath signals that arrive with an absolute delay  $\tau_m$  are accounted for by the model. Ignoring components with larger delays is possible since signals with longer delays will experience greater path loss, and hence have relatively low power compared to those with shorter delays.

The joint ToA and AoA density function is given by [26]

$$f_{\tau, \phi}(\tau, \phi) = \begin{cases} \frac{(D^2 - \tau^2 c^2)(D^2 c - 2D\tau c^2 \cos \phi + \tau^2 c^3)}{4\pi a_m b_m (D \cos \phi - \tau c)^3} & \frac{D}{c} < \tau \leq \tau_m \\ 0 & \text{otherwise} \end{cases} \quad (2-14)$$

In Chapter 4, a three-dimensional GBSBM which combines the concept of Lee's model, GBSBCM and GBSBEM, is proposed to derived the correlation of the signals between any two elements of an spatial-/polar-array in pico-cell (indoor) environments.

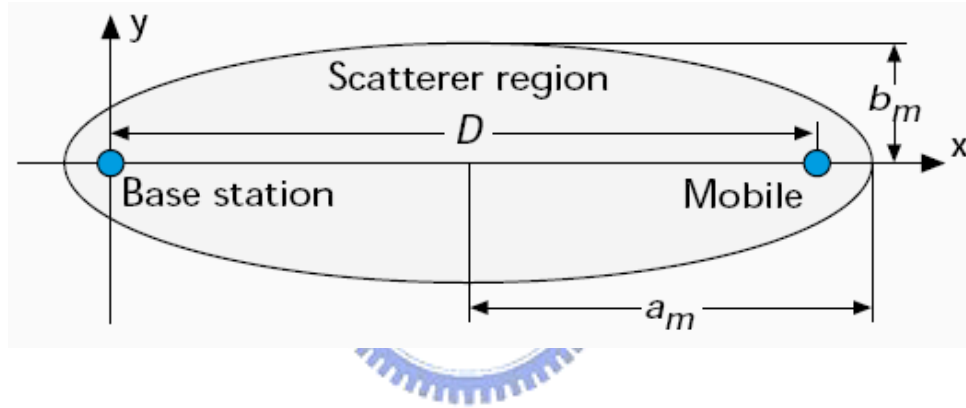


**Fig. 2-5 The illustration of the geometry of GBSBEM.**

### ***E. Correlation-based Models***

In contrast to physical models, analytical channel models characterize the transfer function of the channel between the individual transmit and receive antennas in a mathematical/analytical way without explicitly accounting for wave propagation.

In [29-30], the European Union IST METRA (Multi-Element Transmit Receive Antennas) project proposed a stochastic model based on the power correlation matrix of

---

MIMO channels. In this model, it claims that the spatial cross correlation coefficient can be expressed as the product of the correlations at transmitting and receiving side. i.e.,

$$\rho_{m_2 n_2}^{m_1 n_1} = \left\langle \left| H_{m_1 n_1}^l \right|^2, \left| H_{m_1 n_1}^l \right|^2 \right\rangle = \rho_{n_1 n_2}^{Tx} \rho_{m_1 m_2}^{Rx} \quad (2-15)$$

which can be also written in matrix form as

$$\mathbf{P}_H = \mathbf{P}_H^{Tx} \otimes \mathbf{P}_H^{Rx} \quad (2-16)$$

where ‘ $\otimes$ ’ denotes the Kronecker product,  $\mathbf{P}_H$  is the power correlation matrix of the MIMO channel,  $\mathbf{P}_H^{Tx}$  and  $\mathbf{P}_H^{Rx}$  are the power correlation matrices seen from the transmitter and receiver, respectively.

According to the above description, the MIMO channel can be easily generated by

$$\text{vec}(\mathbf{H}_l) = \sqrt{P_l} \mathbf{C} \mathbf{z}_l \quad (2-17)$$

where  $\text{vec}(\mathbf{X})$  is the operation of stacking the columns of a matrix  $\mathbf{X}$  into a vector.  $\mathbf{z}_l$  is a column vector ( $MN \times 1$ ) with *i.i.d.* zero-mean complex Gaussian elements.  $\mathbf{C}$  is a symmetric matrix and the  $(x, y)^{\text{th}}$  element of  $\mathbf{C}\mathbf{C}^T$  equals the root of the power correlation coefficient between the  $x^{\text{th}}$  and  $y^{\text{th}}$  element of  $\text{vec}(\mathbf{H}_l)$ .  $P_l$  denotes channel power at delay time  $\tau_l$ .

---

## 2.3.2 MIMO Channel Models in Standards

### A. IEEE 802.11n spatial channel model

To enable multiple-input multiple-output (MIMO) antenna technologies in wireless local area networks (WLAN), the task group n (TGn) of IEEE 802.11 standardization group proposed a set of channel models applicable to indoor MIMO WLAN systems [7]. Some of the channel models are an extension of the SISO WLAN channel models, and a newly developed multiple antenna models is based on the cluster model developed by Saleh and Valenzuela [6].

In [7], six clustering delay profile models are proposed for different indoor environments. The model parameters, such as number of clusters, number of taps in a particular cluster, and power, angular spread (AS), angle-of-arrival (AoA), and angle of departure (AoD) values of each tap are defined for each delay profile model. With the knowledge of each tap power, AS, and AoA (AoD), for a given antenna configuration, the channel matrix  $H$  can be determined.

The MIMO channel modeling approach, which is similar to the method presented in [30-31] that utilizes receive and transmit correlation matrices. For a  $4 \times 4$  array, the MIMO channel matrix  $H$  for each tap can be separated into a fixed (constant, LOS) matrix and a Rayleigh (variable, NLOS) matrix

$$\begin{aligned}
H &= \sqrt{P} \left( \sqrt{\frac{K}{K+1}} H_F + \sqrt{\frac{1}{K+1}} H_V \right) \\
&= \sqrt{P} \left( \sqrt{\frac{K}{K+1}} \begin{bmatrix} e^{j\phi_{11}} & e^{j\phi_{12}} & e^{j\phi_{13}} & e^{j\phi_{14}} \\ e^{j\phi_{21}} & e^{j\phi_{22}} & e^{j\phi_{23}} & e^{j\phi_{24}} \\ e^{j\phi_{31}} & e^{j\phi_{32}} & e^{j\phi_{33}} & e^{j\phi_{34}} \\ e^{j\phi_{41}} & e^{j\phi_{42}} & e^{j\phi_{43}} & e^{j\phi_{44}} \end{bmatrix} + \sqrt{\frac{1}{K+1}} \begin{bmatrix} X_{11} & X_{12} & X_{13} & X_{14} \\ X_{21} & X_{22} & X_{23} & X_{24} \\ X_{31} & X_{32} & X_{33} & X_{34} \\ X_{41} & X_{42} & X_{43} & X_{44} \end{bmatrix} \right) \quad (2-18)
\end{aligned}$$

where  $X_{ij}$  ( $i$ -th receiving and  $j$ -th transmitting antenna) are correlated zero-mean, unit variance, complex Gaussian random variables as coefficients of the variable NLOS (Rayleigh) matrix  $H_V$ ,  $\exp(j\phi_{ij})$  are the elements of the fixed LOS matrix  $H_F$ ,  $K$  is the Rician  $K$ -factor, and  $P$  is the power of each tap. To correlate the  $X_{ij}$  elements of the matrix  $X$ , the following method can be used

$$[X] = [R_{rx}]^{1/2} [H_{iid}] ([R_{tx}]^{1/2})^T \quad (2-19)$$

where  $R_{tx}$  and  $R_{rx}$  are the receive and transmit correlation matrices, respectively, and  $H_{iid}$  is a matrix of independent zero mean, unit variance, complex Gaussian random variables, and

$$R_{rx} = \begin{bmatrix} 1 & \rho_{rx12} & \rho_{rx13} & \rho_{rx14} \\ \rho_{rx21} & \rho_{rx22} & \rho_{rx23} & \rho_{rx24} \\ \rho_{rx31} & \rho_{rx32} & \rho_{rx33} & \rho_{rx34} \\ \rho_{rx41} & \rho_{rx42} & \rho_{rx43} & \rho_{rx44} \end{bmatrix} \quad (2-20)$$

---


$$R_{tx} = \begin{bmatrix} 1 & \rho_{tx12} & \rho_{tx13} & \rho_{tx14} \\ \rho_{tx21} & \rho_{tx22} & \rho_{tx23} & \rho_{tx24} \\ \rho_{tx31} & \rho_{tx32} & \rho_{tx33} & \rho_{tx34} \\ \rho_{tx41} & \rho_{tx42} & \rho_{tx43} & \rho_{tx44} \end{bmatrix} \quad (2-21)$$

where  $\rho_{txij}$  are the complex correlation coefficients between  $i$ -th and  $j$ -th transmitting antennas, and  $\rho_{rxij}$  are the complex correlation coefficients between  $i$ -th and  $j$ -th receiving antennas.

The complex correlation coefficient values calculation for each tap is based on the power angular spectrum (PAS) with angular spread (AS) being the second moment of PAS [32-33]. Using the PAS shape, AS, mean angle-of-arrival (AoA), and individual tap power, correlation matrices of each tap can be determined as described in [32]. For the uniform linear array (ULA) the complex correlation coefficient at the linear antenna array is expressed as

$$\rho = R_{XX}(D) + jR_{XY}(D) \quad (2-22)$$

where  $D = 2\pi d / \lambda$ , and  $R_{XX}$  and  $R_{XY}$  are the cross-correlation functions between the real parts (equal to the cross-correlation function between the imaginary parts) and between the real part and imaginary part, respectively, with



---


$$R_{XX}(D) = \int_{-\pi}^{\pi} \cos(D \sin \phi) PAS(\phi) d\phi \quad (2-23)$$

$$R_{XY}(D) = \int_{-\pi}^{\pi} \sin(D \sin \phi) PAS(\phi) d\phi \quad (2-24)$$

### ***B. 3GPP SCM/SCME channel model***

To enable multiple-input multiple-output (MIMO) antenna technologies in cellular systems, standardization groups 3GPP and 3GPP2 defined a spatial channel model (SCM) [8] for cellular systems with bandwidths up to 5 MHz. Recently, for 3GPP long-term evolution (LTE) standardization [2], an SCM extension (SCME) model including the wideband spatial channel characteristics was proposed to support bandwidths up to 20 MHz.

In [8], the spatial channel models for link level and system level simulations are defined. Link level simulations will not be used to compare performance of different algorithms. Rather, they will be used only for calibration, which is the comparison of performance results from different implementations of a given algorithm. Table 2-1 summarizes the physical parameters to be used for link level modeling. The MIMO channel matrix generation method of the link level model is similar to that described in Section 2.3.2-A.

---

As opposed to link simulations which simply consider a single BS transmitting to a single MS, the system simulations typically consist of multiple cells/sectors, BSs, and MSs. Fig. 2-6 shows a roadmap for generating the channel coefficients. It defines three environments (suburban macro, urban macro, and urban micro) where urban micro is differentiated in line-of-sight (LOS) and non-LOS (NLOS) propagations. Detailed model parameters are listed in Table 2-2. In each environment, the number of paths is equal to 6. Each path is further composed of 20 spatially separated sub-paths to produce a Rayleigh fading envelope. The main characteristics of the model include a narrow angle spread (AS) per-path, with specific base station angle of departure (AoD) and mobile station angle of arrival (AoA) models. The large-scale behaviors, described by the composite AS, DS and shadow fading (SF), are simultaneously correlated in the log-normal domain to produce the expected channel characteristics for each realization of the channel. Path powers, path delays, and angular properties for both sides of the link are modeled as random variables defined through probability density functions (PDFs) and cross-correlations.

For an  $S$  element linear BS array and a  $U$  element linear MS array, the channel coefficients for one of  $N$  multipath components are given by a  $U$ -by- $S$  matrix of complex amplitudes. Denote the channel matrix for the  $n$ th multipath component ( $n = 1, \dots, N$ ) as  $\mathbf{H}_n(t)$ . The  $(u,s)$ th component ( $s = 1, \dots, S; u = 1, \dots, U$ ) of  $\mathbf{H}_n(t)$  is given by

---


$$h_{u,s,n}(t) = \sqrt{\frac{P_n \sigma_{SF}}{M}} \sum_{m=1}^M \left( \begin{array}{l} \sqrt{G_{BS}(\theta_{n,m,AoD})} \exp(j[kd_s \sin(\theta_{n,m,AoD}) + \Phi_{n,m}]) \times \\ \sqrt{G_{MS}(\theta_{n,m,AoA})} \exp(jkd_u \sin(\theta_{n,m,AoA})) \times \\ \exp(jk \|\mathbf{v}\| \cos(\theta_{n,m,AoA} - \theta_v) t) \end{array} \right) \quad (2-25)$$

where the angular parameters are shown in Fig. 2-7.

The 3GPP SCME is an extension to the SCM for bandwidths up to 20 MHz. In 3GPP SCME, the 20 sub-paths of SCM are split into 3 subsets, denoted as mid-paths, which are moved to different delays relative to the original path as shown in Fig. 2-8. The delays and powers of these 3 mid-paths are predetermined by an exponential power decay function with 10-ns delay spread. To keep the fading distribution close to Rayleigh, a mid-path is lumped of 4 or more sub-paths. The mid-path ASs ( $AS_i$  where  $i$  is the mid-path index) are optimized such that the deviation from the path AS ( $AS_n$  where  $n$  is the path index), i.e. the AS of all mid-paths combined, is minimized. The delays and the corresponding sub-paths of each mid-path are listed in Table 2-3.

**Table 2-1 The channel parameters of 3GPP SCM for link level simulations.**

Model		Case I	Case II	Case III	Case IV			
# of Paths		1) 4+1 (LOS on, K = 6dB) 2) 4 (LOS off)	6	6	1			
Relative Path Power (dB)	Delay (ns)	1) 0.0 2) -Inf	0	0,0	0	0	0	
		1) -6.51 2) 0.0	0	-1.0	310	-0.9	200	
		1) -16.21 2) -9.7	110	-9.0	710	-4.9	800	
		1) -25.71 2) -19.2	190	-10.0	1090	-8.0	1200	
		1) -29.31 2) -22.8	410	-15.0	1730	-7.8	2300	
				-20.0	2510	-23.9	3700	
Speed (km/h)		1) 3 2) 30, 120	3, 30, 120	3, 30, 120	3			
UE / Mobile Station	Topology	Reference $0.5\lambda$	Reference $0.5\lambda$	Reference $0.5\lambda$	N/A			
	PAS	1) LOS on: Fixed AoA for LOS component, remaining power has 360 degree uniform PAS. 2) LOS off: PAS with a Laplacian distribution, RMS angle spread of 35 degrees per path	RMS angle spread of 35 degrees per path with a Laplacian distribution Or 360 degree uniform PAS.	RMS angle spread of 35 degrees per path with a Laplacian distribution	N/A			
	DoT (degrees)	0	22.5	-22.5	N/A			
	AoA (degrees)	22.5 (LOS component) 67.5 (all other paths)	67.5 (all paths)	22.5 (odd numbered paths), -67.5 (even numbered paths)	N/A			
Node B / Base Station	Topology	Reference: ULA with $0.5\lambda$ -spacing or $4\lambda$ -spacing or $10\lambda$ -spacing			N/A			
	PAS	Laplacian distribution with RMS angle spread of 2 degrees or 5 degrees, per path depending on AoA/AoD			N/A			
	AoD/AoA (degrees)	50° for 2° RMS angle spread per path 20° for 5° RMS angle spread per path			N/A			

**Table 2-2 The channel parameters of 3GPP SCM for system level simulations.**

Channel Scenario	Suburban Macro	Urban Macro	Urban Micro
Number of paths ( $N$ )	6	6	6
Number of sub-paths ( $M$ ) per-path	20	20	20
Mean AS at BS AS at BS as a lognormal RV $\sigma_{AS} = 10^{\wedge}(\varepsilon_{AS}x + \mu_{AS}), x \sim \eta(0,1)$	$E(\sigma_{AS})=5^{\circ}$ $\mu_{AS} = 0.69$ $\varepsilon_{AS} = 0.13$	$E(\sigma_{AS})=8^{\circ}, 15^{\circ}$ $8^{\circ} \mu_{AS} = 0.810$ $\varepsilon_{AS} = 0.34$ $15^{\circ} \mu_{AS} = 1.18$ $\varepsilon_{AS} = 0.210$	NLOS: $E(\sigma_{AS})=19^{\circ}$ N/A
$r_{AS} = \sigma_{AoD} / \sigma_{AS}$	1.2	1.3	N/A
Per-path AS at BS (Fixed)	2 deg	2 deg	5 deg (LOS and NLOS)
BS per-path AoD Distribution standard distribution	$\eta(0, \sigma_{AoD}^2)$ where $\sigma_{AoD} = r_{AS}\sigma_{AS}$	$\eta(0, \sigma_{AoD}^2)$ where $\sigma_{AoD} = r_{AS}\sigma_{AS}$	U(-40deg, 40deg)
Mean AS at MS	$E(\sigma_{AS,MS})=68^{\circ}$	$E(\sigma_{AS,MS})=68^{\circ}$	$E(\sigma_{AS,MS})=68^{\circ}$
Per-path AS at MS (fixed)	$35^{\circ}$	$35^{\circ}$	$35^{\circ}$
MS Per-path AoA Distribution	$\eta(0, \sigma_{AoA}^2(\text{Pr}))$	$\eta(0, \sigma_{AoA}^2(\text{Pr}))$	$\eta(0, \sigma_{AoA}^2(\text{Pr}))$
Delay spread as a lognormal RV $\sigma_{DS} = 10^{\wedge}(\varepsilon_{DS}x + \mu_{DS}), x \sim \eta(0,1)$	$\mu_{DS} = -6.80$ $\varepsilon_{DS} = 0.288$	$\mu_{DS} = -6.18$ $\varepsilon_{DS} = 0.18$	N/A
Mean total RMS Delay Spread	$E(\sigma_{DS})=0.17 \mu\text{s}$	$E(\sigma_{DS})=0.65 \mu\text{s}$	$E(\sigma_{DS})=0.251 \mu\text{s}$ (output)
$r_{DS} = \sigma_{delays} / \sigma_{DS}$	1.4	1.7	N/A
Distribution for path delays			U(0, 1.2 $\mu\text{s}$ )
Lognormal shadowing standard deviation, $\sigma_{SF}$	8dB	8dB	NLOS: 10dB LOS: 4dB
Pathloss model (dB), $d$ is in meters	$31.5 + 35\log_{10}(d)$	$34.5 + 35\log_{10}(d)$	NLOS: $34.53 + 38\log_{10}(d)$ LOS: $30.18 + 26\log_{10}(d)$

Table 2-3 Sub-paths to mid-paths assignment and resulting angle spread in 3GPP SCME

Mid-path	Number of sub-paths	Delay	Sub-paths	$As_i / AS_n$
1	10 (of 20)	0	1, 2, 3, 4, 5, 6, 7, 8, 19, 20	0.9865
2	6 (of 20)	12.5 ns	9, 10, 11, 12, 17, 18	1.0056
3	4 (of 20)	25 ns	13, 14, 15, 16	1.0247

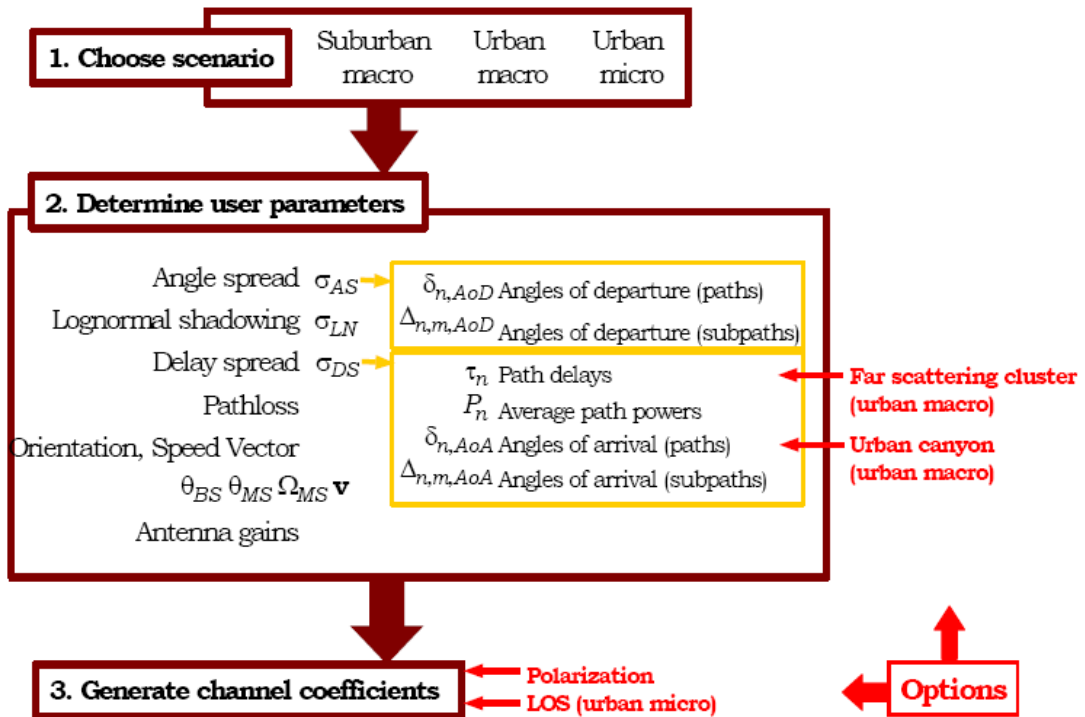


Fig. 2-6 The illustration of the procedure for generating MIMO channels.

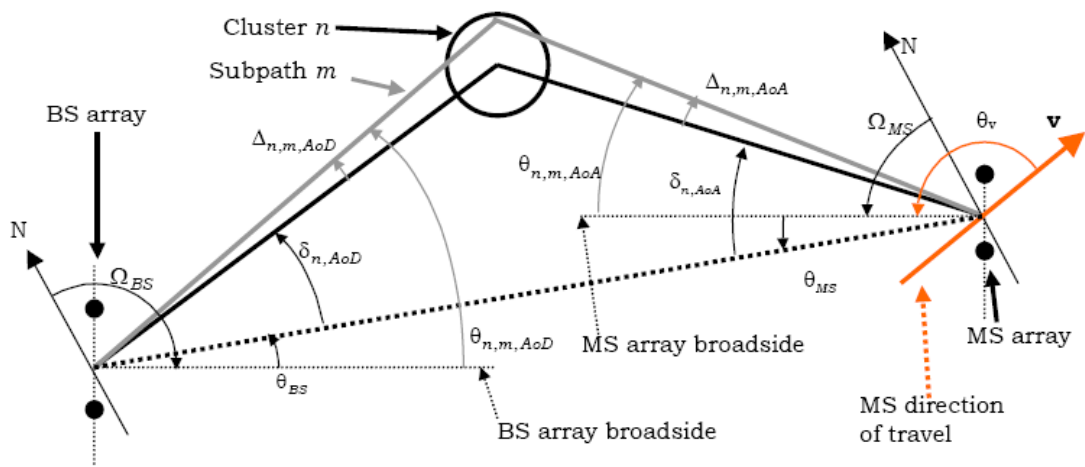


Fig. 2-7 The illustration of multipath angle parameters at BS and MS sides.

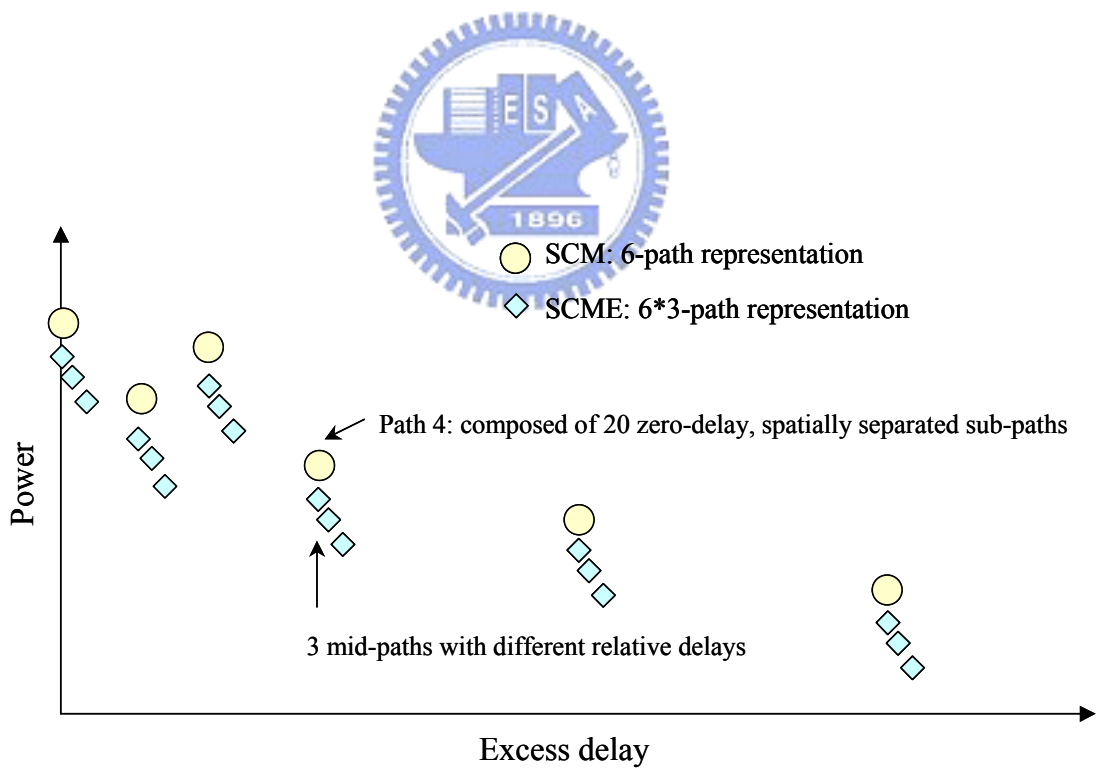


Fig. 2-8 A diagram of the mid-path approach of SCME.

---

# **Chapter 3 Measurement and Modeling of Wideband SISO Channels**



**In this chapter, first our proposed method for wideband multipath model parameters estimation is described. We validate this method with extensive measurement data. The measurement setup and environments and the validation results are presented.**



---

### 3.1 Introduction

In order to realize the B3G systems, a thorough understanding of the time dispersion characteristics of radio multipath propagation channels is required. In high-speed wireless data transmission, severe frequency-selective fading of multipath channel causes inter-symbol interference (ISI) and leads to a significant problem for the systems. To solve the problem, modeling of multipath time-of-arrival (TOA), particular on the multipath-clustering phenomenon, is a fundamental and important work.

Although there are many researches focused on the exploration or modeling of multipath-clustering phenomenon, few researches focused on the effect of signal bandwidth on observed multipath-clustering so far. As shown in Fig. 3-1, it is easily understood that in the observation of multipath-clustering of a radio channel using a band-limited signal, the result is mainly affected by the signal resolution, which is the reciprocal of the signal bandwidth. In this paper, based on the  $\Delta$ - $K$  model, newly formulas are derived to describe the relationships between the observed TOA model parameters of narrowband signals and those of wideband signals. Through this approach, effect of signal bandwidth on the observable multipath-clustering is explored. Furthermore, to completely characterize the time dispersion characteristics of the channel, a model using power ratio, decay constant and the Rician factor to describe multipath averaged power delay profile

and amplitude fading is proposed. Formulas to relate these model parameters of a wideband signal to those of a narrowband signal are also derived. Here, the model parameter estimation methods have been extensively validated by comparing the computed channel parameters with the ones extracted from the measured channel responses of 1.95 GHz and 2.44 GHz broadband radios in metropolitan and suburban areas, and of 3-5 GHz UWB signals in indoors.

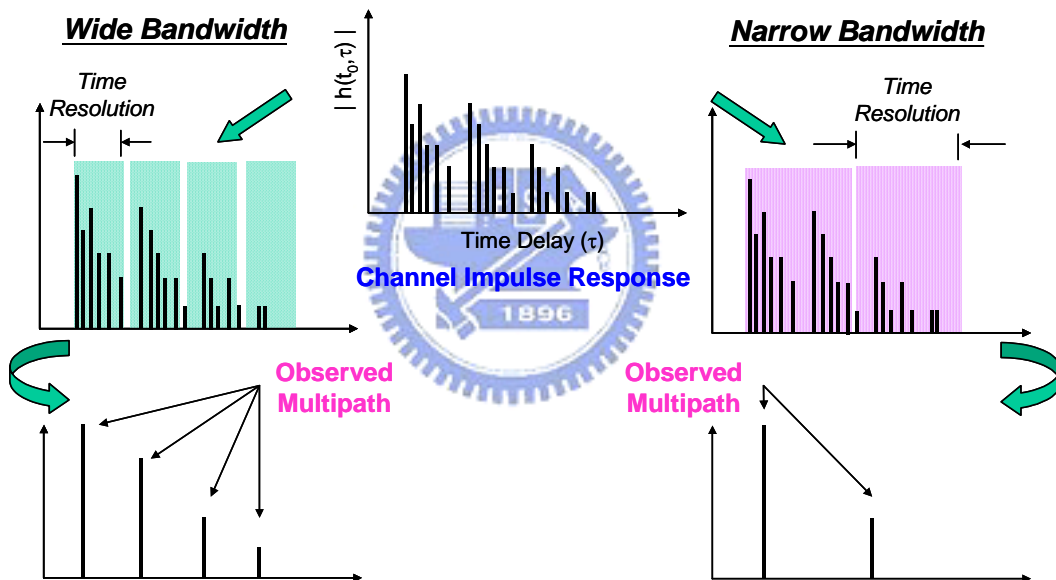


Fig. 3-1 A diagram for bandwidth effect on the observed multipath propagation channels.

### 3.2 A novel method for wideband model parameter estimation

To explore bandwidth dependency of the model parameters, which include the clustering parameter, formulas to describe the relationships between observed model parameters of narrowband signals and those of wideband signals are derived. Here,  $\Delta$ - $K$

---

model is adopted to characterize the multipath-clustering. It is noted that the bandwidth of the wideband signal is confined to be  $n$  times of the narrowband signal's, where  $n$  is a positive integer. For convenience, the parameters with a subscript  $f$  or  $F$  correspond to those of bandwidth  $f$  or  $F$ , respectively, where  $F=n\cdot f$ .

### 3.2.1 Bandwidth on observable multipath-clustering

#### A. Formulas for wideband to narrowband

Since a bin width is inversely proportional to its signal bandwidth,  $\Delta_f$  is equal to  $n\cdot\Delta_F$ , where  $\Delta_f$  and  $\Delta_F$  are the bin widths of the systems with signal bandwidths  $f$  and  $F$ , respectively. Therefore, when a received path occurs at bin  $i$  of a signal with bandwidth  $f$ , the path should arrive at one or more of the bins covering from the  $(n\cdot i-n+1)^{\text{th}}$  bin to the  $(n\cdot i)^{\text{th}}$  bin, for the signal with bandwidth  $F$ , which is due to the increase of time resolution interval. Fig. 3-2 shows an example of  $n=2$ .

With the above analysis,  $\lambda_{i,f}$  and  $P_{i,f}$  are derived in terms of  $\lambda_{j,F}$  and  $P_{j,F}$  by (3-1) and (3-2), respectively.

$$\lambda_{i,f} = 1 - \prod_{r=1}^n (1 - \lambda_{A+r,F}) \quad (3-1)$$

where  $A = n\cdot i - n$ .

$$P_{i,f} = \begin{cases} P_{A+1,F} + (1 - P_{A+1,F}) \lambda_{A+2,F} & , n = 2 \\ P_{A+1,F} + (1 - P_{A+1,F}) \left\{ \lambda_{A+2,F} + \sum_{r=3}^n \left[ \lambda_{A+r,F} \prod_{s=3}^r (1 - \lambda_{A+s-1,F}) \right] \right\} & , n \geq 3 \end{cases} \quad (3-2)$$

Substituting  $\lambda_{i,f}$  and  $P_{i,f}$  into (2-6),  $k_{i,f}$  is obtained. Here, let  $n=2$ , the analytical relationship between  $k_{i,f}$  and  $k_{2 \cdot i-1,F}$  is found and written as

$$(k_{i,f} - 1) = (k_{2 \cdot i-1,F} - 1) \cdot \frac{\lambda_{2 \cdot i-1,F} (1 - \lambda_{2 \cdot i,F})}{[\lambda_{2 \cdot i,F} + \lambda_{2 \cdot i-1,F} (1 - \lambda_{2 \cdot i,F})]} \cdot \frac{[k_{2 \cdot i-2,F} \cdot \lambda_{2 \cdot i-2,F} \cdot P_{2 \cdot i-3,F} + \lambda_{2 \cdot i-2,F} (1 - P_{2 \cdot i-3,F})]}{[P_{2 \cdot i-3,F} + \lambda_{2 \cdot i-2,F} (1 - P_{2 \cdot i-3,F})]} \quad (3-3)$$

On the right-hand side of (3-3), magnitudes of the second and third factors are in the range of 0 to 1. From (3-3), it is found that  $k_{i,f}$  is smaller than  $k_{2 \cdot i-1,F}$  if  $k_{2 \cdot i-1,F} > 1$ . It means that wider bandwidth signal observes stronger multipath-clustering phenomenon. It is noted that  $k_{2 \cdot i-1,F} \cong k_{2 \cdot i,F}$ , which is found from measurement data and is shown in Section 3-3.

### **B. Formulas for narrowband to wideband**

With (3-1) and (3-2), the observed model parameters of a narrowband signal cannot determine those of a wideband signal due to the limited conditions. For  $n=2$ , one extra

---

condition is needed to determine three unknown parameters,  $\lambda_{2\cdot i-1,F}$ ,  $\lambda_{2\cdot i,F}$  and  $P_{2\cdot i-1,F}$  with those of bandwidth  $f$ ,  $\lambda_{i,f}$  and  $P_{i,f}$ . Here, the condition is given by assuming  $\lambda_{2\cdot i-1,F} = \lambda_{2\cdot i,F}$ , i.e., the path arrival rates of two neighboring bins are equal. It is because that for both outdoor broadband and indoor UWB radio channels, multipath excess delay time is much larger than the time resolution (bin width). Based on this assumption,  $\lambda_{2\cdot i-1,F}$  and  $\lambda_{2\cdot i,F}$  are solved from (3-1)

$$\lambda_{2\cdot i-1,F} = \lambda_{2\cdot i,F} = 1 - \sqrt{1 - \lambda_{i,f}} \quad (3-4)$$

However, our assumption may lead to underestimate  $\lambda_{2\cdot i-1,F}$  and overestimate  $\lambda_{2\cdot i,F}$  since the path arrival rate decreased asymptotically with bin number. To reduce the estimation errors,  $\lambda_{2\cdot i-1,F}$  and  $\lambda_{2\cdot i,F}$  from (3-4) are modified using the interpolation method and are given by (3-5a) and (3-5b), respectively

$$\lambda_{2\cdot i-1,F} = \mathbf{min} \left\{ 1, \left[ \lambda_{2\cdot i-1,F} + \frac{1}{4} \cdot (\lambda_{2\cdot i-1,F} - \lambda_{2\cdot i+1,F}) \right] \right\} \quad (3-5a)$$

$$\lambda_{2\cdot i,F} = \lambda_{2\cdot i-1,F} - \frac{1}{4} \cdot (\lambda_{2\cdot i-1,F} - \lambda_{2\cdot i+1,F}) \quad (3-5b)$$

It is noted that  $\lambda_{2\cdot i-1,F}$  and  $\lambda_{2\cdot i+1,F}$  on the right-hand side of (3-5a) and (3-5b) are calculated from (3-4). Then, from (3-2) with  $n=2$ ,  $P_{2\cdot i-1,F}$  is solved and given by (3-6a)

$$P_{2 \cdot i-1, F} = (P_{i, f} - \lambda_{2 \cdot i, F}) / (1 - \lambda_{2 \cdot i, F}) \quad (3-6a)$$

$P_{2 \cdot i, F}$  is computed by averaging its neighboring points and is given by (3-6b)

$$P_{2 \cdot i, F} = (P_{2 \cdot i-1, F} + P_{2 \cdot i+1, F}) / 2 \quad (3-6b)$$

Substituting  $\lambda_{j, F}$  and  $P_{j, F}$  into (2-6),  $k_{j, F}$  is obtained. Through the above approaches, the model parameters of a wideband signal,  $\lambda_{j, F}$ ,  $P_{j, F}$  and  $k_{j, F}$ , are determined by those of a narrowband signal,  $\lambda_{i, f}$  and  $P_{i, f}$ , for  $n=2$ . Furthermore, by repeating the procedures, this method can be extended to  $n=2^m$ , where  $m=2, 3, \dots$

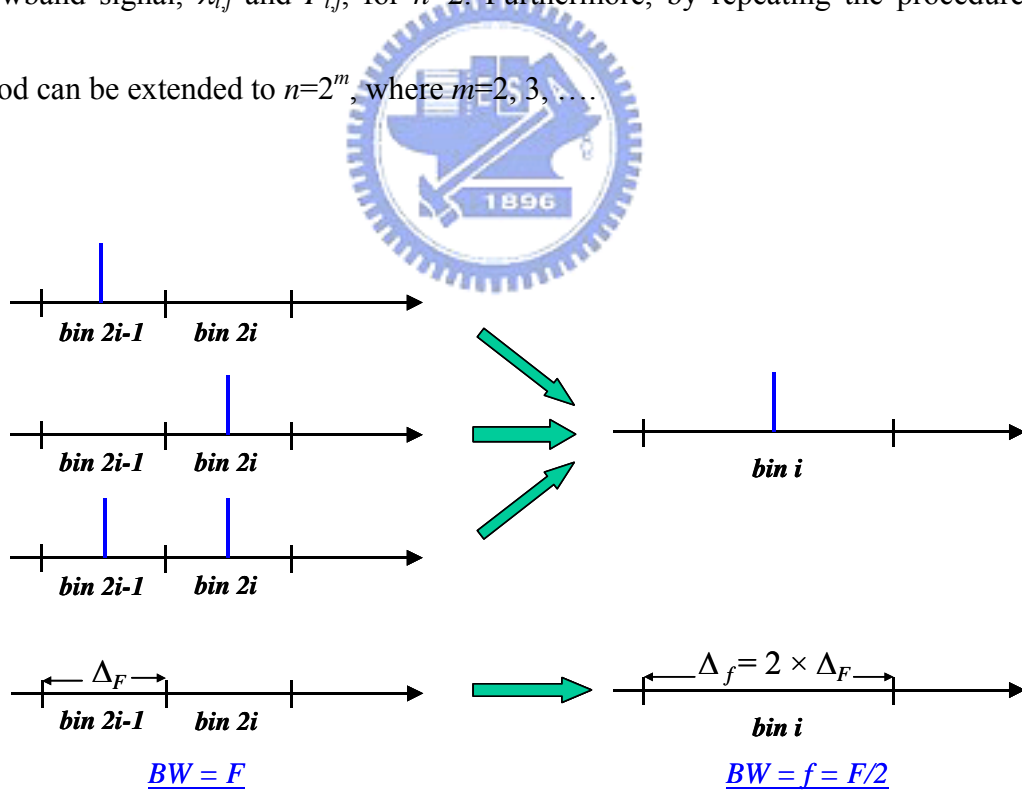


Fig. 3-2 A diagram for the arrival of multipath when bandwidth changes from  $F$  to  $f$  for  $n=2$ .


---

### 3.2.2 Bandwidth on multipath power decay and amplitude fading

To completely characterize the time dispersion characteristics of the channel, effects of bandwidth on multipath averaged power decay and amplitude fading are analyzed as follows.

#### A. A statistical model for multipath averaged power decay and amplitude fading

In many literatures for broadband and UWB radio channel modeling [34-35], the small-scale averaged power delay profile (aPDP),  $\bar{g}(\tau)$ , is modeled by an exponential time decay function with a stronger first bin and is expressed as


$$\bar{g}(\tau) = \bar{G}_1 \left[ \delta(\tau_1) + \sum_{i=2}^L \gamma \exp[-(\tau_i - \tau_2)/\Gamma] \delta(\tau_i) \right] \quad (3-7)$$

where  $\bar{G}_1$  is the mean power of the first bin,  $\tau_i$  is the relative time delay of bin  $i$  and is equal to  $(i-1) \cdot \Delta$ ,  $\gamma$  is the power ratio that is defined as the ratio of the second bin's mean power to the first bin's mean power,  $\Gamma$  is the exponentially power decay constant and  $\delta$  is the Dirac delta function. From our extended measurement data at indoor environments, one of the examples shown in Fig. 3-3, it is found that this model well describes the measured aPDP.

Based on our measurement data, it is found that the amplitude fading of the first bin

---

follows a Rician distribution with a large Rician factor and the later bins tend to follow the Rayleigh statistics (the Rician factor is closed to zero), as shown in Fig. 3-4. It is noted that measured points no.1-no.12 are in LOS (Line-of-Sight) situations and the rest points are in NLOS (Non LOS) situations. Details of measurements are described later in Section 3.3.2.

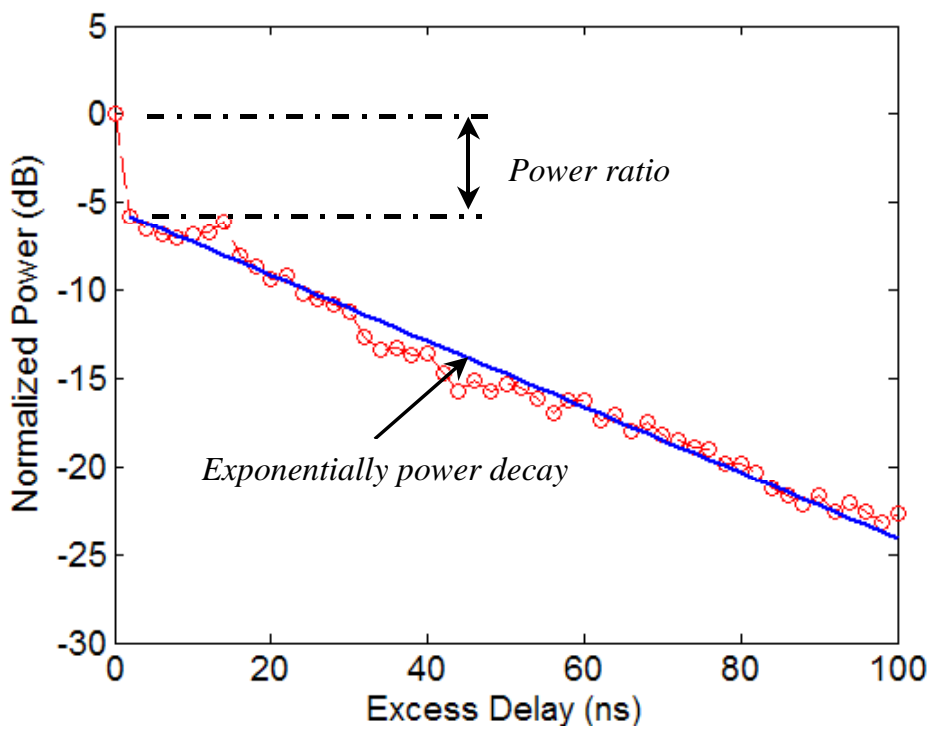


**Fig. 3-3** The averaged power delay profile of a 500 MHz-bandwidth UWB signal at an indoor environment and under NLOS condition. The wavy line shows the measured profile. The straight line, which is obtained by a best-fit procedure, represents an exponential decay line.



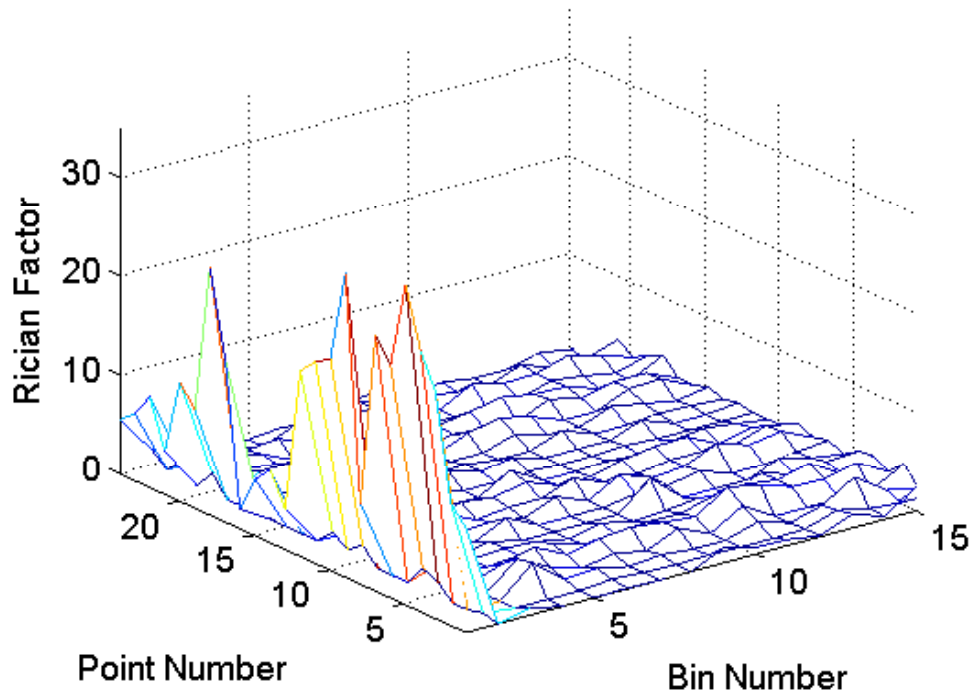


**Fig. 3-4 Rician factors of the first 15 bins of each measured point at indoor environments with 2-GHz bandwidth are shown. The total numbers of measured points are 24.**



***B. Formulas for wideband to narrowband***

For an uncorrelated scattered radio propagation channel [36], bins' amplitudes are distributed independently of one another, and the averaged bin power is calculated by the power sum of multipath in a bin. For example, averaged power sum of two successive bins for bandwidth  $F$  is equal to the averaged power of the corresponding bin for bandwidth  $f$  when  $n=2$ , i.e.,  $\bar{G}_{i,f} = \bar{G}_{2i-1,F} + \bar{G}_{2i,F}$ . From (3-7) and  $n=2$ ,  $\bar{G}_{i,f}$  is expressed by

---


$$\begin{cases} \bar{G}_{1,f} = 1 + \gamma_F \\ \bar{G}_{i,f} = \gamma_F \cdot [\exp(-\Delta_F/\Gamma_F) + \exp(-2 \cdot \Delta_F/\Gamma_F)] \cdot \exp[-(i-2) \cdot \Delta_f/\Gamma_F], i \geq 2 \end{cases} \quad (3-8)$$

From (3-8), it is found that  $\bar{G}_{i,f}$  is exponentially decayed from bin 2 with time decay constant  $\Gamma_F$ . It represents that the decay constant is independent of signal bandwidth, i.e.,  $\Gamma_f = \Gamma_F$ .

From (3-8), the power ratio  $\gamma_f = \bar{G}_{2,f} / \bar{G}_{1,f}$  is expressed by

$$\gamma_f = \frac{\gamma_F}{1 + \gamma_F} \cdot [\exp(-\Delta_F/\Gamma_F) + \exp(-2 \cdot \Delta_F/\Gamma_F)] \quad (3-9)$$

From (3-9),  $\gamma_f$  is greater than  $\gamma_F$  if  $\Gamma_F \gg \Delta_F$ , which is true for the most indoor UWB channels that their decay constants are larger than 10 ns and their bin widths are smaller than 2 ns.

The Rician statistics is mainly characterized by a Rician factor,  $R$ , which is defined as the power ratio of the specular/ LOS path to the scattered multipath. For the first bin, when the signal bandwidth changes from  $F$  to  $f$ , the specular/LOS path power is unchanged but the scattered multipath power is increased by  $\bar{G}_{2,F}$  due to the increase of the bin width and no specular/LOS path in bin 2 (its Rician factor is closed to 0). Therefore,  $R_f$ , after simple derivations, is given by (3-10)

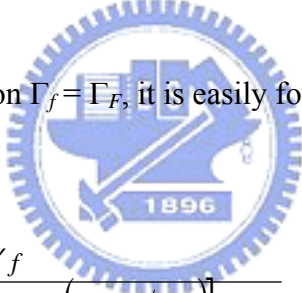
---


$$R_f = \frac{R_F}{1 + (R_F + 1) \cdot \gamma_F} \quad (3-10)$$

Since the denominator of (3-10) is always larger than one,  $R_f$  is smaller than  $R_F$ . The reason for this result is that the total number of scattered multipath in the first bin is increased when the signal bandwidth is decreased, which yields increase of the scattered power. It is noted that (3-10) is not so meaningful for the latter bins since their amplitude fading follow a Rayleigh distribution with their Rician factors all close zero.

### C. Formulas for narrowband to wideband

With (3-9) and the condition  $\Gamma_f = \Gamma_F$ , it is easily found that  $\gamma_f$  is given by



$$\gamma_f = \frac{\gamma_f}{\left[ \exp(-0.5 \cdot \Delta_f / \Gamma_f) + \exp(-\Delta_f / \Gamma_f) \right] - \gamma_f} \quad (3-11)$$

Substituting (3-11) into (3-12),  $R_F$  is expressed by

$$R_F = R_f \cdot \frac{1 + \frac{\gamma_f}{\left[ \exp(-0.5 \cdot \Delta_f / \Gamma_f) + \exp(-\Delta_f / \Gamma_f) \right] - \gamma_f}}{1 - R_f \cdot \frac{\gamma_f}{\left[ \exp(-0.5 \cdot \Delta_f / \Gamma_f) + \exp(-\Delta_f / \Gamma_f) \right] - \gamma_f}} \quad (3-12)$$

---

## 3.3 Measurement setup and environments

### 3.3.1 Outdoor environments

For outdoor environments, the RUSK broadband vector channel sounder [37] is employed to measure the band-limited channel impulse response. The system diagram of the channel sounder is illustrated in Fig. 3-5. It consists of a mobile transmitter with an omni-directional antenna, and a fixed receiver with an 8-element uniform linear array antenna. Maximum 120-MHz broadband radio signal can be generated by periodic multi-frequency signals excitation. It is very helpful for this study, because radio channel data for the narrowband signal can be intercepted from the measurement data of the wideband signal.



Measurements of broadband radio channel impulse response were performed at three outdoor sites in Taipei (a large city) and a suburban area. A summary of the measurement setup and environments for these sites is given in Table 3-1. At each site, the fixed receiver and its antenna were mounted on a rooftop; the mobile transmitter and its antenna were carried by a car with antenna height of 1.8 m above the ground. Measurement was done along selected routes with a speed of 10 Km/hr approximately, and the channel responses were sampled in a time grid of 1000.448 ms. It is noted that the distance between two neighboring channel response sampling points are around 10-20 times of wavelength of the

center frequency, which means that the small-scale measurements were not performed at outdoor sites.

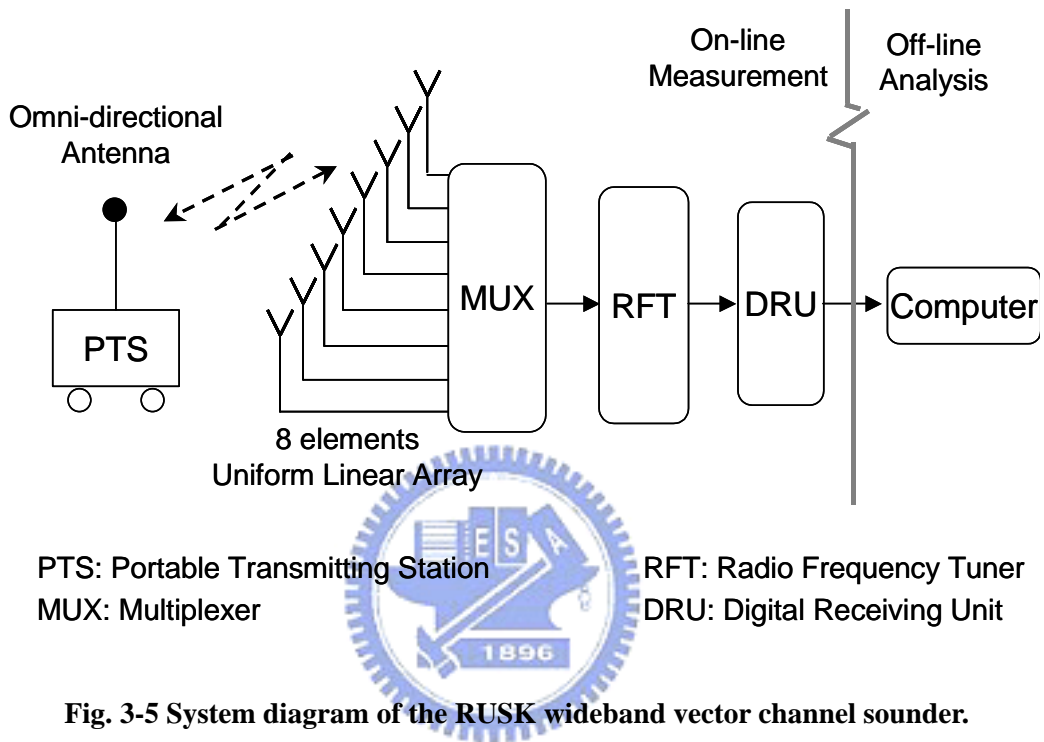


**Fig. 3-5 System diagram of the RUSK wideband vector channel sounder.**

**Table 3-1 Setup and environments for the broadband outdoor channel measurements**

Site No.	Urban 1	Urban 2	Suburban
Measurement Environment	Heavily built up area with an average building height of 10 stories. The maximum one is 26 stories.	Heavily built up area with an average building height of 10 stories. The maximum one is 20 stories.	Small village with buildings of 3~6 stories and gardens with trees and pools.
Numbers of sampled routes and points	Total number of the sampled routes is 7 and each route has 150 meters long approximately. Total sampled points are about 600. Most of them are in NLOS situation.	Total number of the sampled routes is 8 and each route has 250 meters long approximately. Total sampled points are about 900. Most of them are in NLOS situation.	Total number of the sampled routes is 5 and each route has 150 meters long approximately. Total sampled points are about 400. Most of them are in NLOS situation.
Center Frequency	2.44 GHz	1.95 GHz	1.95 GHz
Bandwidth	120 MHz	50 MHz	50 MHz
Receiver	On the rooftop of a 11-floor building.	On the rooftop of a 12-floor building.	On the rooftop of a 8-floor building.

---

### 3.3.2 Indoor environments

A schematic diagram of the UWB indoor channel measurement system is shown in Fig. 3-6. An Agilent 8719ET Vector Network Analyzer (VNA) was used for measuring the frequency response of the channel. The transmitted signal is sent from the VNA to the transmitting antenna through a low-loss 10-m coaxial cable. Both the transmitting and receiving antennas (EM-6865) are vertical-polarized and omni-directional in the H-plane. They are biconical antennas covering 2-18 GHz. The signal from the receiving antenna is returned to the VNA via a low-loss 30-m coaxial cable and is amplified by a Low Noise Amplifier (LNA) with a gain of 30 dB connecting to the VNA. The VNA records the variation of 801 complex tones across the 3-5 GHz frequency range, by measuring the S-parameter,  $S_{21}$ , of the UWB channel, which is essentially the transfer function of the channel. The time-domain channel response can be obtained by taking the inverse Fourier transform (IFFT) of the frequency-domain channel response.

UWB propagation experiments were performed in three different floors of Engineering Building Number Four at the National Chiao-Tung University in Hsin-Chu, Taiwan. Figs. 3-7(a)-(d) show the floor layouts of the measurement sites including a laboratory, a classroom, a computer room, and corridors/classrooms, respectively. Room #901 is a laboratory with some equipments and iron tables. The classroom has many

---

wooden chairs and the computer room has ten iron tables and fifty computers. At these sites, all measured points are under the LOS condition. At the last site, the transmitter (Tx) is located at the corridor and 15 measured points are carefully planned to include LOS and NLOS propagations. At each measured point, 64 channel frequency responses were sampled at 64 sub-points, arranged in  $8 \times 8$  square grid, as shown in Fig. 3-7(d). The spacing between two neighboring sub-points is 3.75 cm, which is equal to half wavelength of the center frequency. In each measurement, both the transmitting and receiving antennas are fixed with the same height of 1.6 m.

Here, these 24 measured points are classified into two scenarios, the “Indoor LOS” and the “Indoor NLOS”. The “Indoor LOS” represents all the measurements in the LOS condition, which contains the measured points no.1-no.12. The distance between the transmitter and each receiver is ranged from 2 m to 9 m. The “Indoor NLOS” represents all the measurements in the NLOS condition, which contains the measured points no.13-no.24. The distance between the transmitter and each receiver is ranged from 3 m to 18 m.



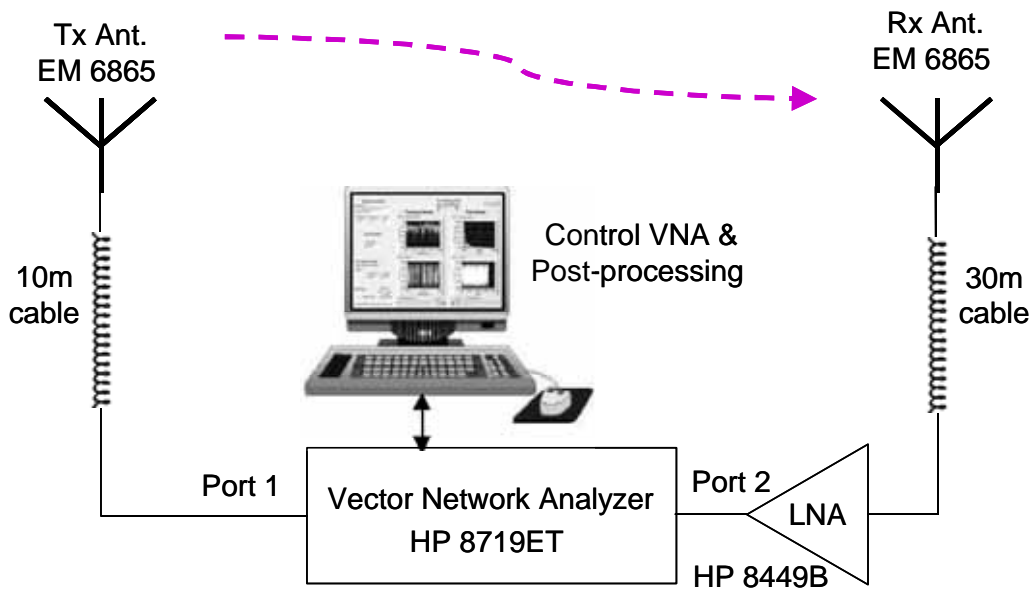


Fig. 3-6 Schematic diagram of the UWB indoor channel measurement system.

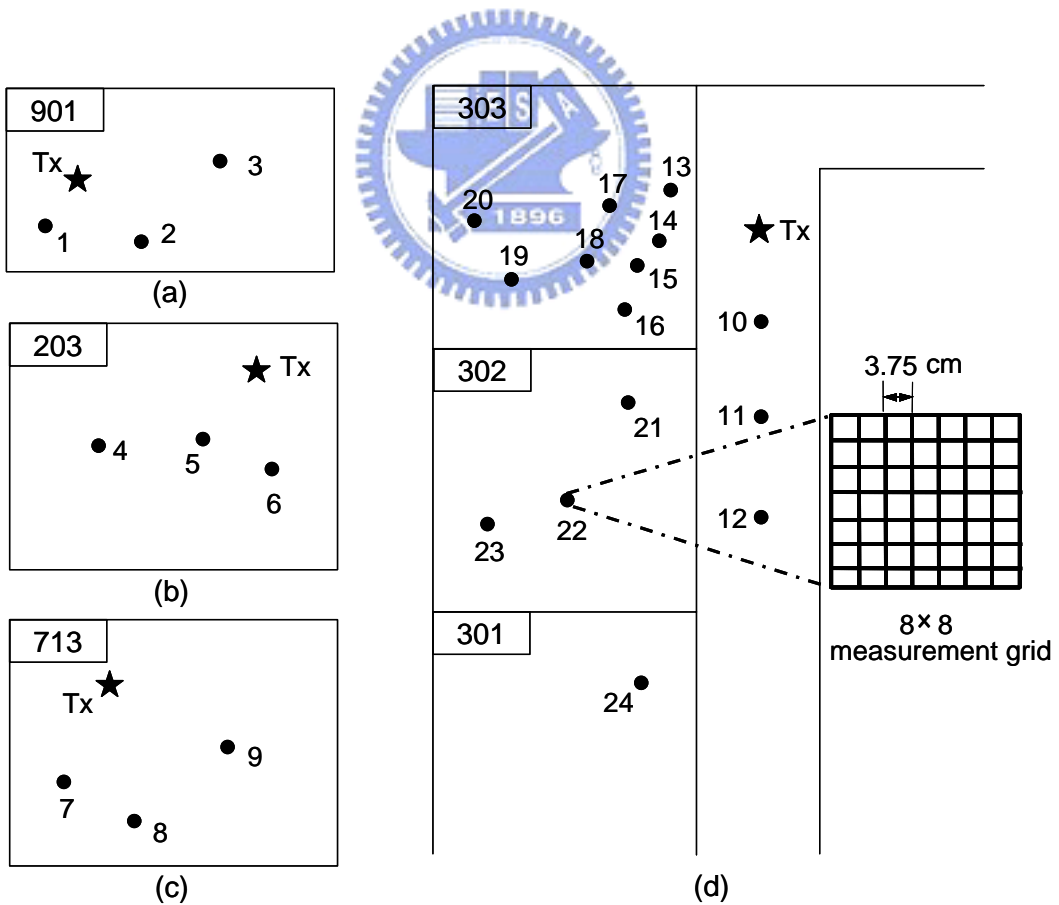


Fig. 3-7 Layouts of four sites where the UWB indoor channel measurements were performed. Locations of the transmitter (Tx) and the receiver are shown by “★” and “●”, respectively.

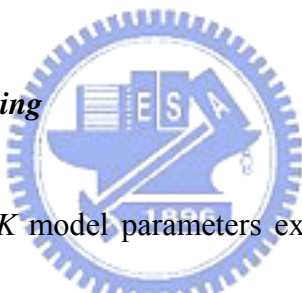
---

## 3.4 Validation and Discussions

It is noted that the  $\Delta$ - $K$  model parameters are extracted from the measured instantaneous power delay profiles (iPDPs) for both outdoor and indoor measurement sites. However, the model parameters of aPDP and amplitude fading are only computed and validated for indoor sites since the small-scale measurements were not performed at outdoor sites.

### 3.4.1 Measurement data processing and analysis

#### A. *Measurement data processing*



Before performing the  $\Delta$ - $K$  model parameters extraction, the measured iPDPs were processed according to the following procedures. It is noted that a propagation path may be undetected in an iPDP due to the amplitude fading. Therefore, to increase the reliability of the estimation, only the iPDPs with large signal-to-noise ratio (SNR) are considered for extracting the  $\Delta$ - $K$  model parameters.

- 1) **Delay translation:** Since the absolute propagation delays of the received signals vary from one location to another, an appropriate delay reference is needed to characterize the relative delays of each path. Here the measured delay time of each iPDP is shifted by the propagation delay, which is equal to  $d/c$ , where  $d$  is the T-R

---

separation distance and  $c$  is the speed of light.

2) ***iPDP selection***: Since the path detection algorithm that shown in the following is in connection with the noise floor, most of the long-delay paths can not be detected for a measured iPDP with low SNR. Here only the measured iPDPs with high SNR (highest peak > noise floor + 20 dB) were selected to extract the model parameters. Therefore, effect of the amplitude fading on model parameters, which is not considered in our approach, is reduced especially for the bins with short delays because of their high powers.

3) ***Path detection***: To detect the presence of a path in any bin, we adopt the approach presented in [11, 22, 38] by choosing a  $\alpha$ -dB threshold relative to the highest peak power in the iPDP. Besides that, the path power must also exceed 6 dB above the noise floor [35] to reduce the influence of noise on path detection. The noise floor for each iPDP is obtained by computing the average power from the portion of the iPDP that is measured before the first MPC arrives. To choose a reasonable value of  $\alpha$ , effects of this value on some channel statistics, such as average mean excess delay, average rms delay spread, standard deviation of rms delay spread, and average number of paths, were analyzed. It is found that the average mean excess delay, average rms delay spread, and standard deviation of rms delay spread, are all in saturation region when the threshold value is larger than around 20 dB for all

---

measurement sites. However, different phenomenon is found for average number of paths, which is increased as the threshold value. It is simply because that larger threshold value will capture more number of paths. However, this increase does not influence the value of the model parameters because of these paths having very low power. For example, when  $\alpha$  is larger than around 20 dB,  $P_i$ ,  $\lambda_i$  and  $k_i$  with small  $i$  will not be changed with  $\alpha$ . Therefore, the relative power threshold value was chosen as 20 dB in this paper.

For the computation of model parameters, the path arrivals of an iPDP is described by a path indicator sequence of “0”s and “1”s, where a “1” indicates the presence of a path in a given bin and a “0” represents the absence of a path in that bin.

Furthermore, for the aPDP and small-scale amplitude fading model parameters extraction, the aPDP of each measured point at indoor sites is computed by averaging the iPDPs sampled at the 64 sub-points.

### ***B. Model parameter extraction***

Here we follow the method proposed by [22] for  $\Delta$ - $K$  model parameters extraction. Compared to the model parameter extracting method using in previous works [11, 13, 20], the method directly describes the bin-by-bin conditional path arrival probabilities and provides an easier mean to calculate the  $\lambda_i$  and  $k_i$ .

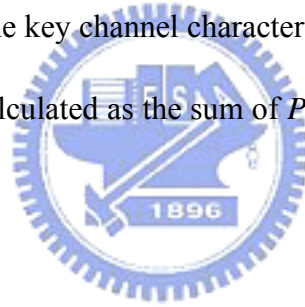
---

In the method, all the selected path indicator sequences of each measurement site were collected to compute the  $\Delta$ - $K$  model parameters through the following procedures:

**1)  $P_i$  computation:**

$$P_i = \frac{N_{1,i}}{N_{total}} \quad (3-13)$$

where  $N_{1,i}$  is the number of points that the path indicator is 1 at bin  $i$ ,  $N_{total}$  is the number of total selected points for this site. It is noted that the average number of paths ( $NP_{\alpha dB}$ ), one of the key channel characteristics for broadband and UWB radio propagations, can be calculated as the sum of  $P_i$ , i.e.,  $NP_{\alpha dB} = \sum_i P_i$ . In this paper,  $\alpha$  is chosen as 20.



**2)  $\lambda_i$  computation:**

$$\lambda_i = \frac{N_{01,i}}{N_{00,i} + N_{01,i}} \quad (3-14)$$

where  $N_{01,i}$  is the number of points that the path indicator is 0 at the  $(i-1)^{\text{th}}$  bin and is 1 at the  $i^{\text{th}}$  bin,  $N_{00,i}$  is the number of points that the path indicator is 0 at both the  $(i-1)^{\text{th}}$  and the  $i^{\text{th}}$  bins.

**3)  $k_i$  computation:**

---


$$k_i = \frac{N_{11,i}}{\lambda_i \cdot (N_{10,i} + N_{11,i})} \quad (3-15)$$

where  $N_{11,i}$  is the number of points that the path indicator is 1 at both the  $(i-1)^{\text{th}}$  and the  $i^{\text{th}}$  bins,  $N_{10,i}$  is the number of points that the path indicator is 1 at the  $(i-1)^{\text{th}}$  bin and is 0 at the  $i^{\text{th}}$  bin.

Furthermore, the model parameters of averaged power decay,  $\gamma$  and  $\Gamma$ , are extracted from the aPDP by the best-fit procedure for each measured point at indoor sites. Finally, the Rician factor is obtained by fitting the cumulative distribution function (CDF) of the 64 subpoints' amplitude to that of a Rician distribution for each measured point at indoor sites.



### 3.4.2 Validation Results

#### A. *Bandwidth on observable multipath-clustering*

Figs. 3-8(a) and (b) illustrates measured and computed  $\lambda_i$  and  $P_i$  of 60MHz-bandwidth signal at the “Urban 1” site, respectively. In these figures, the discrete points of  $\lambda_i$  or  $P_i$  are connected by curves for clarity. The computed  $\lambda_i$  and  $P_i$  are achieved from the measured  $\lambda_j$  and  $P_j$  of 30MHz-bandwidth signal by using (3-5) and (3-6), respectively. The comparison shows that the proposed method yields good prediction accuracy of  $\lambda_i$  with  $m_{e-\lambda} = -0.0632$ ,

---

$\sigma_{e-\lambda} = 0.0906$  and  $P_i$  with  $m_{e-P} = -0.0669$ ,  $\sigma_{e-P} = 0.0922$ . Here,  $m_{e-\lambda}$  and  $m_{e-P}$  represent the mean of the relative error (the ratio of the difference between the computed and the measured data to the measured data) of  $\lambda_i$  and  $P_i$ , respectively.  $\sigma_{e-\lambda}$  and  $\sigma_{e-P}$  are the standard deviations of the relative error of  $\lambda_i$  and  $P_i$ , respectively. For UWB radio propagation in indoor environments, Figs. 3-9(a) and (b) illustrate measured and computed  $\lambda_i$  and  $P_i$ , respectively, of 1GHz-bandwidth signal at the “Indoor NLOS” site. Here, the computed data for 1GHz-bandwidth signal is achieved from the measured data of a signal with 500 MHz bandwidth using (3-5) and (3-6). For conciseness, the results of other sites are not illustrated. In Table 3-2, the values of  $m_{e-\lambda}$ ,  $\sigma_{e-\lambda}$ ,  $m_{e-P}$  and  $\sigma_{e-P}$  for  $n=2$  at all sites are listed. From Table 3-2, it is found that the absolute value of  $m_{e-\lambda}$  and  $m_{e-P}$  are all less than 0.1, which validates our proposed method. The small difference between the measured and the computed parameter values may be mainly due to the amplitude fading which is dependent on the bandwidth and is not considered in our approach. Besides that, the small fluctuation of  $\lambda_i$  and  $P_i$  as shown in Figs. 3-8 and 3-9, also lead some prediction error because it is inconsistent to our assumption that  $\lambda_i$  and  $P_i$  decrease asymptotically with bin number.

For the case of  $n=4$ , Figs. 3-10(a) and (b) illustrates measured and computed  $\lambda_i$  and  $P_i$  of 120MHz-bandwidth signal at the “Urban 1” site, respectively. Here, the computed data for 120MHz-bandwidth signal is achieved from the measured data of a signal with 30 MHz

---

bandwidth. The comparison shows that our proposed method also yields good prediction accuracy of  $\lambda_i$  and  $P_i$  for  $n=4$ . The  $m_{e-\lambda}$ ,  $\sigma_{e-\lambda}$ ,  $m_{e-P}$  and  $\sigma_{e-P}$  for  $n=4$  at all sites are calculated and listed in Table 3-3.

Table 3-4 shows the average number of paths,  $NP_{20dB}$ , which were calculated from the measured and computed results of  $P_i$ , respectively. It is found that the average number of paths is increased as the signal bandwidth is increased. In addition to the  $m_{e-\lambda}$ ,  $\sigma_{e-\lambda}$ ,  $m_{e-P}$  and  $\sigma_{e-P}$  shown in Tables 3-2 and 3-3, the good prediction accuracy of  $NP_{20dB}$  shown in Table 3-4 also validates our proposed method. The mean value of relative errors of  $NP_{20dB}$  are -0.0701 and -0.1551 for  $n=2$  and 4, respectively.

Fig. 3-11 illustrates measured  $k_i$  of 1GHz-bandwidth signal at the “Indoor NLOS” site. It is found that  $k_i$  fluctuates at bins with large bin number. It is noted that for clearly showing the small variation of  $k_i$  at bins with small bin number, the value of  $k_i$  have been clipped at the far right of Fig. 3-11. From (3-15), it is easily understood that the fluctuation of  $k_i$  results from the very small values of  $\lambda_i$ ,  $N_{10,i}$  and  $N_{11,i}$  for bins with long delays. However, these bins are insignificant to the value of channel parameters because of their very low powers. From Figs. 3-9 and 3-11, it is found that  $k_i$  varies slightly at bins with  $\lambda_i \geq 0.1$  (bin number  $\leq 80$ ). Therefore, it is reasonable to use  $\bar{K}$ , which is defined as the mean value of  $k_i$  of the bins with  $\lambda_i \geq 0.1$ , as an index to quantify the observed multipath-clustering.



---

$\bar{K}$  versus bandwidth at both the outdoor and indoor measurement sites are illustrated in Figs. 3-12(a) and (b), respectively. The figures show that  $\bar{K}$  is increased when the signal bandwidth increased, i.e., the wider bandwidth signal yields stronger observable multipath-clustering. It is because that more paths may be resolved due to the finer time resolution of the signal, which increases the probability of clustering occurrence.

In Fig. 3-12(a), it is also found that  $\bar{K}$  value in urban area is larger than that of the suburban area. It is simply because that in urban areas, the scatterers (buildings) are more dense and larger than those of the suburban areas, which leads to a larger chance of multipath components arriving in-group. For indoor environments,  $\bar{K}$  in LOS situation is smaller than that of NLOS situation as shown in Fig. 3-12(b). This is because power of the direct path is much larger than that of the reflected and scattered paths under LOS condition, most part of the grouping paths from scattering and multiple reflections cannot be detected.

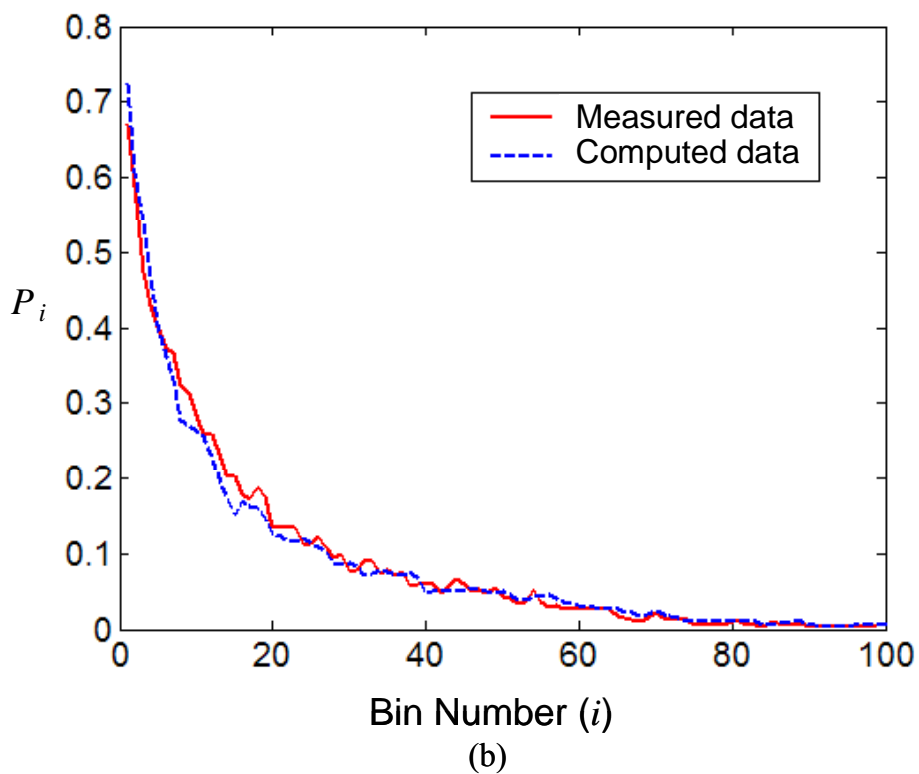
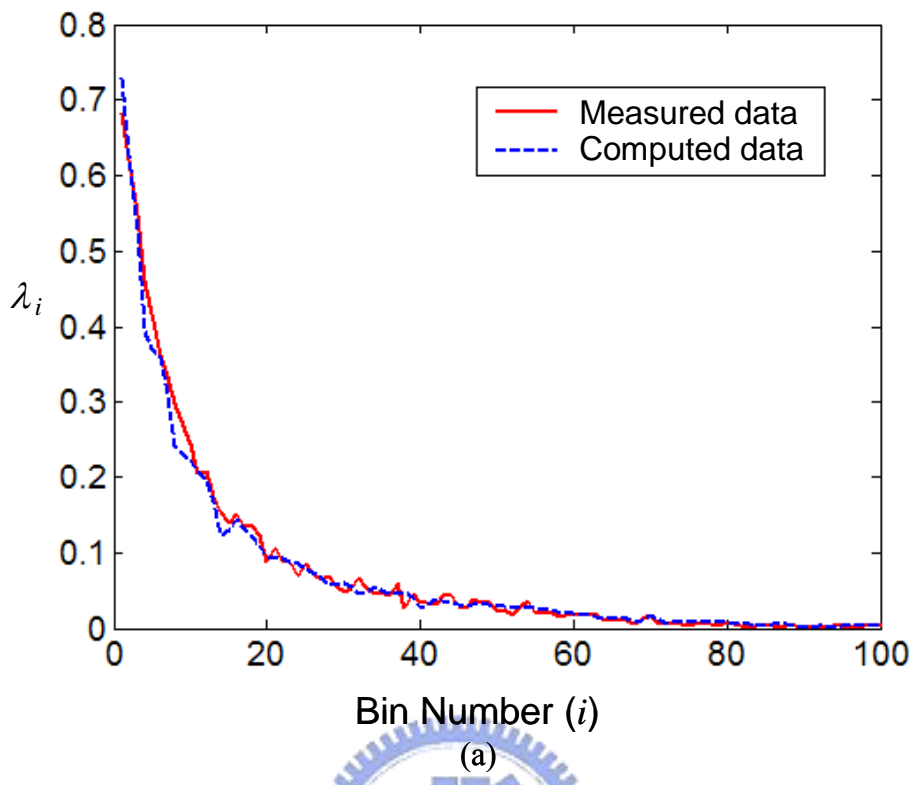


Fig. 3-8 Comparisons of the measured and computed results of (a) the path arrival rate  $\lambda_i$ ; and (b) the path occurrence probability  $P_i$  of “Urban 1” site with 60-MHz bandwidth for  $n=2$ .

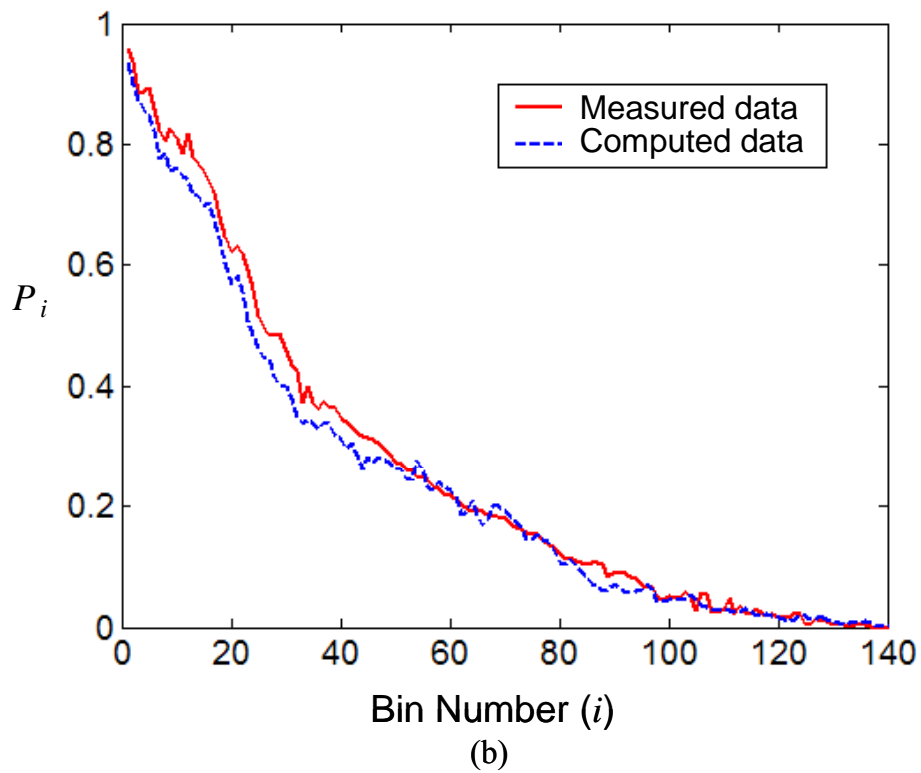
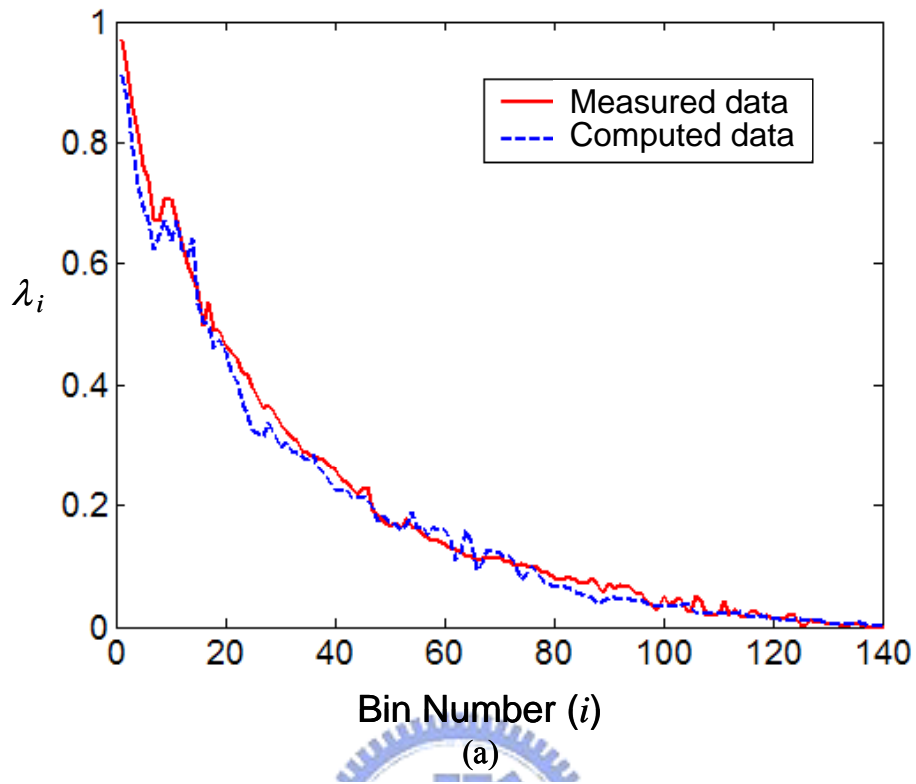


Fig. 3-9 Comparisons of the measured and computed results of (a) the path arrival rate  $\lambda_i$ ; (b) the path occurrence probability  $P_i$  of “Indoor NLOS” site with 1 GHz bandwidth for  $n=2$ .

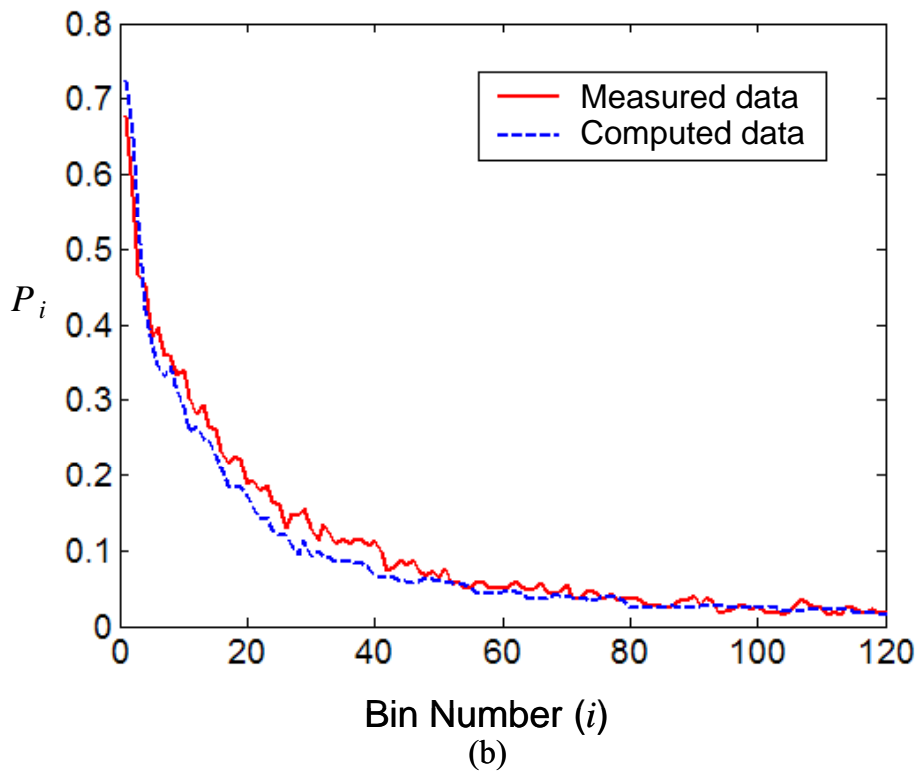
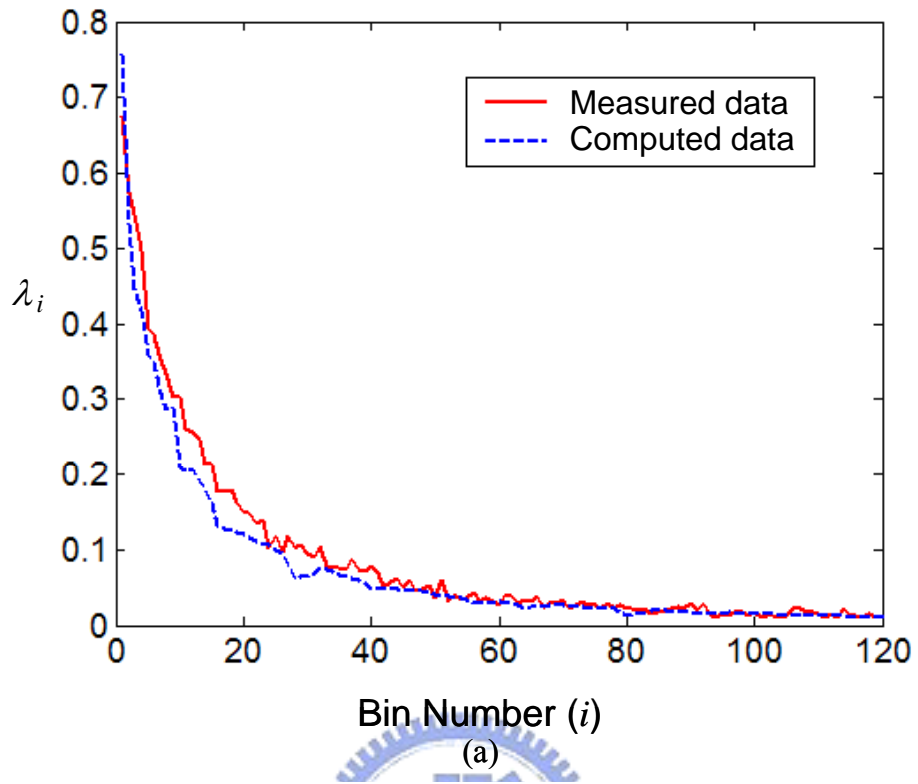


Fig. 3-10 Comparisons of the measured and computed results of (a) the path arrival rate  $\lambda_i$ ; (b) the path occurrence probability  $P_i$  of “Urban 1” site with 120 MHz bandwidth for  $n=4$ .

**Table 3-2 Values of  $m_{e-\lambda}$ ,  $\sigma_{e-\lambda}$ ,  $m_{e-P}$  and  $\sigma_{e-P}$  for  $n=2$ .**

Measurement Sites	Bandwidth ( $F$ )	$m_{e-\lambda}$	$\sigma_{e-\lambda}$	$m_{e-P}$	$\sigma_{e-P}$
Urban 1	120 MHz	-0.0853	0.0902	-0.0790	0.0931
Urban 2	50 MHz	-0.0793	0.0928	-0.0763	0.0911
Suburban	50 MHz	-0.0924	0.1087	-0.0891	0.1012
Indoor LOS	2 GHz	-0.0911	0.1070	-0.0886	0.1031
Indoor NLOS	2 GHz	-0.0786	0.1125	-0.0807	0.1007

**Table 3-3 Values of  $m_{e-\lambda}$ ,  $\sigma_{e-\lambda}$ ,  $m_{e-P}$  and  $\sigma_{e-P}$  for  $n=4$ .**

Measurement Sites	Bandwidth ( $F$ )	$m_{e-\lambda}$	$\sigma_{e-\lambda}$	$m_{e-P}$	$\sigma_{e-P}$
Urban 1	120 MHz	-0.1610	0.1134	-0.1423	0.1197
Urban 2	50 MHz	-0.1539	0.1187	-0.1501	0.1159
Suburban	50 MHz	-0.1711	0.1314	-0.1730	0.1288
Indoor LOS	2 GHz	-0.1643	0.1278	-0.1713	0.1256
Indoor NLOS	2 GHz	-0.1592	0.1309	-0.1625	0.1248

**Table 3-4 Values of measured and computed NP<sub>20dB</sub>**

Measurement Sites	Bandwidth (F)	Measured NP <sub>20dB</sub>	Computed NP <sub>20dB</sub> (computed from measured data @ 1/2×F)	Computed NP <sub>20dB</sub> (computed from measured data @ 1/4×F)
Urban 1	120 MHz	15.4	14.2	13.4
	60 MHz	11.8	11.2	---
	30 MHz	8.5	---	---
Urban 2	50 MHz	13.8	13.0	12.2
	25 MHz	10.6	10.1	---
	12.5 MHz	8.2	---	---
Suburban	50 MHz	12.8	12.0	11.3
	25 MHz	9.3	8.7	---
	12.5 MHz	6.9	---	---
Indoor LOS	2 GHz	25.3	22.8	19.6
	1 GHz	15.8	14.8	---
	0.5 GHz	11.8	---	---
Indoor NLOS	2 GHz	67.3	60.4	54.7
	1 GHz	38.3	35.4	---
	0.5 GHz	24.0	---	---

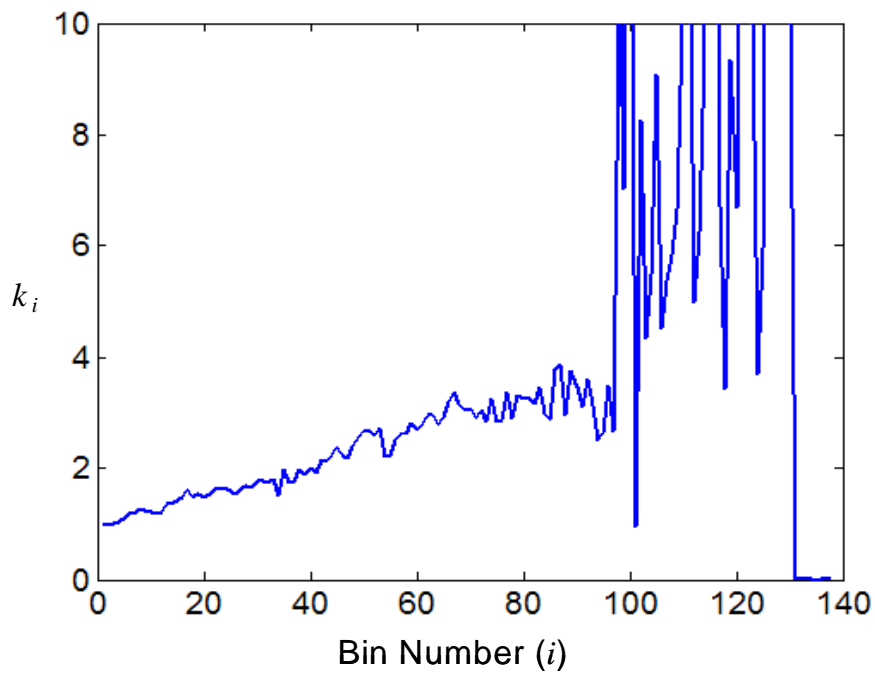


**Fig. 3-11 The measured  $k_i$  of “Indoor NLOS” site with 1 GHz bandwidth.**

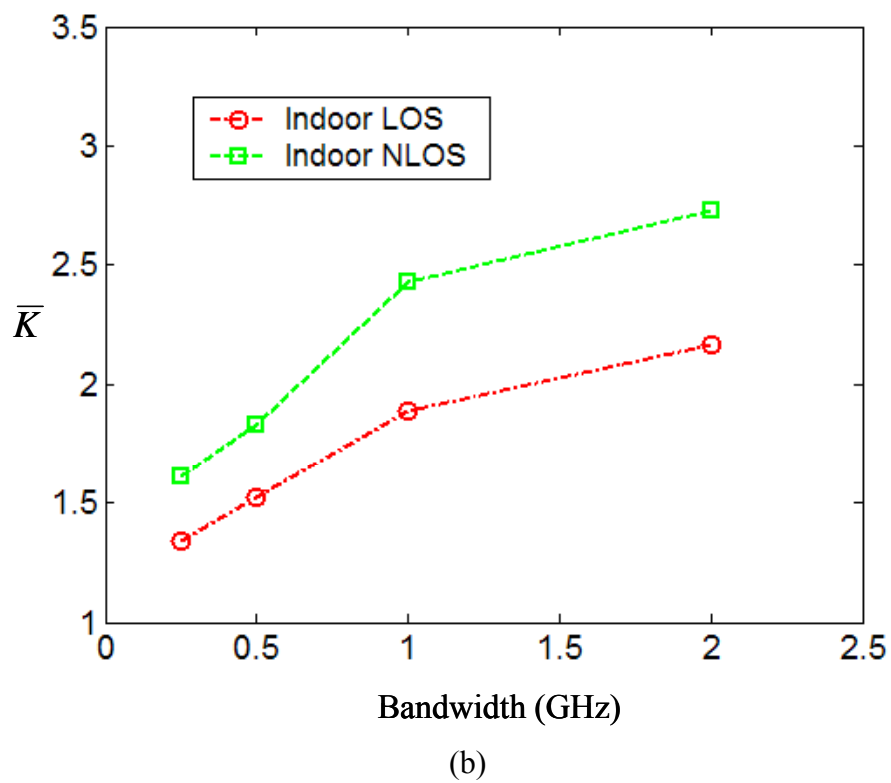
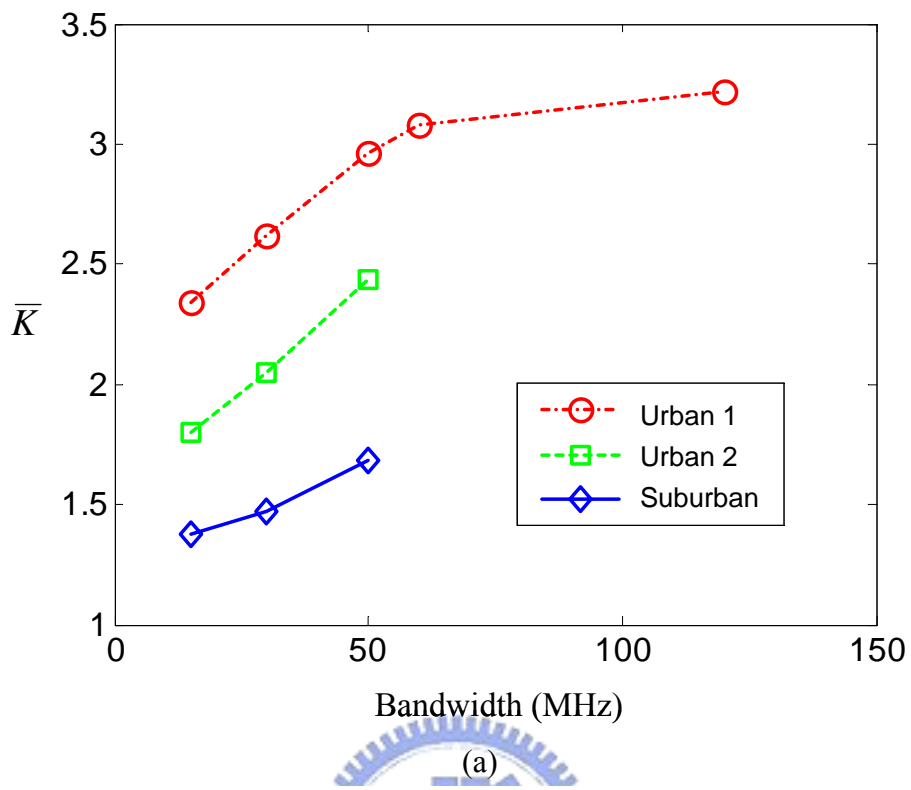


Fig. 3-12  $\bar{K}$  value of the measurement sites: (a) outdoor environments; and (b) indoor environments.

---

### ***B. Bandwidth on multipath power decay and amplitude fading***

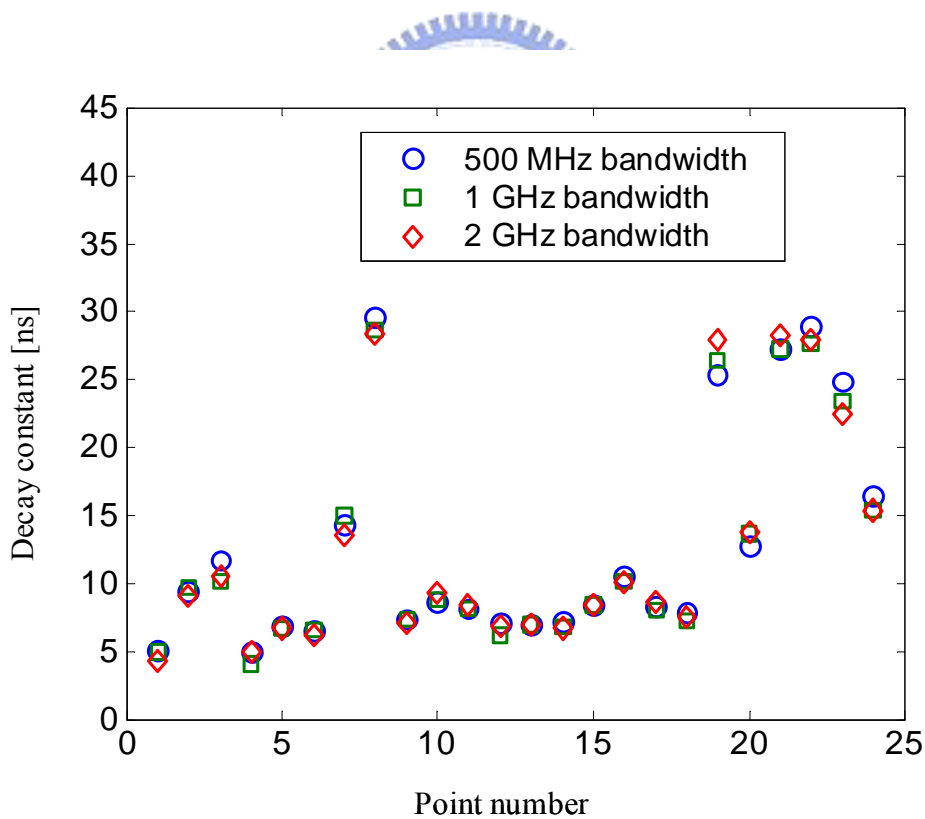
Fig. 3-13 shows the decay constant versus measured point number for the “Indoor LOS” and “Indoor NLOS” sites with signal bandwidths of 500 MHz, 1 GHz and 2 GHz. The comparison shows that the decay constant is independent of the signal bandwidth because that there is only little difference of decay constant value among the three bandwidths at each measured point.

Fig. 3-14 shows the power ratio versus measured point number for the “Indoor LOS” and “Indoor NLOS” sites with signal bandwidths of 500 MHz, 1 GHz and 2 GHz. It is found that the power ratio is decreased when the signal bandwidth is increased, which validates our analytical result as shown in (3-9). Fig. 3-15 shows the measured and computed power ratio for bandwidth of 1 GHz. Here, the computed results are based on the measured results of a 500MHz-bandwidth signal and using (3-11). The comparison shows that our proposed method yields good prediction accuracy of power ratio.

Fig. 3-16 shows the first bin’s Rician factor versus measured point number for the “Indoor LOS” and “Indoor NLOS” sites with signal bandwidths of 500 MHz, 1 GHz and 2 GHz. It is found that the Rician factor is increased when the signal bandwidth is increased for most of the measured points, which validate our analytical result as shown in (3-10). Fig. 3-17 illustrate measured and computed Rician factor for bandwidth of 1 GHz. Here,



the computed data for 1GHz-bandwidth signal is achieved from the measured data of a signal with 500 MHz bandwidth using (3-12). It is found that our proposed method yields good prediction accuracy for the points with low Rician factors, but leads to an overestimation for the points with large Rician factors. However, this kind of difference does not cause significant impact on the small-scale fading statistical properties because that the statistical properties of Rician fading are not very sensitive to large Rician factors [39].



**Fig. 3-13** Decay constant versus measured point number for signal bandwidths of 500 MHz, 1 GHz, and 2 GHz at “Indoor LOS” and “Indoor NLOS” sites.

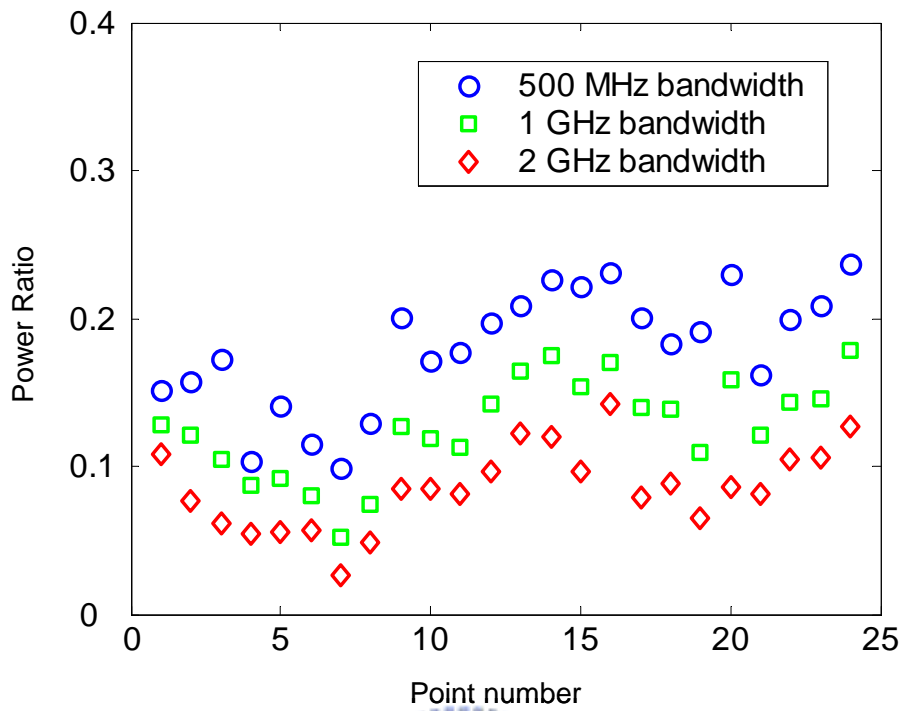


Fig. 3-14 Power ratio versus measured point number for signal bandwidths of 500 MHz, 1 GHz, and 2 GHz at “Indoor LOS” and “Indoor NLOS” sites.

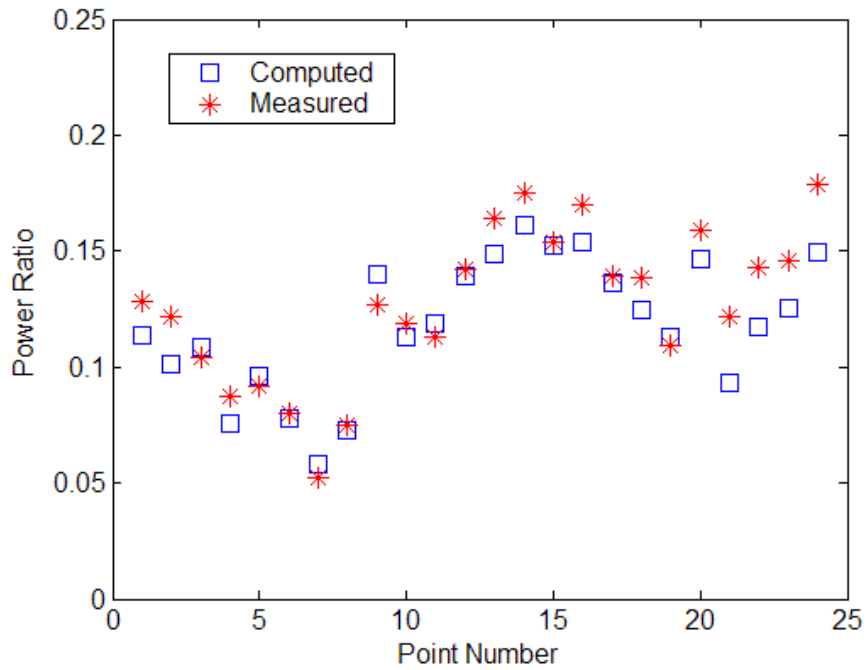
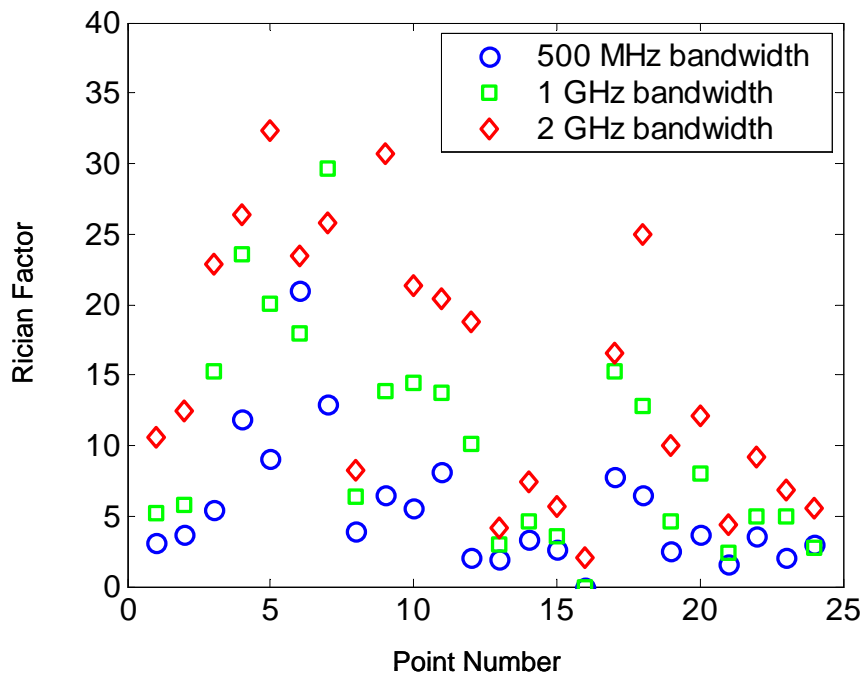
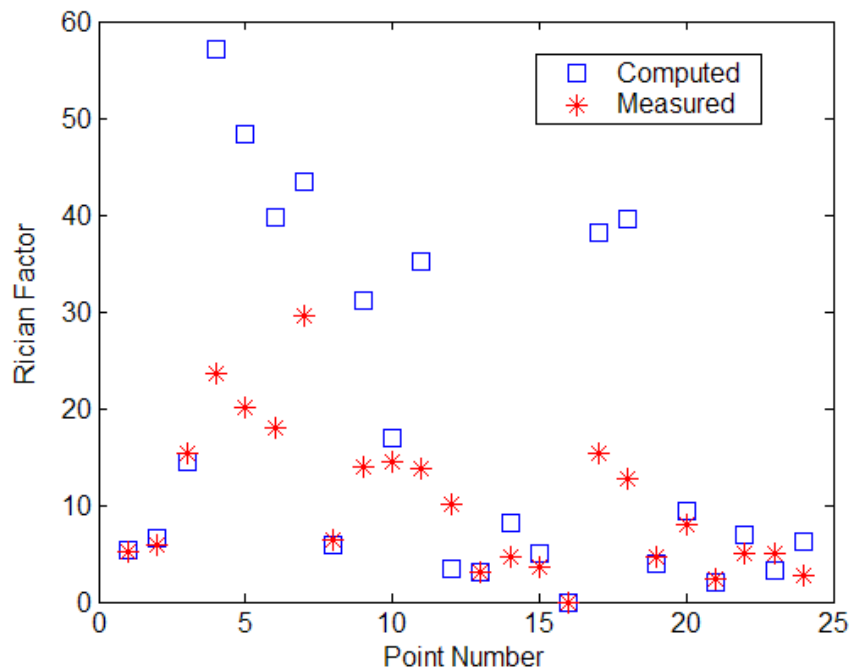


Fig. 3-15 Comparisons between the measured and computed results of the power ratio for all measured points at “Indoor LOS” and “Indoor NLOS” sites with 1 GHz bandwidth.



**Fig. 3-16 Rician factor versus measured point number for signal bandwidths of 500 MHz, 1 GHz, and 2 GHz at “Indoor LOS” and “Indoor NLOS” sites.**



**Fig. 3-17 Comparisons between the measured and computed results of the Rician factor for all measured points at “Indoor LOS” and “Indoor NLOS” sites with 1 GHz bandwidth.**

---

### 3.5 Summary

For a band-limited system, due to the limitation of the signal time resolution, observation of the multipath-clustering is a function of not only the propagation environment but also the signal bandwidth. In this chapter, with the help of  $\Delta$ - $K$  model the effect of signal bandwidth on observable multipath-clustering is investigated by exploring the relationship between  $\Delta$ , signal bin width, and  $\bar{K}$ , an index to quantify the multipath-clustering phenomenon. A formula is derived to show that the signal with larger bandwidth yields finer time resolution and observe more MPCs, which may show stronger multipath-clustering in iPDPs. To completely characterize the time dispersion characteristics of the channel, bandwidth dependencies of multipath averaged power delay profile and amplitude fading are also formulated. Here, a model is applied to characterize the averaged power delay profile with two coefficients, the power ratio and decay constant. In addition, the amplitude fading is described by a Rician distribution function. It is found that (1) the power ratio is decreased when the signal bandwidth is increased; (2) the decay constant is independent of signal bandwidth; and (3) the Rician factor is increased as the signal bandwidth is increased. Our findings are validated by the measurement results of 1.95 GHz and 2.44 GHz broadband signals in metropolitan and suburban areas, and by the results of 3-5 GHz UWB signals in indoors.

---

# **Chapter 4 Measurement and Modeling of Space Correlation for Indoor Wideband MIMO Channels**



**In this chapter, a 3D geometrically based single bounce model (3D GBSBM) that we developed for the space correlation of indoor wideband MIMO channels is introduced. The comparisons between simulated and measured space correlation for spatial/polar arrays are presented.**

---

## 4.1 Introduction

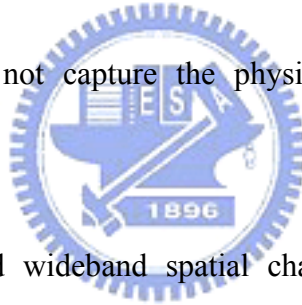
Recently, MIMO technologies have attracted great interest for broadband wireless communication systems due to its potential to provide channel capacity gain without additional bandwidths. Meanwhile, it is well known that to what extent the MIMO capacity can reach depends on the correlations among sub-channels. For the spatial/polar arrays, the correlations among sub-channels are dependent on not only the array spacing but also the antenna polarization.

For MIMO systems operated in indoor buildings, the elevation spectrum must be considered in addition to the azimuth spectrum. However, there is a real scarcity of published models for the elevation spectrum in these environments that are suitable for MIMO system studies. In particular, the combined impact of the polarization characteristics and the elevation spectrum has been given little attention. It is noted that the use of cross-polarized antennas for MIMO systems is now receiving considerable attention since they are able to double the antenna numbers for half the spacing needs of co-polarized antennas.

In [40], an analytical expression for the spatial correlation of uniform rectangular dipole arrays considering elevation spectrum and azimuth spectrum is derived. It shows that the dipole arrays have more spatial correlation than isotropic arrays, if the elevation

---

spread is larger than azimuth spread. In [41], a composite model that takes into account both 2D and 3D propagations for cross polarized channels are proposed and the impact of elevation angle on MIMO capacity is analyzed. It shows that the 3D component captures the environments when the elevation angle power spectrum is significant. The ergodic capacity is very sensitive to the power ratio between 2D and 3D components especially for an environment with low azimuth angle spread. From [40] and [41], it is found that the 3D multipath is significant in correlation among sub-channels as well as the MIMO capacity. However, the analysis results in [40, 41] are based on some assuming stochastic models of angle spectrum, which does not capture the physical property of a specific indoor environment.



In this chapter, a hybrid wideband spatial channel model, which combines the site-specific specular rays with a newly 3D geometric based single bounce model (3D GBSBM) for scattering rays, is presented. Here, the 3D GBSBM is extended from the combination model of the GSBEM and GSBCEM. The region of scatterers for different taps can be modeled by GSBEM, and the effective scatterers located near the transmitting and receiving antennas are modeled by GSBCEM. Based on this model, we derived the per-tap correlation between MIMO sub-channels of spatial/polar arrays and validated by measurements in an indoor environment.

---

## 4.2 A New Model for Wideband MIMO Channel Correlation

To model the indoor propagation channels, which is significant dependent on the layout of the building, a hybrid model is proposed. The hybrid model combines a site-specific deterministic model with a 3D GBSBM statistical model. Here, the former model describes the specular rays, and the latter one is used to model the scattered rays. Based on the hybrid model, the received electric field at time delays of  $\tau_n$ ,  $\vec{E}_t(\tau_n)$ , is determined by a superposition of deterministic and randomly scattered rays, which is given by

$$\vec{E}_t(\tau_n) = \sum_j \vec{E}_{D,j}(\tau_n) + \sum_i \vec{E}_{S,i}(\tau_n) \quad (4-1)$$



where  $\vec{E}_D$  and  $\vec{E}_S$  are the deterministic and randomly scattered rays, respectively.

As (2-3), an UWB/wideband MIMO channel is represented by a channel matrix that is function of delays. Therefore, a useful model for wideband MIMO channels should have the capability to model the channel matrix or correlation matrix for taps with different delays. Fig. 4-1 is an illustration of the per-tap spatial correlation metrics for a 2x2 MIMO channels.

As shown in Section 2.3.1, a nice attribute of the GBSBEM is the physical



interpretation that multipath signals arrived with different delays are accounted by changing the length of the axes of the ellipse. Based on this concept, a three-dimensional geometrically based single bounce ellipsoid model is proposed to model the indoor wideband MIMO channels.

From (4-1), the space correlation of the  $n^{\text{th}}$  tap received signal,  $\rho_t(\tau_n)$ , is given by

$$\rho_t(\tau_n) = \frac{\chi}{1+\chi} \rho_D(\tau_n) + \frac{1}{1+\chi} \rho_S(\tau_n) \quad (4-2)$$

where  $\rho_D$  and  $\rho_S$  are the space correlation resulted by the deterministic and randomly scattered rays, respectively, and  $\chi$  is the power ratio of the deterministic rays to the scattered rays.

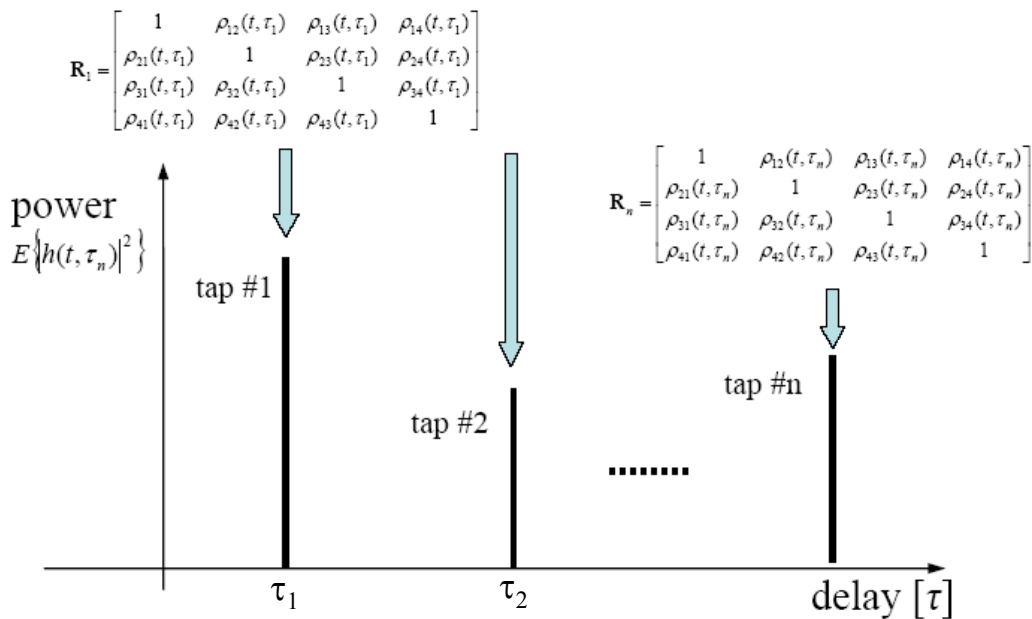


Fig. 4-1 Per tap MIMO correlation metrics.

---

### 4.2.1 3D Geometrically Based Single Bounce Model

Fig. 4-2 shows the geometry of an ellipsoid with axes lengths of  $a$ ,  $b$  and  $c$ . The scatterer lies at coordinates  $(x, y, z)$  on the surface of the ellipsoid satisfy

$$\frac{x^2}{a^2} + \frac{y^2}{b^2} + \frac{z^2}{c^2} = 1 \quad (4-3)$$

As shown in Fig. 4-2, the transmitter and receiver are located at  $(0, 0, -f)$  and  $(0, 0, f)$ , respectively. To keep the propagation distances of every scattered rays caused by the scatterers on the surface of the ellipsoid as a constant value, we let  $a = b$  and  $a^2 + f^2 = c^2$ . From (4-4a) and (4-4b), it is found that the propagation distances of the scattered rays are equal to a constant value, i.e.,  $d_1 + d_2 = 2c/c_0$ , where  $c_0$  is the light speed.

$$d_1 = \sqrt{x^2 + y^2 + (z + f)^2} = \sqrt{a^2 - \frac{a^2}{c^2}z^2 + z^2 + 2fz + f^2} = c + \frac{1}{c}fz \quad (4-4a)$$

$$d_2 = \sqrt{x^2 + y^2 + (z - f)^2} = \sqrt{a^2 - \frac{a^2}{c^2}z^2 + z^2 - 2fz + f^2} = c - \frac{1}{c}fz \quad (4-4b)$$

For wideband channels, the scatterer regions of different taps with time delay of

---

$\tau_n = \tau_0 + n\Delta_d/c_0$  can be modeled as different sub-regions of the ellipsoid with different axes length by  $\tau_n c_0 = 2c$  as shown in Fig. 4-3. Here,  $\tau_0$  is the absolute propagation delay of the direct path between the transmitter and the receiver, and  $\Delta_d$  is the equivalent propagation distance for a delay time which is equal to the bin width.

Furthermore, it is known that the scattering field strength is inversely proportional to the square of the product value of the length from transmitter to the scatterer and the length from the scatterer to receiver. It implies that the local scatterers compared to the far scatterers mainly contribute the scattering field. Therefore, we introduced the concept of the GBSBCM to model the local scatterers around the transmitter and the receiver as shown in Fig. 4-4 and Fig. 4-5. By combining the 3D GBSBEM and GBSBCM, the effective scatterer region for different taps is determined. Furthermore, for simplicity, we use the “effective” scatterers concept in Lee’s model which shows that the scatterer within the effective scatterer region can be represented by uniformly distributed effective scatterers in the outer surface of the scatterer region.

Fig. 4-4(a) shows the effective scatterer region for the first tap. The effective scattering rays caused by the local scatterers around the transmitter arrives the receiver within a small angle spread, which leads large correlation coefficient (almost equal to 1). Furthermore, as shown in Fig. 4-4(b), the effective scattering rays caused by the local scatterers around the receiver is modeled by effective scatterers which is uniformly

distributed on the surface of the ellipsoid with major axis half length of  $c = f + \Delta_d/2$ . It is noted that the field strength of all scattering rays are equal.

Fig. 4-5(a) and Fig. 4-5(b) show the effective scatter region and the effective scatterers, respectively, for the second tap. It is found that the effective scatterers is constrained in a small region of the surface of the ellipsoid with major axis half length of  $c = f + \Delta_d$ , which is different to the case for the first tap. The covered area of the effective region is dependent on the bin width and the tap number, which is derived in the next section.

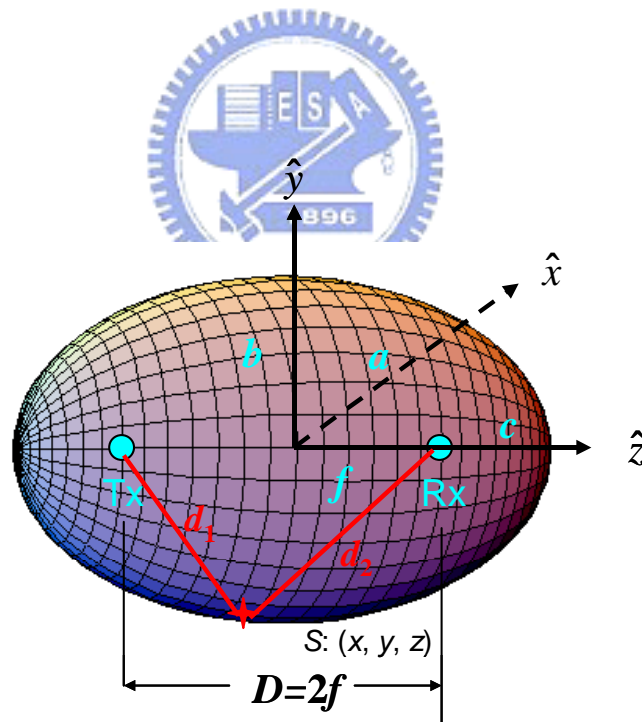


**Fig. 4-2 The illustration of the geometry of the 3D GSBEM.**

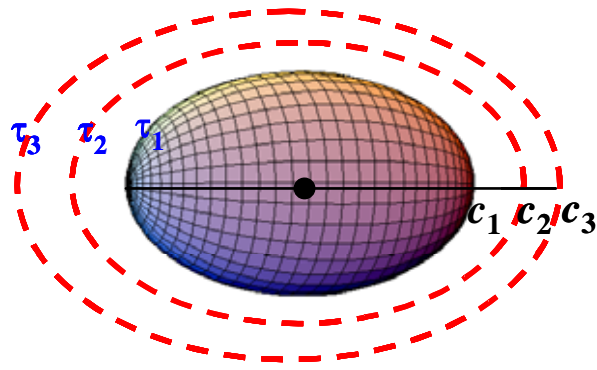


Fig. 4-3 The geometry for the scatter region of different taps.

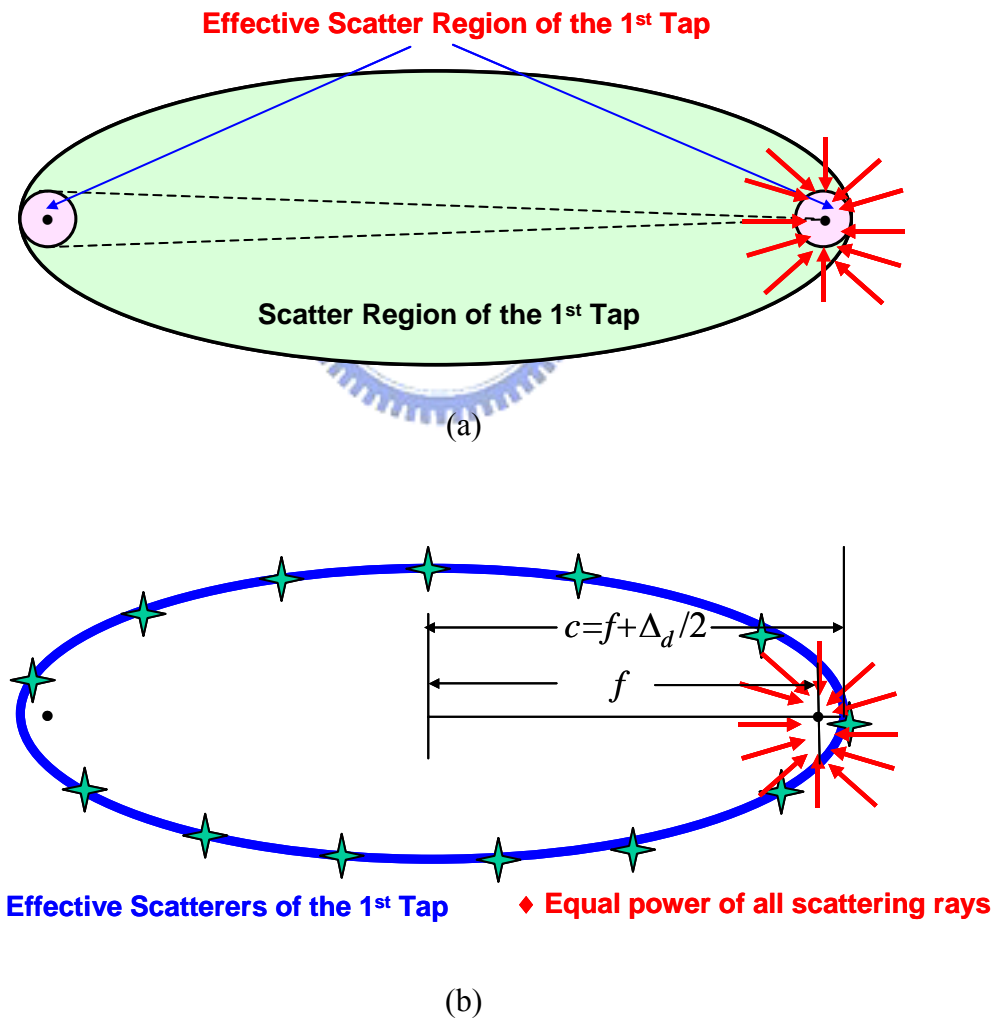


Fig. 4-4 The illustration of the geometry of the 3D GBSBM for the 1<sup>st</sup> tap: (a) the effective scatter region; (b) the effective scatterers.

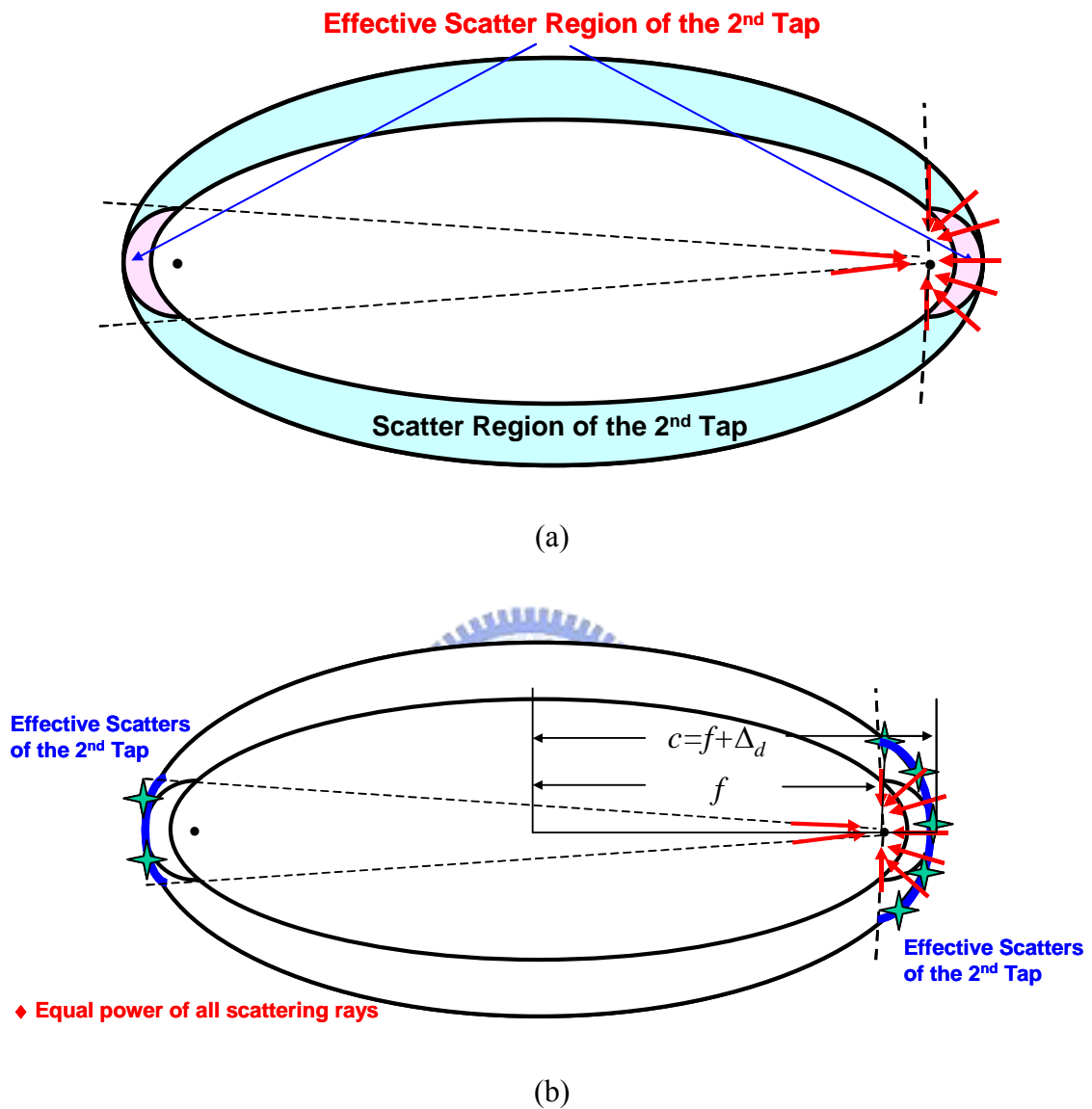


Fig. 4-5 The illustration of the geometry of the 3D GBSBM for the 2<sup>nd</sup> tap: (a) the effective scatter region; (b) the effective scatterers.

#### 4.2.2 Space Correlation of Spatial/Polar Arrays

To derive the spatial correlation of spatial/polar arrays by using the 3D GBSBM, the geometry as shown in Fig. 4-6 is considered. Here, the transmitter (Tx) is located at (0, 0,

-f) and two receivers, Rx1 and Rx2, are located at  $(-\Delta s/2, 0, f)$  and  $(\Delta s/2, 0, f)$ , respectively.

The normalized spatial correlation coefficient between the  $n^{\text{th}}$  tap's receiving signals of Rx1 and Rx2,  $h_1(\tau_n)$  and  $h_2(\tau_n)$ , respectively, is defined as

$$\rho_S(\tau_n, \Delta s) = E \left\{ h_1^*(\tau_n) h_2(\tau_n) \right\} / \sqrt{\Omega_1 \Omega_2} \quad (4-5)$$

where,  $\Omega_1$  and  $\Omega_2$  are power of the power of  $h_1(\tau_n)$  and  $h_2(\tau_n)$ , respectively.

Since the receiving signal is composed of multiple scattering wave with same propagation delay,  $h_1(\tau_n)$  and  $h_2(\tau_n)$  are expressed as

$$h_1(\tau_n) = \sum_{i=1}^N V_{1i} \exp \left\{ j \left[ \varphi_i - \bar{k}_i \cdot \bar{r}_1 - 2\pi f \tau_n \right] \right\} \quad (4-6a)$$

$$h_2(\tau_n) = \sum_{i=1}^N V_{2i} \exp \left\{ j \left[ \varphi_i - \bar{k}_i \cdot \bar{r}_2 - 2\pi f \tau_n \right] \right\} \quad (4-6b)$$

where  $\{V_i\}$ ,  $\{\varphi_i\}$  and  $\{\bar{k}_i\}$  are the amplitude, the phase and the wavenumber vector of the  $i^{\text{th}}$  scattering wave. Since the scattering waves arrive from different direction, the amplitude of the receiving signal is resulted from the inner product of the electromagnetic wave and the antenna polarization vector by

$$V_{1i} = \bar{E}_{1i} \cdot \bar{p}_1 = \left[ E_{1i,\theta}(\theta, \phi) \bar{\theta} + E_{1i,\phi}(\theta, \phi) \bar{\phi} \right] \cdot \bar{p}_1 \quad (4-7a)$$

---


$$V_{2i} = \bar{E}_{2i} \cdot \bar{p}_2 = [E_{2i,\theta}(\theta, \phi)\bar{\theta} + E_{2i,\phi}(\theta, \phi)\bar{\phi}] \cdot \bar{p}_2 \quad (4-7b)$$

where  $\bar{p}_1$  and  $\bar{p}_2$  are the polarization vector of Rx1 and Rx2, respectively.

It is noted that only the effective scatterers around the transmitter and receivers are considered in our model, therefore, we assume the strength of scattering waves are equal for simplicity, i.e.,  $V_{1i} = |E_0|p_1(\theta, \phi)$  and  $V_{2i} = |E_0|p_2(\theta, \phi)$ . Based on this assumption, the  $\rho_S(\tau_n, \Delta s)$  is expressed as

$$\rho_S(\tau_n, \Delta s) = \int_{s \in S_0} p_1(s)p_2(s) \exp\left\{-j \frac{2\pi}{\lambda} \hat{k}(s) \cdot (\bar{r}_1 - \bar{r}_2)\right\} dS_0 \quad (4-8)$$

where  $\hat{k}(s) = 2\pi/\lambda(l_1 - l_2)$ , and  $l_1$  and  $l_2$  are the distance between the scatterer and the Rx1, Rx2, respectively, as shown in Fig. 4-6.  $S_0$  is the surface of the effective scatter region.

Since the two minor axes of the ellipsoid is equal, i.e.,  $a=b$ , the profile of the  $x$ - $y$  plane is a circle, therefore, we transfer the cartesian coordinates to cylindrical coordinates as shown in Fig. 4-7. Then the  $\rho_S(\tau_n, \Delta s)$  in (4-8) is given by (4-9) in cylindrical coordinates.

$$\rho_S(\tau_n, \Delta s) = \frac{1}{A_0} \int_{-c}^c \int_0^{2\pi} p_1 p_2 \exp\left\{-j \frac{2\pi}{\lambda} (l_1 - l_2)\right\} r d\phi dz, \quad n=1 \quad (4-9)$$



---

Since  $x = r \cos \phi$  and  $y = r \sin \phi$ , it gives  $r^2/a^2 + z^2/c^2 = 1$  and then

$$r = \sqrt{a^2 - \frac{a^2}{c^2} z^2} \quad (4-10)$$

Furthermore,  $l_1$  and  $l_2$  is given by

$$l_1 = \sqrt{(r \cos \phi + \Delta s/2)^2 + (r \sin \phi)^2 + (z - f)^2} \quad (4-11a)$$

$$l_2 = \sqrt{(r \cos \phi - \Delta s/2)^2 + (r \sin \phi)^2 + (z - f)^2} \quad (4-11b)$$

For vertical-polarized and horizontal-polarized antenna, the antenna pattern  $p_v$  and  $p_h$  in cylindrical coordinates, respectively, are given by

$$p_v = \sqrt{(r \cos \phi)^2 + (z - f)^2} / \sqrt{r^2 + (z - f)^2} \quad (4-12a)$$

$$p_h = \sqrt{(r \sin \phi)^2} / \sqrt{r^2 + (z - f)^2} \times \sqrt{(z - f)^2} / \sqrt{(r \cos \phi)^2 + (z - f)^2} \quad (4-12b)$$

For the spatial/polar array, antennas of the two receivers may be co-polarized or cross-polarized. The  $p_1$  and  $p_2$  in (4-9) is chosen as  $p_v$  or  $p_h$  based on the antenna polarization of Rx1 and Rx2.

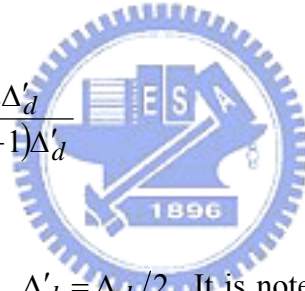
By substituting (4-10), (4-11) and (4-12) into (4-9), the  $\rho_S(\tau_n, \Delta s)$  is obtained. It is

noted in (4-9), the range of the integration in z-axis is from  $-c$  to  $c$ , which is only valid for the case of the first tap. For another cases, the effective scatter region is dependent on the bin width and the tap number.

As shown in Fig. 4-8, the effective scatters are distributed within the region of  $z = [-c, z'_2]$  and  $z = [z'_1, c]$ . From Fig. 4-8, the  $z'_1$  and  $z'_2$  can be found out from  $z_1$  and  $z_2$  by

$$z'_1 = f + (z_1 - f) \frac{n}{(n-1)} \quad (4-13a)$$

$$z'_2 = f - (f - z_2) \frac{2f + n\Delta'_d}{2f + (n-1)\Delta'_d} \quad (4-13b)$$



where  $n$  is the tap number and  $\Delta'_d = \Delta_d/2$ . It is noted that  $z_2 = -z_1$ , and  $z_1$  is obtained by finding the cross point of the  $n^{\text{th}}$  tap's ellipse and the circle centered at  $(0, 0, f)$  with radius of  $n\Delta'$ . From (4-14) and (4-15) and after some derivation,  $z_1$  is given by (4-16).

$$\begin{cases} \frac{z_1^2}{c^2} + \frac{y^2}{a^2} = 1 \\ (z_1 - f)^2 + y^2 = (n\Delta'_d)^2 \end{cases} \quad (4-14)$$

$$\begin{cases} c^2 = f^2 + a^2 \\ c = f + (n-1)\Delta'_d \end{cases} \quad (4-15)$$

---


$$z_1 = \frac{[f + (n-1)\Delta'_d](f - \Delta'_d)}{f} \quad (4-16)$$

For taps of  $n \geq 2$ ,  $\rho_S(\tau_n, \Delta s)$  is given by

$$\rho_S(\tau_n, \Delta s) = \int_{-c}^{z'_2} \int_0^{2\pi} p_1 p_2 \mathbf{exp}\left\{-j \frac{2\pi}{\lambda} (l_1 - l_2)\right\} r d\phi dz + \int_{z'_1}^c \int_0^{2\pi} p_1 p_2 \mathbf{exp}\left\{-j \frac{2\pi}{\lambda} (l_1 - l_2)\right\} r d\phi dz \quad (4-17)$$

It is noted that (4-17) is reduced to the 2D case when the value of  $\phi$  is limited to  $\phi=0$  and  $\phi=\pi$ .

Fig. 4-9 shows the simulated spatial correlation of the co-polarized antenna case by the 2D GBSBEM. Here, we assume  $f=3$  and  $\Delta'_d=0.5$ . It is found that the spatial correlation of the 1<sup>st</sup> tap is smaller than those of the 3<sup>rd</sup> and the 5<sup>th</sup> taps due to its larger angle spread.

Here, the co-polarized antenna case indicates that the transmitting antenna and the two receiving antennas are all vertical-polarized. Furthermore, also for the co-polarized antenna case, the simulated spatial correlations that considered the elevation spectrum are shown in Fig. 4-10. It is found that the larger elevation spread (ES) results lower spatial correlation.

Furthermore, for the cross-polarized antennas case, which indicates that the transmitting antenna and one of the two receiving antennas are vertical-polarized and the other receiving antenna is horizontal-polarized. Figs. 4-11 and 4-12 show the simulated

spatial correlations for the 1<sup>st</sup> tap and the 5<sup>th</sup> tap, respectively. It is found that the spatial correlation is equal to zero when the elevation spectrum is not considered. However, the scattering wave arrives from the elevation plane will depolarized into both the vertical- and horizontal-polarization. Although it results non-zero correlation, but the correlation is much lower than that of co-polarized antenna case. It demonstrates the feasibility of polar arrays to achieve high capacity as well as array compactness.

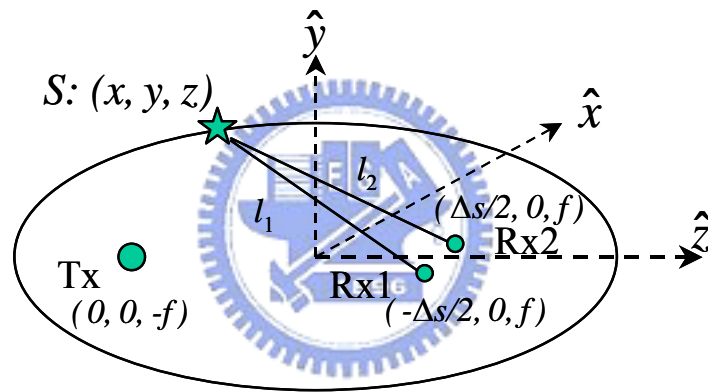


Fig. 4-6 The geometrical configuration of a 1-by-2 channel of the 3D GBSBM.

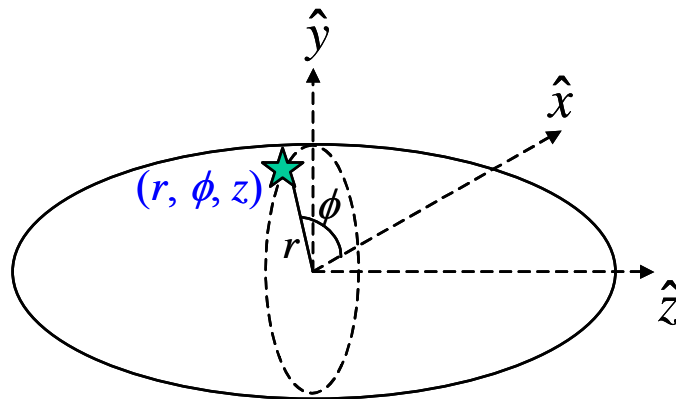


Fig. 4-7 The illustration of the 3D GBSBM in cylindrical coordinates.

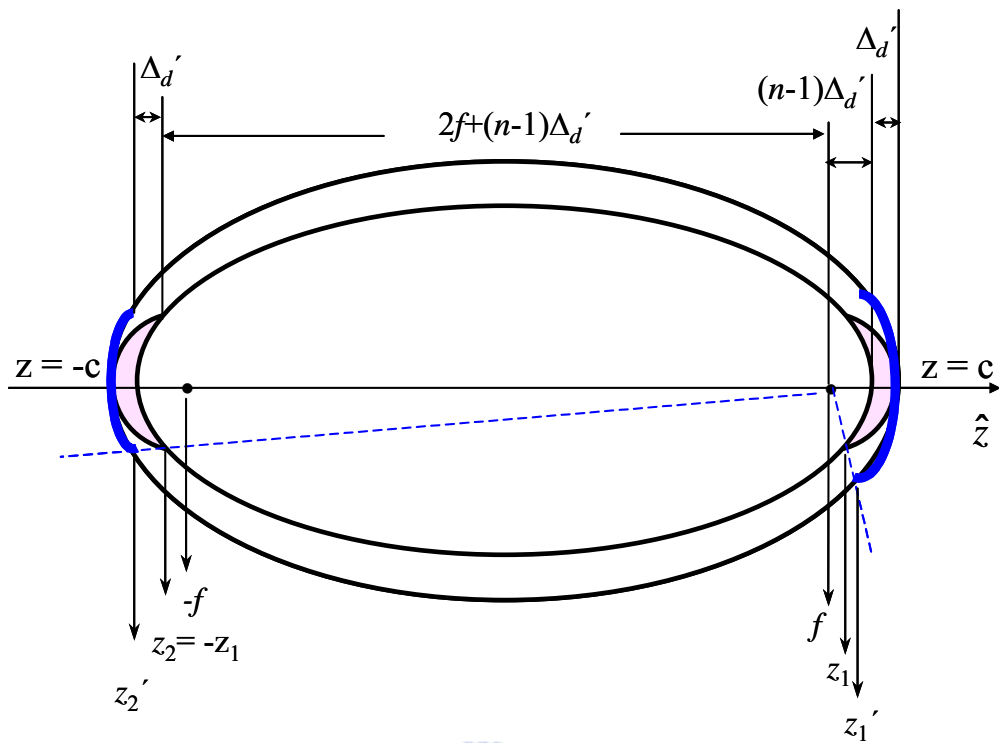


Fig. 4-8 The illustration of the 3D GBSBM for the  $n^{\text{th}}$  tap.

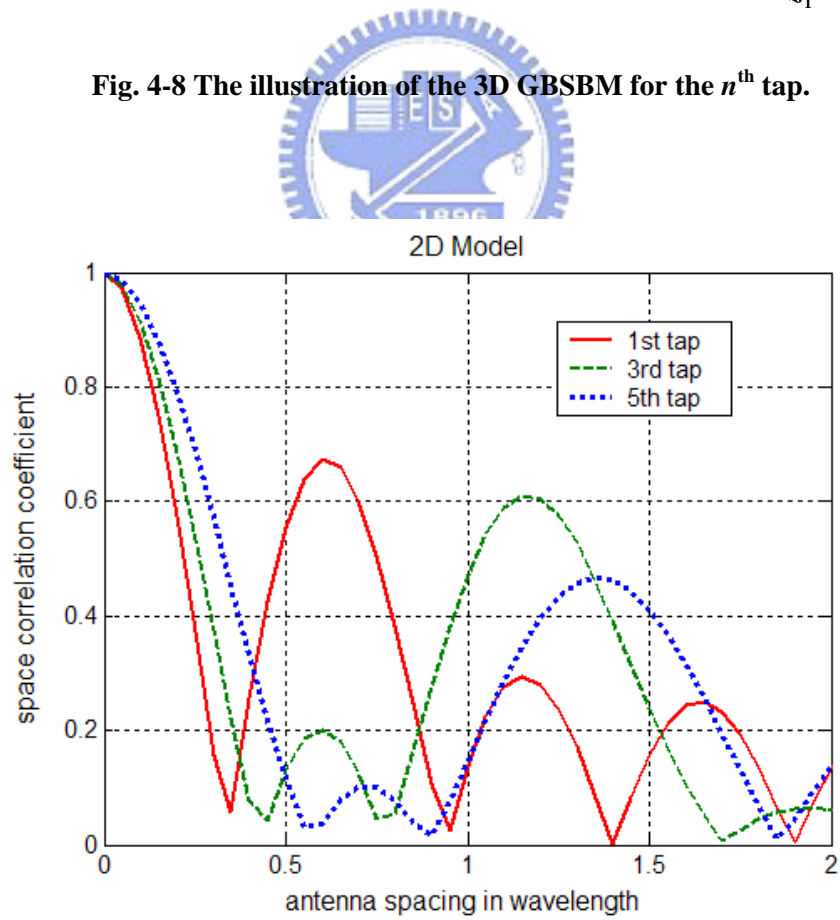


Fig. 4-9 The simulated spatial correlation of the co-polarized antenna case based on the 2D GBSBM.

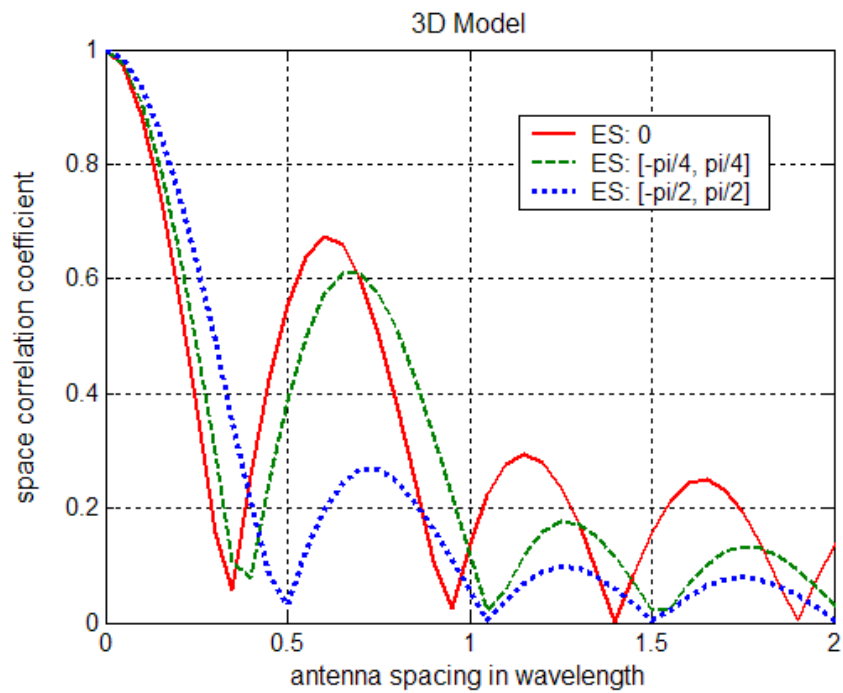


Fig. 4-10 The simulated spatial correlation of the co-polarized antenna case based on the 3D GBSBM for the 1<sup>st</sup> tap.

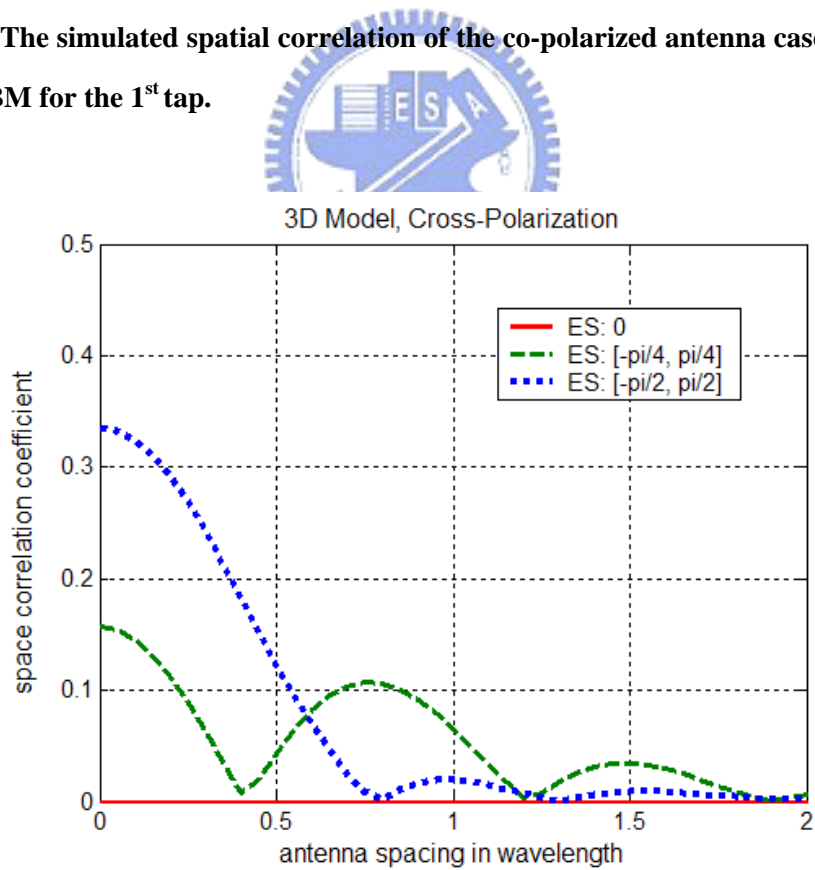


Fig. 4-11 The simulated spatial correlation of the cross-polarized antenna case based on the 3D GBSBM for the 1<sup>st</sup> tap.

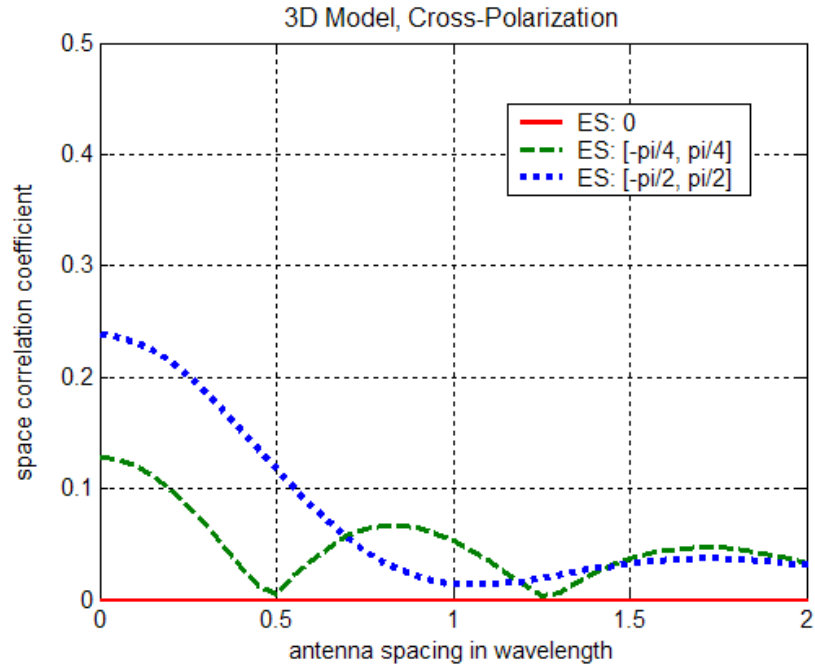
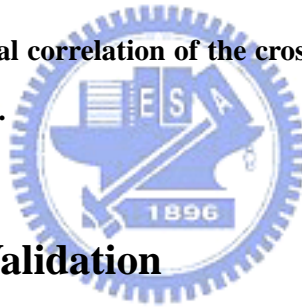


Fig. 4-12 The simulated spatial correlation of the cross-polarized antenna case based on the 3D GBSBM for the 5<sup>th</sup> tap.



## 4.3 Measurement and Validation

### 4.3.1 Measurement Setup and Environment

To validate our proposed model for spatial correlation in indoor environments, wideband MIMO channel measurements were taken in a laboratory at Engineering Building Number Four in the National Chiao-Tung University, Hsinchu, Taiwan. The layout of the measurement site is shown in Fig. 4-13. It shows that there are many scatterers such as partition board, equipments and iron tables in the laboratory.

Fig. 3-4 shows a schematic diagram of the measurement system for wideband

---

single-input-single-output (SISO) channel measurement. An Agilent 8719ET Vector Network Analyzer (VNA) was used for measuring the frequency response of the channel. Here, both transmit (Tx) and receive (Rx) antennas are linear-polarized and omni-directional in the H-plane. In our measurement, channel frequency responses were recorded in the frequency range of 5.1 GHz to 5.8 GHz with 801 frequency components. It implies that the bin width is equal to 1.4286ns and  $\Delta_d=0.4286m$ .

Since the indoor radio propagation channel is nearly time-invariant, MIMO channels are simulated by collecting multiple SISO channel responses measured at different Tx and Rx antenna locations. In our experiment,  $4 \times 16 \times 2$  SISO channel responses measurement were performed. As shown in Fig. 4-14, the Tx antenna is moved to 4 fixed locations with 3-cm spacing between neighboring locations and the Rx antenna is moved to 16 fixed locations with 1.25-cm spacing for each Tx antenna location. Meanwhile, at each Rx antenna location, channel responses were measured for both the vertical- and horizontal-polarized Rx antenna. In our measurement, both the transmitting and the receiving antennas are fixed with the same height of 1.1 m.



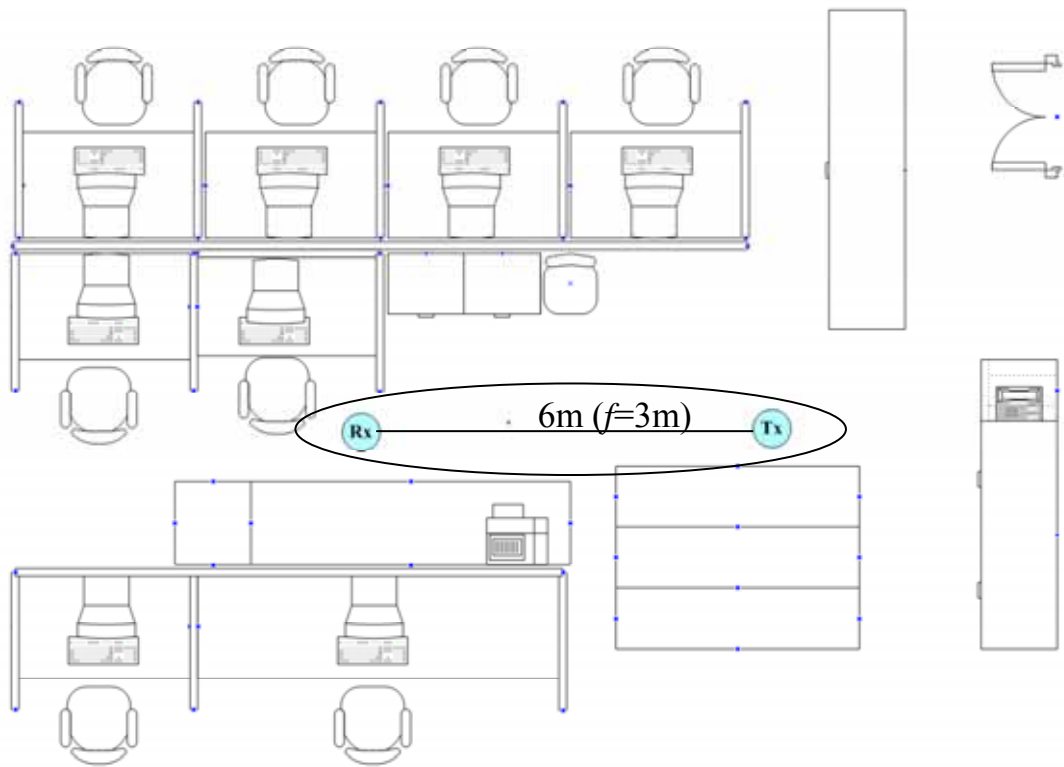


Fig. 4-13 Layouts of the wideband MIMO channel measurement site.

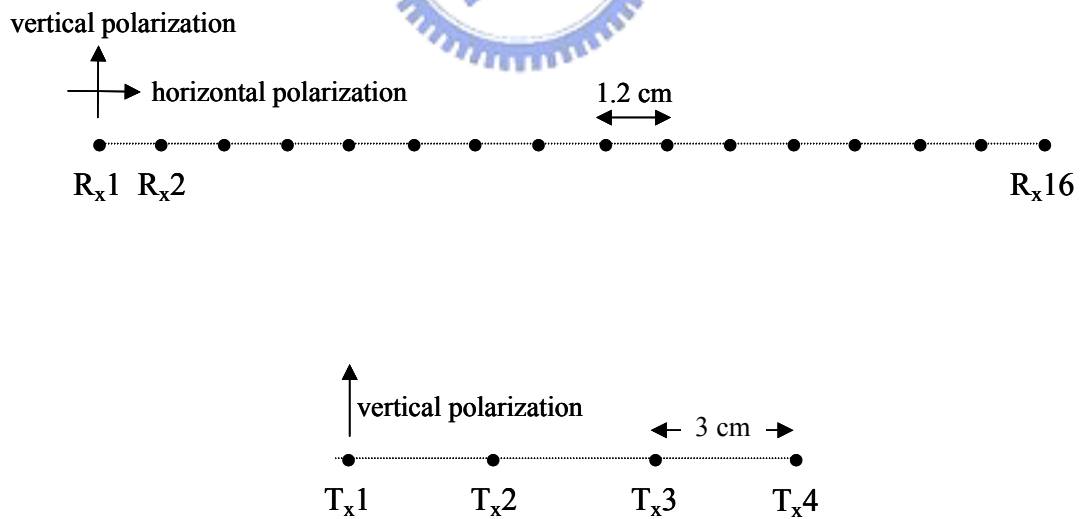


Fig. 4-14 The virtual antenna array configuration for MIMO channel measurements.

---

### 4.3.2 Validation and Discussions

To validate our proposed 3D GBSBM by measurement results, first the parameters of the geometry of the 3D GBSBM should be determined from the measurement setup.

- Distance between the transmitting and the receiving antenna = 6m  $\rightarrow f = 3$
- Bandwidth of measurements = 700MHz  $\rightarrow$  bin width = 1.4286ns  $\rightarrow \Delta_d = 0.4286m$

Based on the  $f$  and  $\Delta_d$ ,  $z'_1$  and  $z'_2$  of the  $n^{\text{th}}$  tap are determined by (4-13a) and (4-13b), respectively. Furthermore, the power ratio  $\chi$  of each tap can be determined by the Rician factor of the amplitude fading, which is obtained from measurement data by curve-fitting method. For example, Fig. 4-15 and Fig. 4-16 show the measured and fitted CDFs of the normalized power of the 1<sup>st</sup> tap and the 2<sup>nd</sup> tap, respectively. It shows that the measured data of the 1<sup>st</sup> tap and the 2<sup>nd</sup> tap are well fitted to a Rician distribution with Rician factor of 1.9 and 0.03, respectively. Since the Rician factor is defined as the power ratio of the specular/LOS path to the scattered multipath, the parameter  $\chi$  of the 1<sup>st</sup> tap and the 2<sup>nd</sup> tap are chosen as 1.9 and 0.03, respectively. Based on these parameters, the simulated and measured spatial correlations of the 1<sup>st</sup> tap and the 2<sup>nd</sup> tap for co-polarized antenna case are shown in Fig. 4-17 and Fig. 4-18, respectively. It is found that the 3D GBSBM combined gives good estimation of spatial correlation compared to the 2D GBSBM. Furthermore, for cross-polarized antenna case, the simulated and measured

---

spatial correlations of the 1<sup>st</sup> tap and the 2<sup>nd</sup> tap are shown in Fig. 4-19 and Fig.4-20, respectively. It is known that if only the 2D GBSBM are considered, the simulated spatial correlation is equal to zero, which is much different to the measured one shown in Fig. 4-19 and Fig. 4-20. Compared to the 2D GBSBM, the 3D GBSBM gives more reasonable results of spatial correlation. From Fig. 4-19 and Fig. 4-20, it is found that the correlation of the 1<sup>st</sup> tap is larger than that of the 2<sup>nd</sup> tap. It is because that the ground reflected ray arrives in the 1<sup>st</sup> tap and leads correlation between vertical and horizontal polarization antennas. Furthermore, it is also found that the simulated spatial correlation is lower than the measured one as shown in both Fig. 4-19 and Fig. 4-20. It may be due to the non-perfect polarization discrimination of the antenna used in measurements, which leads non-zero correlation of the transmitted wave.

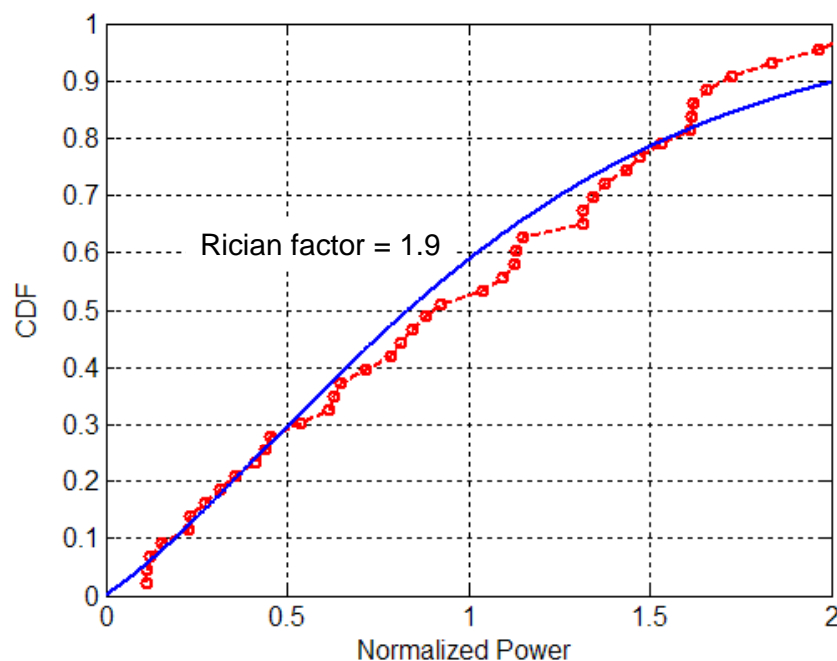


Fig. 4-15 The measured and fitted CDFs of the normalized power of the 1<sup>st</sup> tap.

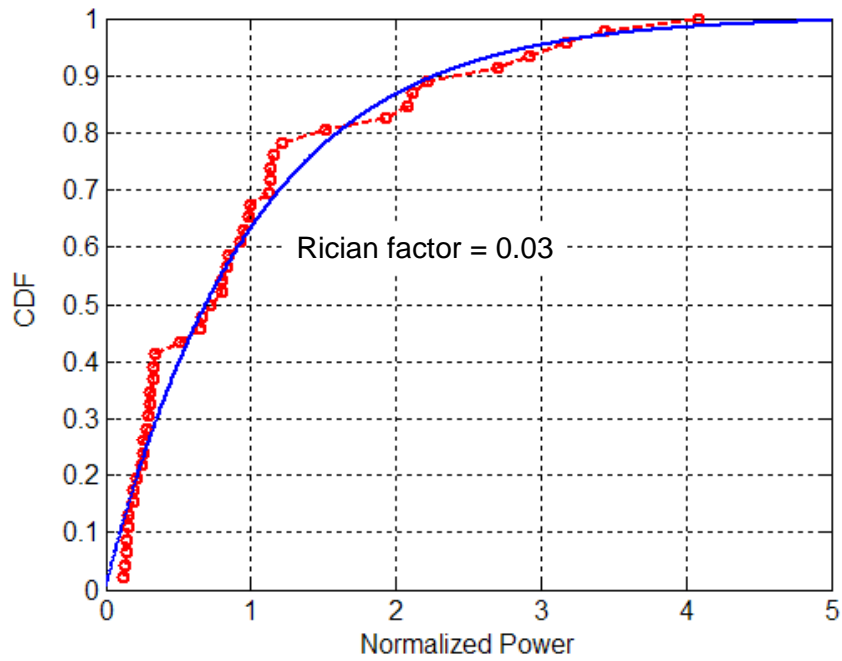


Fig. 4-16 The measured and fitted CDFs of the normalized power of the 2<sup>nd</sup> tap.

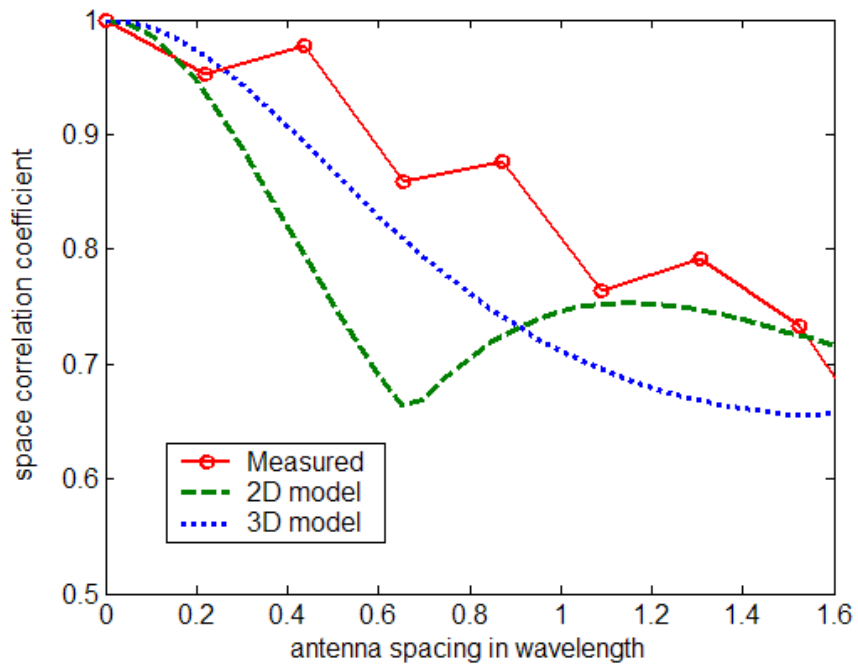


Fig. 4-17 The measured and simulated space correlation of the 1<sup>st</sup> tap for co-polarized

antenna case.

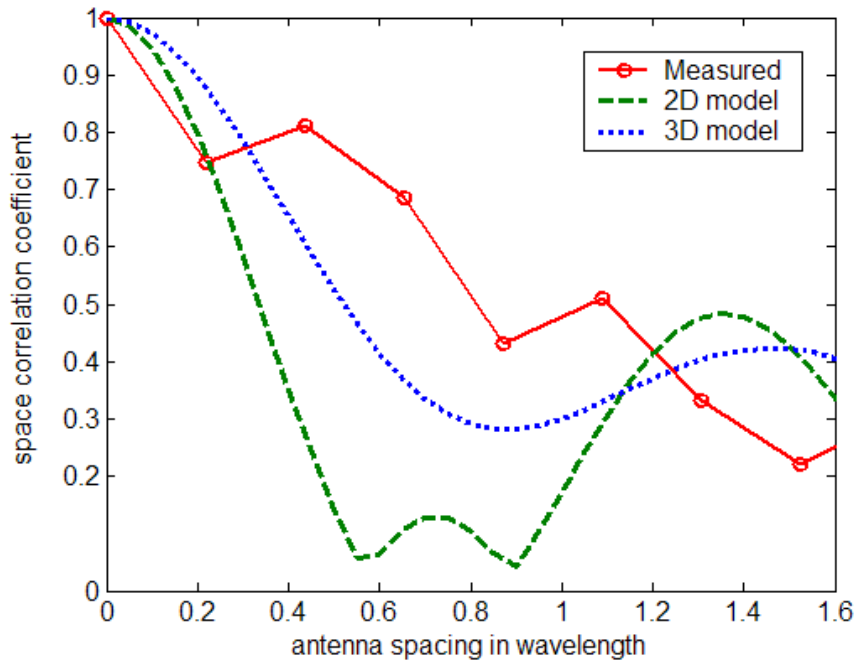


Fig. 4-18 The measured and simulated space correlation of the 2<sup>nd</sup> tap for co-polarized antenna case.

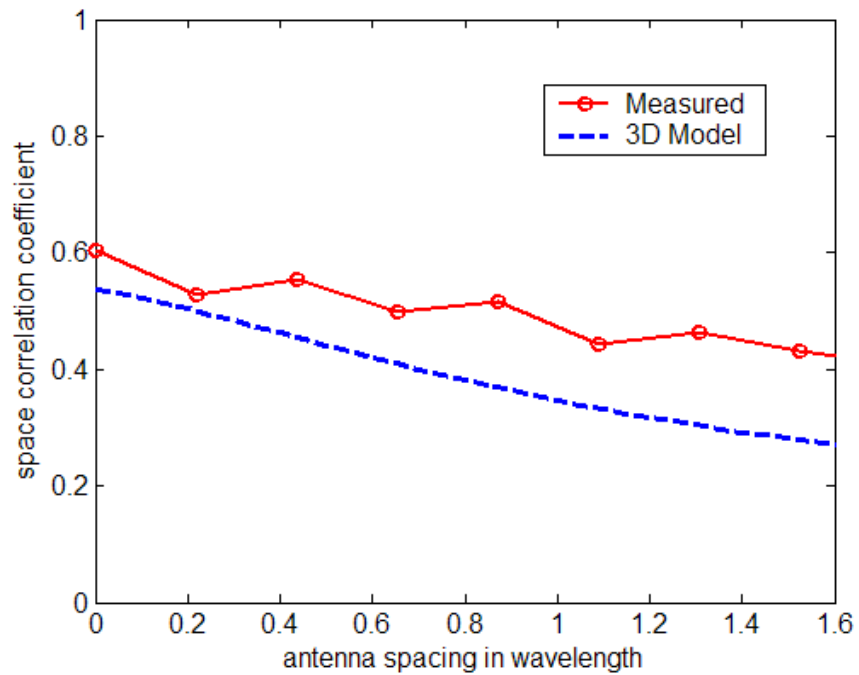


Fig. 4-19 The measured and simulated space correlation of the 1<sup>st</sup> tap for cross-polarized antenna case.

antenna case.

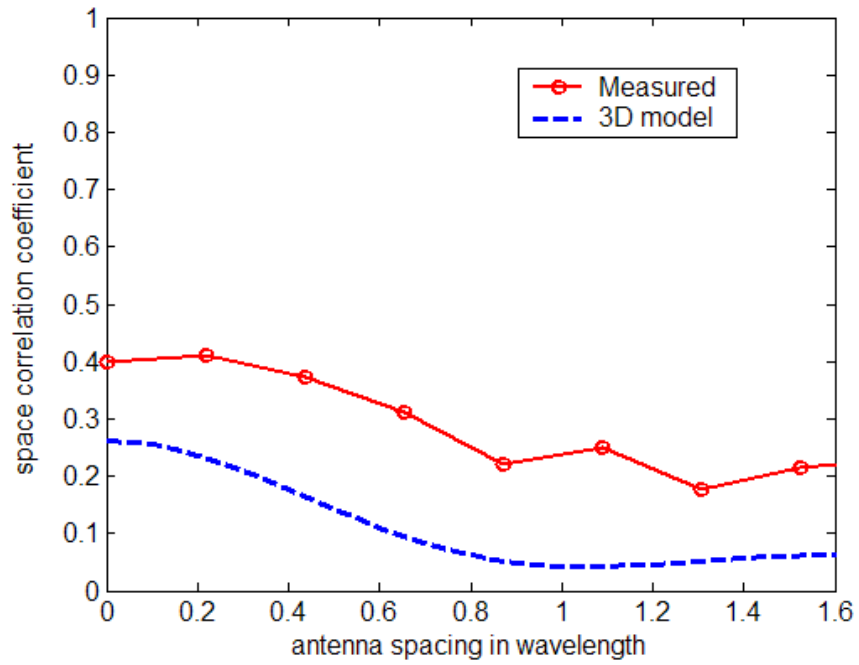


Fig. 4-20 The measured and simulated space correlation of the 2<sup>nd</sup> tap for cross-polarized antenna case.



---

## 4.4 Summary

For MIMO systems operated in indoor environments, the elevation spectrum must be considered in addition to the azimuth spectrum. The azimuth spectrum will give significant influence on the received power and space correlation especially for the cross-polarized antennas.

In this chapter, a hybrid wideband spatial channel model, which combines the site-specific specular rays with a newly 3D GBSBM for scattering rays, is presented. Here, the 3D GBSBM is extended from the combination model of the GSBEM and GBSBCM. From the comparisons between measured and simulated space correlation, it is found that the 3D GBSBM gives more reasonable results compared to the 2D GBSBM for both the co-polarized and the cross-polarized antenna cases. It is because that the elevation spectrum of multipath propagations is considered in the 3D GBSBM.

---

# **Chapter 5    Measurements and Analysis of UWB MIMO Performance for Body Area Network Applications**



**In this chapter, performance of UWB-MIMO in BANs is investigated through measurements for both spatial and polar antenna arrays. From the measured channels, effects of propagation condition, bandwidth, array spacing, and antenna polarization on UWB-MIMO channel capacity are analyzed.**



---

## 5.1 Introduction

Using wireless sensors around the body to monitor health information is a promising new application made possible by recent advances in ultra low power technology [42]. The large diversity and potential of these applications makes it an exciting new research direction in wireless communications. The gain of interest for BAN is confirmed by the IEEE 802.15.6 standardization committee. This group is mandated to develop a physical layer based on the promising UWB radio technologies to provide energy-efficient data communications. In addition to UWB, MIMO technologies have attracted great interest for broadband wireless communications due to its potential to provide channel capacity gain without additional bandwidths. Its use in wide area networks (WAN) and WLAN has been extensively studied [43]. However, to date, the use of MIMO for BAN applications has not been considered.

To our knowledge, measurements of UWB-MIMO channels for BAN were presented in few literatures [44, 45] so far. In [44], MIMO channel characteristics were investigated through measurements with two on-body dual-polar antennas. In the experiment, the array spacing is fixed to one wavelength and the frequency bandwidth is 120 MHz, which is not satisfied the bandwidth requirement of UWB technologies. In [45], the spatial correlation in frequency and delay domains were extracted from channel measurements on the human

---

torso in the frequency ranges of 3-10 GHz. In the experiment, only co-polarized transmitting and receiving antennas are used. Analysis of the MIMO channel capacity is not presented in the literature.

In this chapter, performance of UWB-MIMO for BAN channel capacity improvements is investigated through extensively measurements for both spatial and polar antenna arrays. In our experiments, channel frequency responses were measured in the frequency ranges of 3-10 GHz that covers the whole UWB band. The array spacing is varied from 3 cm to 12 cm. Furthermore, vertical- and horizontal-polarized receiving antennas were used to investigate performance of cross-polarized antennas. From the measured channels, effects of propagation condition, bandwidth, array spacing, and antenna polarization on UWB-MIMO channel capacity are analyzed.

---

## 5.2 Measurement Setup and Sites

In our study, the frequency domain measurement technology to perform UWB BAN indoor channel sounding is adopted. An Agilent 8719ET VNA was used to record the variation of 801 complex tones between the transmitting and receiving antennas across 3-6 GHz, 6-10 GHz and 3-10 GHz frequency ranges, respectively. Here, the UWB antenna is a planar binominal curved monopole antenna [46]. Fig. 5-1 shows the measured antenna return loss versus frequency. As shown, the return loss is below  $-10$  dB from 3 GHz to 10 GHz.



Since our measurements were performed at night, therefore, the measured channel is nearly time-invariant. MIMO channels are formed by collecting multiple SISO channel responses. As shown in Fig. 5-2, the transmitting antenna is moved to 5 fixed sub-points with 3-cm spacing. Meanwhile, for each transmitting antenna sub-point, the receiving antenna is moved to 5 fixed sub-points with 3-cm spacing. In addition, at each receiving antenna sub-point, channel responses were measured for both the vertical- and horizontal-polarized receiving antennas. For each environment, MIMO channel responses are measured at four receiving antenna positions (Rx 1-4) as shown in Fig. 5-2, while the transmitting antenna (Tx) is always placed on the front of the body. Therefore, in our experiment,  $5 \times 5 \times 2 \times 4$  SISO channel measurements were performed at each site. Here, the

---

MIMO channels between Tx and Rx 1-4 are denoted as MIMO\_1-4, respectively. The transmitting and receiving arrays are under LOS conditions for MIMO\_1 and MIMO\_4 cases, while other cases are NLOS conditions.

UWB-MIMO BAN propagation experiments are performed at Microelectronics and Information System Research Center (MISRC) in the National Chiao-Tung University, Hsinchu, Taiwan. Fig. 5-3(a) shows the floor layouts of the measurement sites, Sites A and B, at the lobby of 2nd floor of MISRC. In Sites A and B, measurements were performed at the center and side of the lobby, respectively, to understand the effect of reflected waves caused by the sidewall. Fig. 5-3(b) shows the layout of Site C, laboratory #810 at 8th floor of MISRC. Since there are many computers and tables in laboratory #810, measurement results in this site are helpful to understand the effects of local scatters to UWB-MIMO BAN channels.

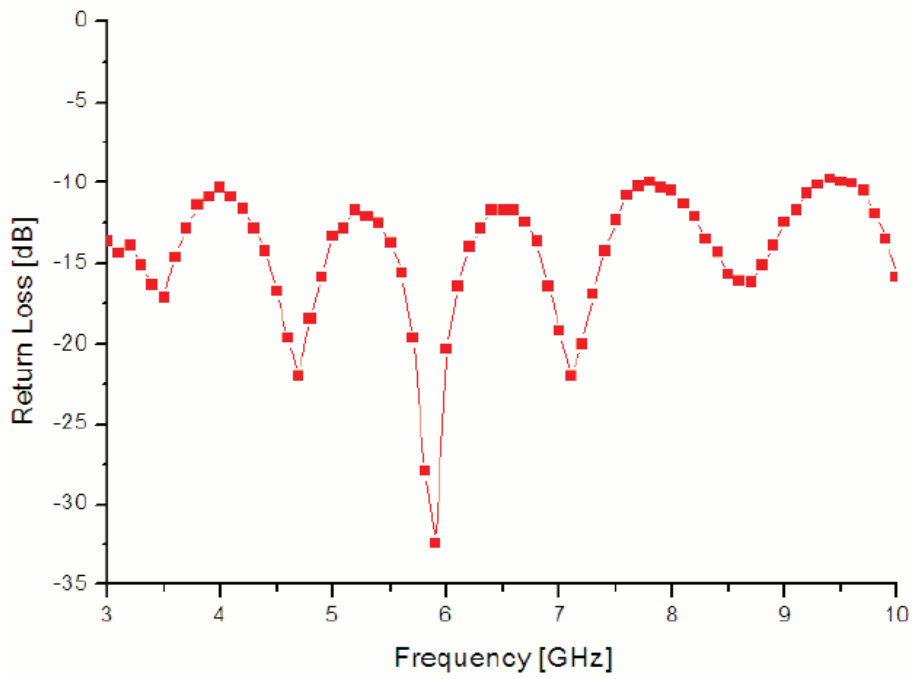


Fig. 5-1 Measured antenna return loss versus frequency.

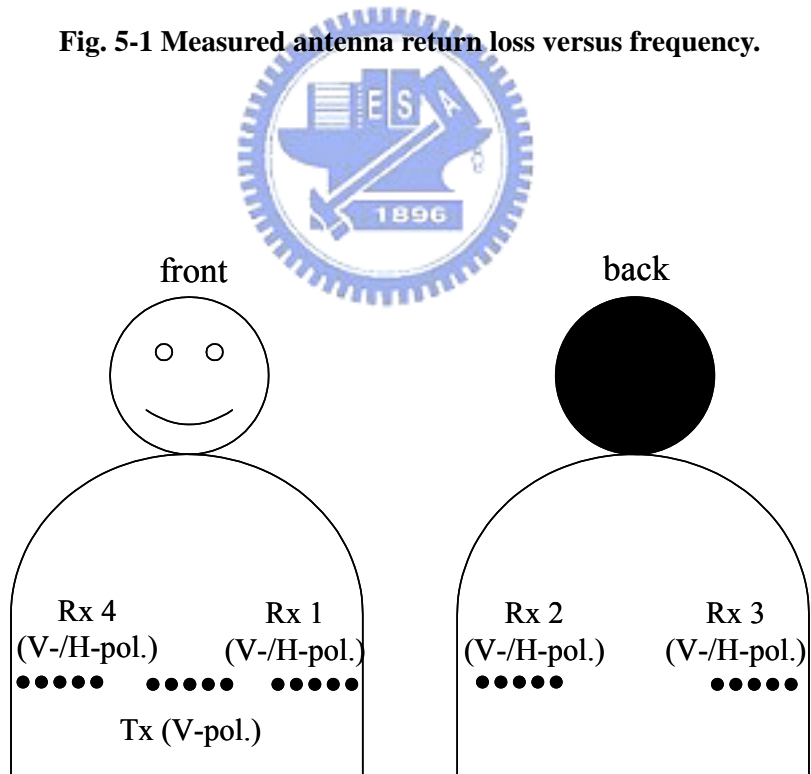
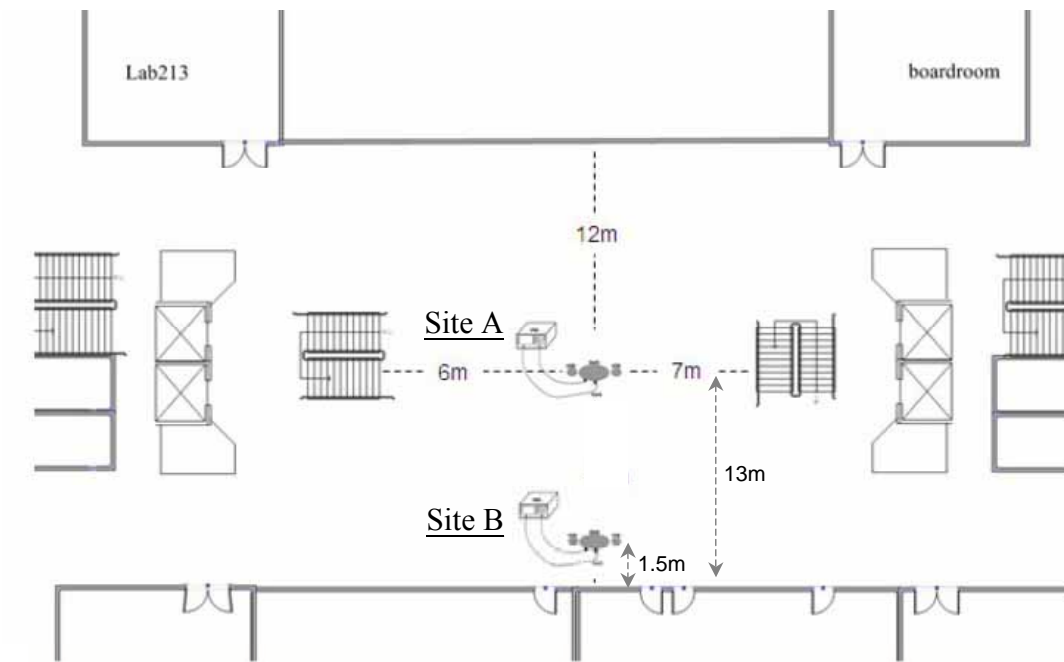
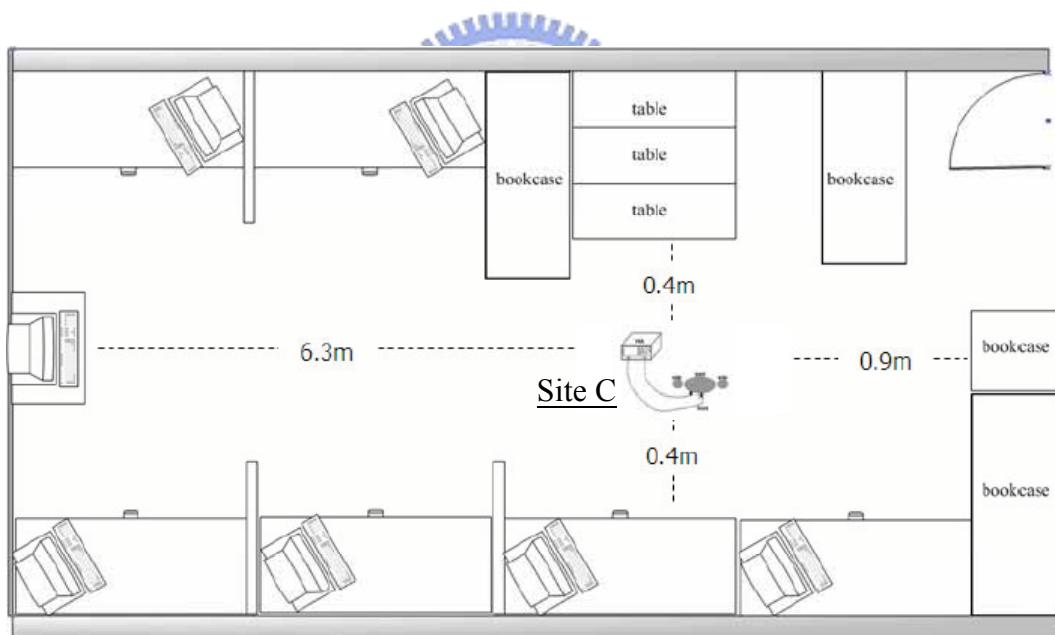


Fig. 5-2 The locations of Tx and Rx antennas for MIMO measurements.



(a)



(b)

**Fig. 5-3 Floor layouts of measurement sites. (a) Sites A and B; (b) Site C.**

---

### 5.3 Observations and Discussions

Given an UWB-MIMO system with  $M$  transmitting elements and  $N$  receiving elements, the UWB-MIMO channel capacity (bits/sec/Hz) is given by [47]

$$C = \frac{1}{N_f} \sum_f^{N_f} \log_2 \left[ \det \left( I_N + \frac{\rho}{M} H(f) H^*(f) \right) \right] \quad (5-1)$$

where  $N_f$  is frequency component  $f$ , which is equal to 801 in our measurements.  $H(f)$  is the normalized frequency-dependent transfer matrix, which is obtained by normalizing the measured transfer matrix to remove the effect of path loss and is given by (5-2). \* denotes the complex conjugation operation, and  $\rho$  is the average SNR over the entire bandwidth. It is noted that  $\rho=20$  dB is given to calculate the UWB-MIMO capacity in the chapter.

$$H(f) = \hat{H}(f) / \sqrt{\sum_{f=1}^{N_f} \|\hat{H}(f)\|_F^2} \quad (5-2)$$

where  $\hat{H}(f)$  is the measured transfer matrix.

---

### 5.3.1 Effect of Propagation Condition

Fig. 5-4 shows the 2×2 MIMO channel capacity for frequency band of 3-10 GHz. Here, both the array spacing at transmitting and receiving side are equal to 3 cm, i.e., around 0.45 times of wavelength of the center frequency. It is found that channel capacities of MIMO\_2 and MIMO\_3 cases are greater than that of MIMO\_1 and MIMO\_4 cases. It is because that MIMO\_2 and MIMO\_3 cases are NLOS situations of rich multipath, which leads to lower correlation among sub-channels than those of MIMO\_1 and MIMO\_4 cases. For example, the average correlation coefficient for 3-cm array spacing is equal to 0.6129, 0.3859, 0.1883 and 0.6216 for MIMO\_1-4, respectively, at Site A. It is noted that, similar results were found at Sites B and C.

From Fig. 5-4, it is also found that the channel capacity is slightly dependent of the measurement sites for NLOS cases. It shows that body-diffracted/refracted waves leads low correlation between sub-channels, the large number of reflected multipath components of Site B and Site C does not give significant contribution on MIMO channel capacity for MIMO\_2 and MIMO\_3. However, for LOS cases, it shows that the channel capacity of Site A is lower than those of Sites B and C. It is because there are very few scatterers around the transmitter and receiver at Site A, LOS path leads high correlation between sub-channels and low channel capacity.



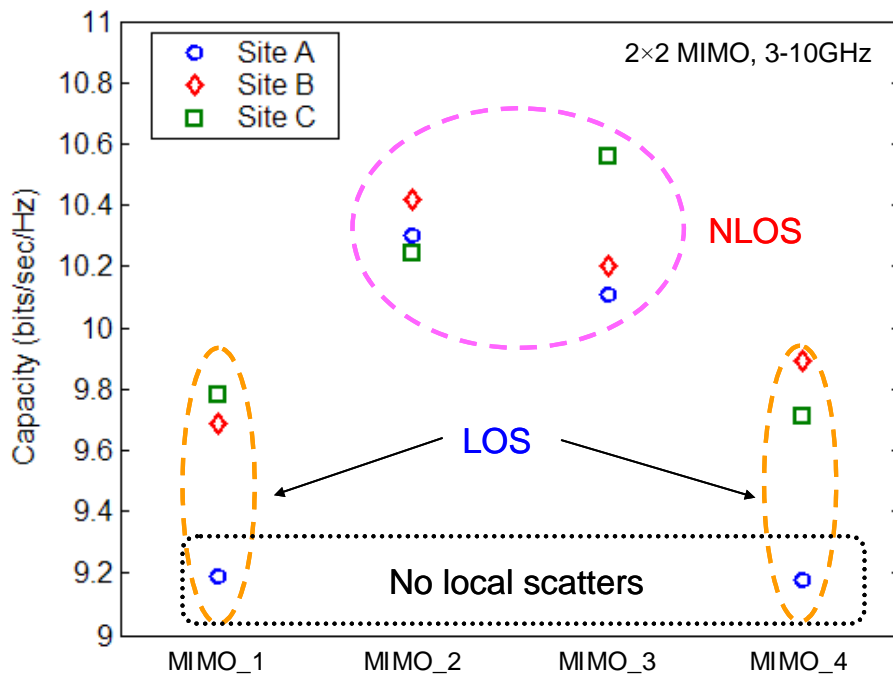


**Fig. 5-4 The measured 2x2 MIMO channel capacity at different sites for frequency band of 3-10 GHz.**



### 5.3.2 Effect of Bandwidth

Fig. 5-5 shows the measured channel capacity versus frequency band at Site C. Here, the number of array elements is 2x2, and the array spacing is 3 cm. It is found that the MIMO channel capacity decreased with frequency or bandwidth. It is because the receiving power is decreased when the frequency band is increased, which can be found in Fig. 5-6. For UWB MIMO, the channel capacity is equal to the average of the multiple narrowband channel capacity. Therefore, high frequency components do not give significant contribution to the channel capacity due to its low power.

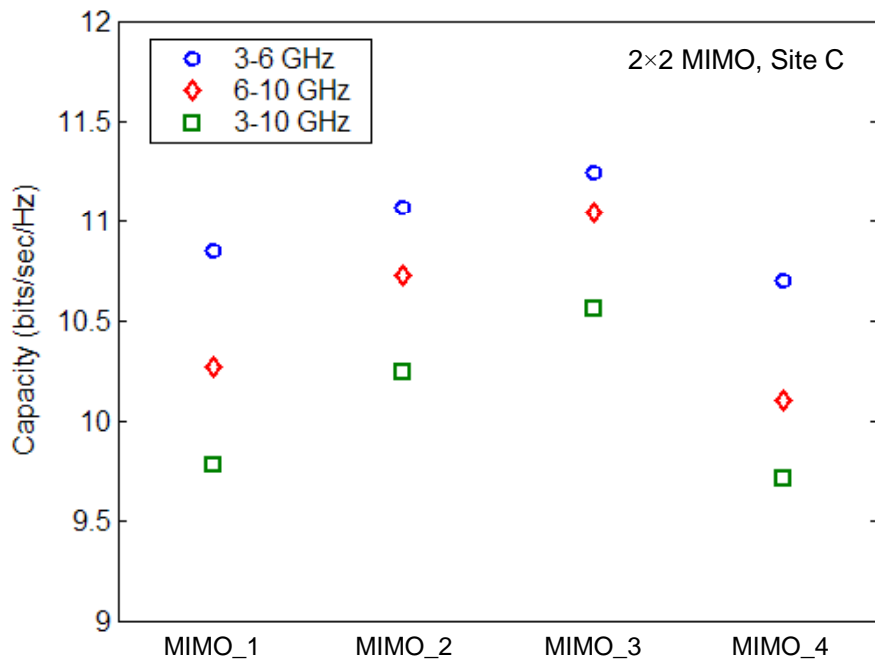


Fig. 5-5 The measured 2x2 MIMO channel capacity at site C.

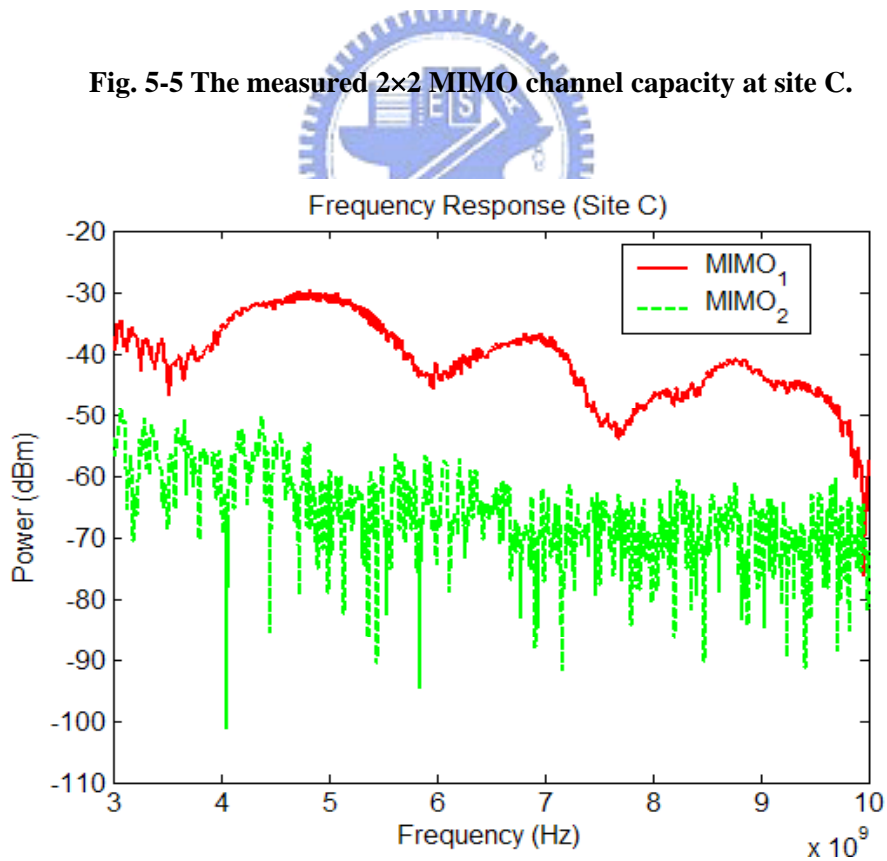


Fig. 5-6 One sub-channel frequency response at Site C.

---

### 5.3.3 Effect of Array Spacing

Fig. 5-7 shows the 2×2 MIMO channel capacity versus receiving array spacing at Site A. Here, the measured bandwidth is in the range of 3 to 6 GHz. From this figure, it is found that the MIMO channel capacity is decreased when the receiving array spacing is increased for most of the MIMO channels. This phenomenon is different from the result observed in WANs and WLANs. For MIMO channels, the capacity is dependent on the correlations among sub-channels and power distribution of received sub-channels. It reaches its maximum value when these sub-channels are uncorrelated and are of equal mean power. The following two figures may illustrate the mechanism to yield the result shown in Fig. 5-7.

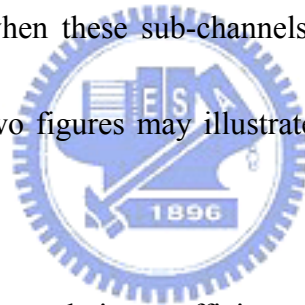
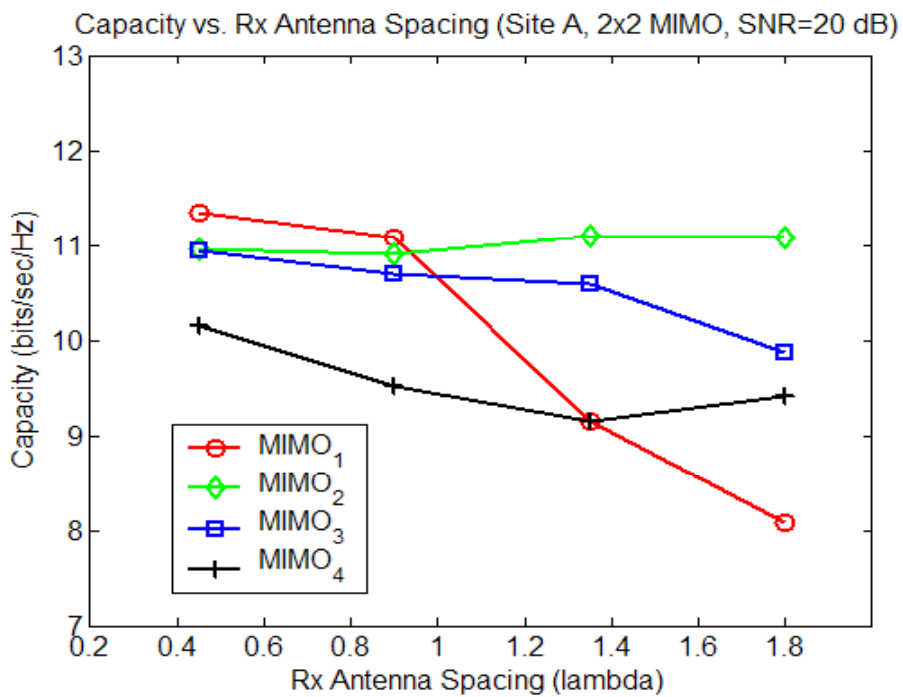


Fig. 5-8 shows the spatial correlation coefficient versus receiving array spacing at Site A. It is found that the spatial correlation coefficient is decreased when the array spacing is increased, which has different trend as that shown in Fig. 5-7.

Fig. 5-9 shows the maximum power difference among the sub-channels versus the array spacing. It is found that the maximum value of the power difference between any two sub-channels is increased when the array spacing is increased. Therefore, some sub-channels with small-received power do not contribute to the MIMO channel capacity even when they are uncorrelated to one another. It shows the reason why the MIMO

channel capacity of BAN is decreased when the array spacing is increased. In other words, increasing of the MIMO capacity by increasing of array spacing does not work in the BAN despite the spatial correlation coefficient is decreased. It is noted that similar results can be found in Sites B and C.



**Fig. 5-7 MIMO channel capacities versus receiving array spacing at Site A.**

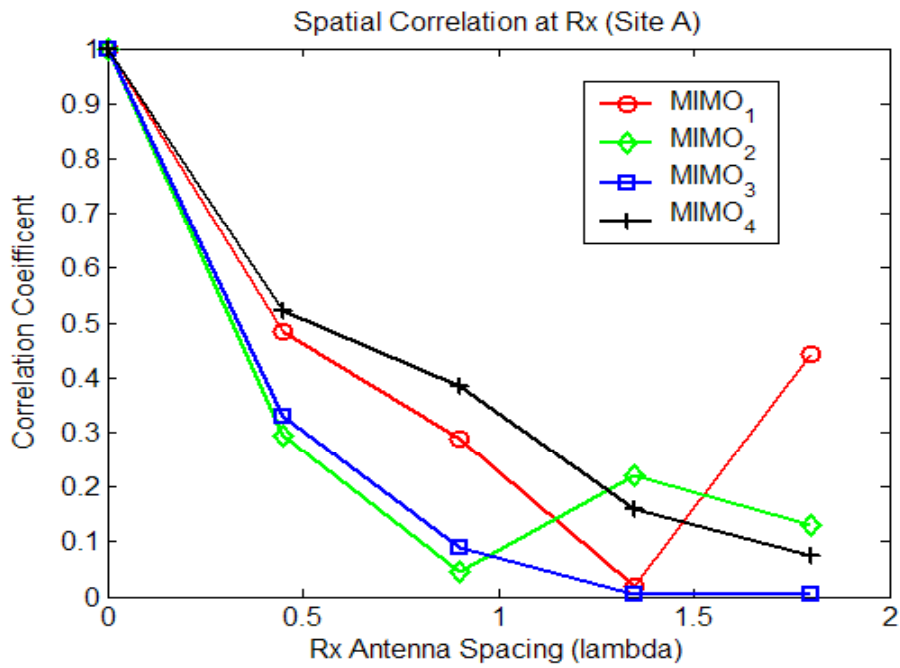


Fig. 5-8 Spatial correlation coefficients versus receiving array spacing at Site A.

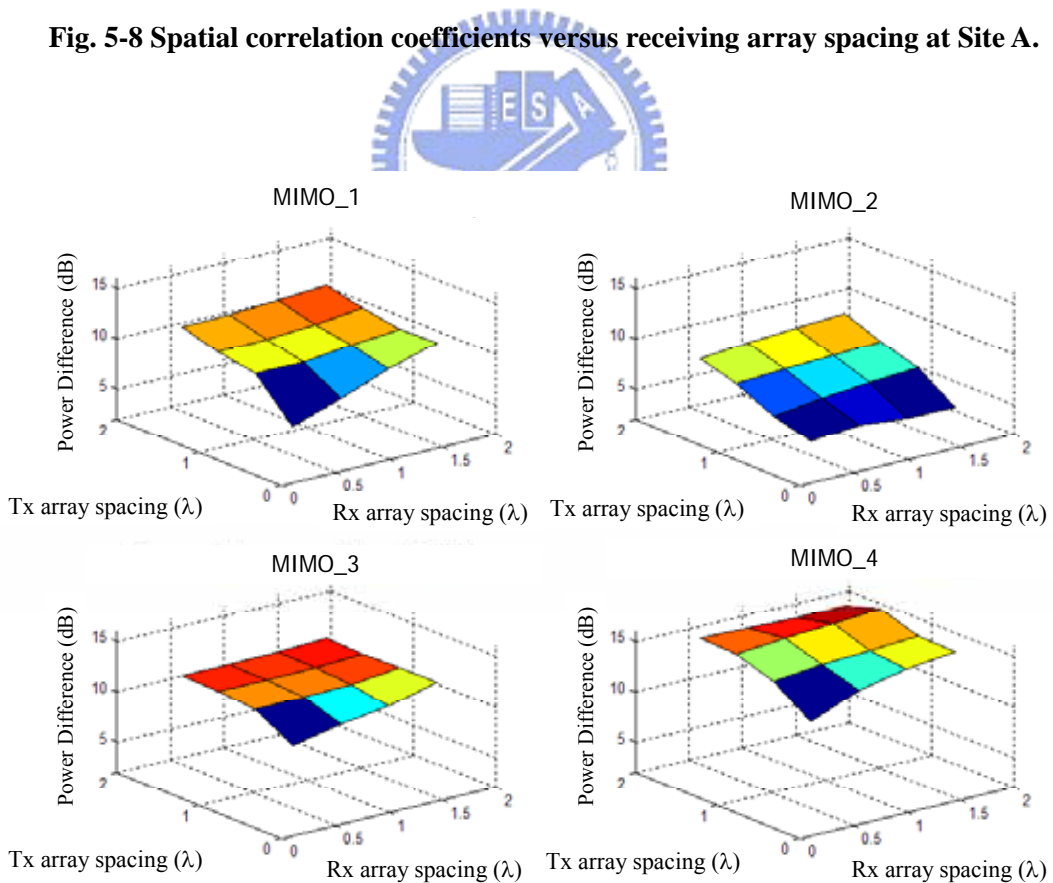


Fig. 5-9 Maximum value of the power differences between any two sub-channels versus receiving and transmitting array spacing at Site A.

---

### 5.3.4 Effect of Antenna Polarization

Fig. 5-10 shows the 2×2 MIMO channel capacity of the polar array and the spatial array at Site C. Here, the measured bandwidth is in the range of 3 to 6 GHz. The polar array is composed of two co-polarized transmitting antennas with spacing of 3 cm and two co-located cross-polarized receiving antennas. It is found that the channel capacity of the polar array is similar to that of the spatial array for MIMO\_2 and MIMO\_3 cases. However, in MIMO\_1 and MIMO\_4 cases, the channel capacity of the polar array is lower than that of the spatial array. It is because that the contribution of the cross-polarized sub-channel is insignificant due to the high cross polarization discrimination in the near-LOS condition as shown in Fig. 5-11(a) where the received power of the V/V case is much larger than that of the V/H case. However, in the NLOS situation, the cross-polarized sub-channel becomes significant due to the same order of magnitude of the multi-path components. Therefore, magnitude of the received power of the V/V case is similar to that of the V/H case, which is observed in Fig. 5-11(b). It means that, only in the NLOS conditions, the device compactness is achieved by using the polar array without sacrifice of channel capacity compared to the spatial array.

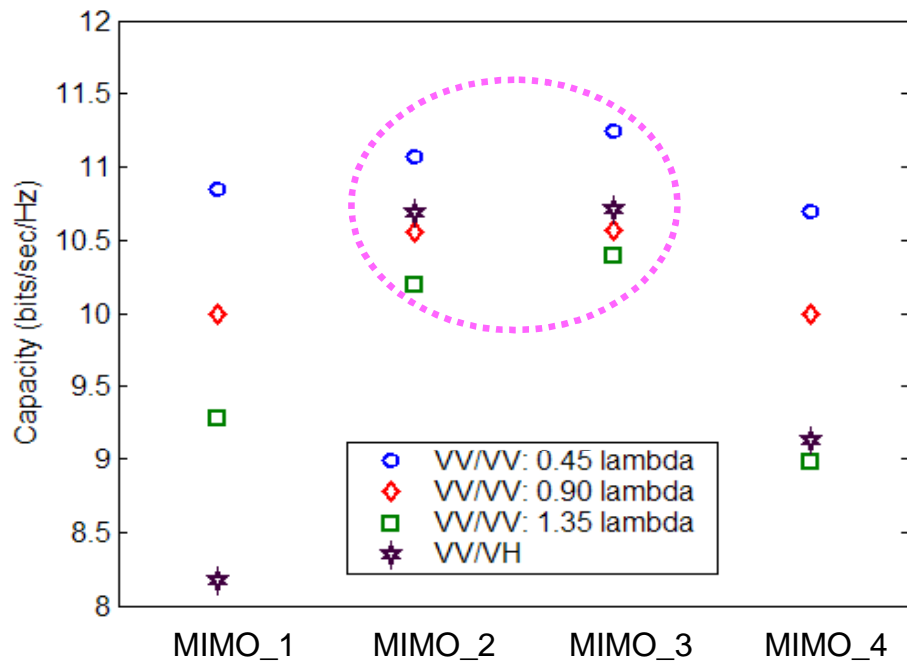
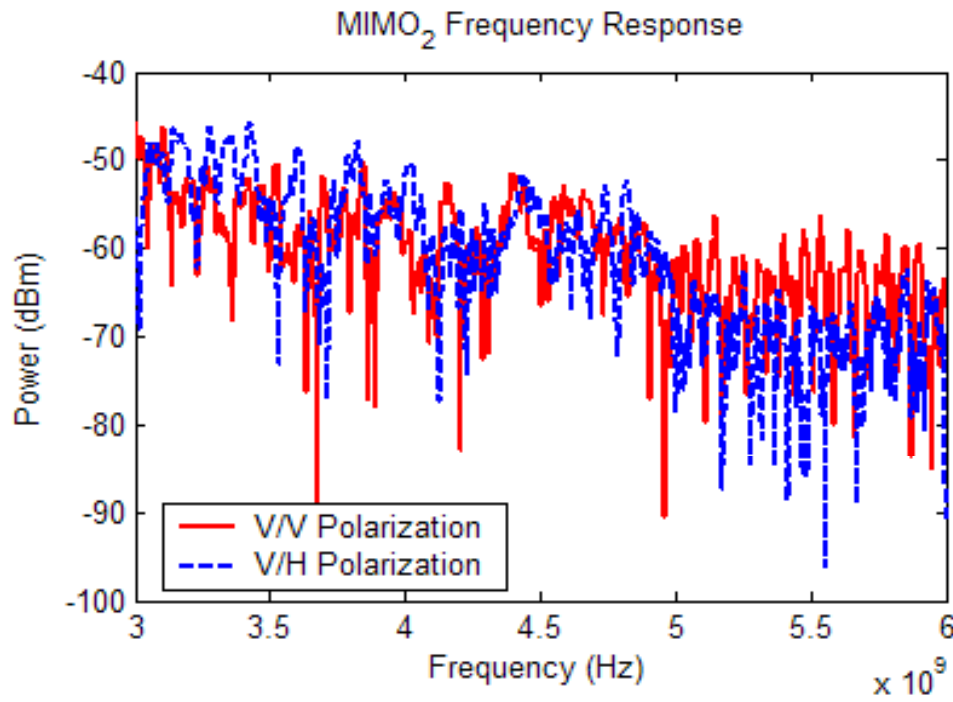
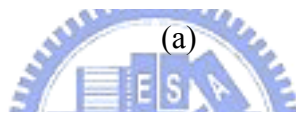
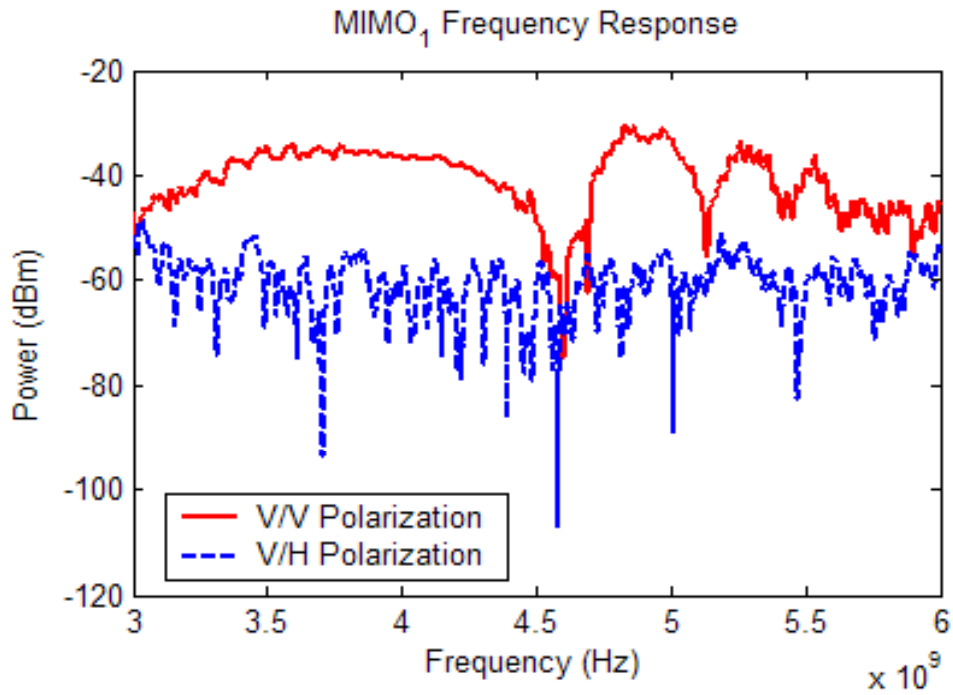


Fig. 5-10 The measured 2x2 MIMO channel capacity of the polar array and the spatial array at Site C.





(b)

**Fig. 5-11** Received power of V/V or V/H link versus frequency at Site C for (a) MIMO<sub>1</sub> (LOS); and (b) MIMO<sub>2</sub> (NLOS).



---

## 5.4 Summary

The key finding here is to that in BAN the MIMO channel capacity is mainly determined by the power imbalance between sub-channels compared to the sub-channel correlation. For spatial array, the measured results show that the MIMO channel capacity is decreased when the array spacing is increased, despite the spatial correlation coefficient is decreased. This phenomenon is different from that in WAN and WLAN. It is because that power difference among elements of the spatial array is significant in BAN short-range communications compared to that in WAN and WLAN. For polar array, the achievable channel capacity is lower than that of the spatial array in LOS conditions, which is due to high cross-polarization discrimination. However, the device compactness is achieved by using polar array without sacrifice of channel capacity compared to spatial array in NLOS conditions. Furthermore, the MIMO channel capacity is slightly dependent on the environments due to dominance of human body effect. It is also found that the MIMO channel capacity decreased with frequency or bandwidth.

---

## **Chapter 6    Conclusions**

**Summary of this paper are presented in this Chapter.**



---

## Conclusions

UWB/wideband-MIMO is the major technology for B3G wireless communication systems. In this research, the bandwidth-space-polarization characterizations of UWB/wideband MIMO channels are investigated. By understanding the channel characteristics, we developed novel methods for UWB/wideband MIMO channel modeling.

In Chapter 3, a novel method for wideband model parameters estimation is developed. Through this method, the model parameters of a wideband signal can be determined from those of a narrowband signal. This method is validated by the measurement results of 1.95 GHz and 2.44 GHz broadband signals in metropolitan and suburban areas, and by the results of 3-5 GHz UWB signals in indoors. Here, with the help of  $\Delta$ - $K$  model that is used for multipath time-of-arrival modeling, the effect of signal bandwidth on observable multipath-clustering is investigated by exploring the relationship between  $\Delta$ , signal bin width, and  $\bar{K}$ , an index to quantify the multipath-clustering phenomenon. It is found that the signal with larger bandwidth yields finer time resolution and observes more multipath components, which leads stronger multipath-clustering. Furthermore, a stochastic model is applied to characterize the averaged power delay profile with two coefficients, the power ratio and decay constant. In addition, the amplitude fading is described by a Rician

---

distribution function. It is found that (1) the power ratio is decreased when the signal bandwidth is increased; (2) the decay constant is independent of signal bandwidth; and (3) the Rician factor is increased as the signal bandwidth is increased.

In Chapter 4, a wideband hybrid spatial channel model, which combines the site-specific specular rays with a newly 3D GBSBM for scattering rays, is presented. Here, the 3D GBSBM is extended from a 2D model, which combines the concept of the GBSBCM and the GSBEM. The GSBEM is used to determine the region of scatterers for different delay-taps, and then the effective scatters located near the transmitting and receiving antennas are modeled by the GBSBCM. In the 3D GBSBM, the effect of 3D multipath on sub-channel correlation of the spatial/polar arrays is taken into account. It is noted that 3D propagations is significant to the receiving power and sub-channel correlations especially for indoor environments. From the comparisons between measured and simulated space correlation, it is found that the 3D GBSBM gives more reasonable results compared to the 2D GBSBM for both the co-polarized and the cross-polarized antenna cases.

In Chapter 5, performance of UWB-MIMO in BANs is investigated through measurements for both spatial and polar antenna arrays. In our experiments, channel frequency responses were measured in the frequency ranges of 3-10 GHz that covers the whole UWB band. The key finding here is to that in BAN the MIMO channel capacity is

---

mainly determined by the power imbalance between sub-channels compared to the sub-channel correlation. For spatial array, the measured results show that the MIMO channel capacity is decreased when the array spacing is increased, despite the spatial correlation coefficient is decreased. This phenomenon is different from that in WAN and WLAN. It is because that power difference among elements of the spatial array is significant in BAN short-range communications compared to that in WAN and WLAN. For polar array, the achievable channel capacity is lower than that of the spatial array in LOS conditions, which is due to high cross-polarization discrimination. However, the device compactness is achieved by using polar array without sacrifice of channel capacity compared to spatial array in NLOS conditions. Furthermore, the MIMO channel capacity is slightly dependent on the environments due to dominance of human body effect. It is also found that the MIMO channel capacity decreased with frequency or bandwidth.

---

## References

- [1] ITU-R PDNR, "Vision framework and overall objectives of the future development of IMT-2000 and of systems beyond IMT-2000," June 2002.
- [2] 3GPP, "Requirements for evolved UTRA and evolved UTRAN," described in TR 25.913 V7.3.0, Mar. 2006.
- [3] 3GPP, "Physical Layer Aspects of UTRA High Speed Downlink Packet Access," described in TR 25.848 V4.0.0, Mar. 2001.
- [4] FCC "Revision of Part 15 of the Commission's Rules Regarding Ultra-Wideband Transmission Systems," First Report and Order, ET Docket 98-153, FCC 02-48, Apr. 2002.
- [5] H. Suzuki, "A Statistical Model for Urban Radio Propagation," *IEEE Transactions on Communications*, vol. COM-25, no. 7, pp. 673-680, July 1977.
- [6] A. Saleh and R. Valenzuela, "A Statistical Model for Indoor Multipath Propagation," *IEEE Journal on Selected Areas in Communications*, vol. SAC-5, no. 2, pp. 128-137, Feb. 1987.
- [7] IEEE 802.11, "IEEE P802.11 TGn Channel Models", described in document IEEE 802.11-03/940r4, May 2004.
- [8] 3GPP, "Spatial channel model for multiple-input multiple-output simulations," described in document 3GPP TR 25.996 v6.1.0, Sep. 2003.
- [9] M. Steinbauer, A. F. Molisch, and E. Bonek, "The Double-Directional Radio Channel," *IEEE Magazine in Antennas and Propagation*, vol. 43, no. 4, pp. 51-63, Aug. 2001.
- [10] A. F. Molisch, H. Asplund, R. Heddergott, M. Steinbauer, and T. Zwick, "The COST 259 Directional Channel Model – Part I: Overview and Methodology," *IEEE Transaction on Wireless Communication*, vol.5, no. 12, pp. 3421-3433, 2006.
- [11] H. Hashemi, "Impulse Response Modeling of Indoor Radio Propagation Channels," *IEEE Journal on Selected Areas in Communications*, vol. 11, no. 7, pp. 967-978, Sep. 1993.
- [12] H. Asplund, A. F. Molisch, M. Steinbauer, and N. B. Mehta, "Clustering of Scatterers in Mobile Radio Channels - Evaluation and Modeling in the COST259 Directional

- 
- Channel Model,” *ICC 2002*, vol. 2, pp. 901-905, Apr. 2002.
- [13] H. Suzuki, “A Statistical Model for Urban Radio Propagation,” *IEEE Transactions on Communications*, vol. COM-25, no. 7, pp. 673-680, July 1977.
- [14] R. J.-M. Cramer, R. A. Scholtz, and M. Z. Win, “Evaluation of an Ultra-Wide-Band Propagation Channel,” *IEEE Transactions on Antennas and Propagation*, vol.50, no.5, pp. 561-570, May 2002.
- [15] Q. H. Spencer, B. D. Jeffs, M. A. Jensen, and A. L. Swindelhurst, “Modeling the Statistical Time and Angle of Arrival Characteristics of an Indoor Multipath Channel,” *IEEE Journal on Selected Areas in Communications*, vol. 18, pp. 347-360, Mar. 2000.
- [16] IEEE P802.15, “Channel Modeling Sub-committee Report Final,” described in document IEEE P802.15-02/490r1-SG3a, Feb. 2003.
- [17] K.-H. Li, M. A. Ingram, and A. V. Nguyen, “Impact of Clustering in Statistical Indoor Propagation Models on Link Capacity,” *IEEE Transactions on Communications*, vol. 50, pp. 521-523, Apr. 2002.
- [18] G. L. Turin, F. D. Clapp, T. L. Johnston, S. B. Fine and D. Lavry, “A Statistical Model of Urban Multipath Propagation,” *IEEE Transactions on Vehicular Technology*, vol. VT-21, no. 1, pp. 1-9, Feb. 1972.
- [19] G. L. Turin, W. S. Jewell and T. L. Johnston, “Simulation of Urban Vehicle-Monitoring Systems,” *IEEE Transactions on Vehicular Technology*, vol. VT-21, no. 1, pp. 9-16, Feb. 1972.
- [20] R. Ganesh and K. Pahlavan, “Statistical Modelling and Computer Simulation of Indoor Radio Channel,” *IEE Proceedings-I*, vol. 138, no. 3, pp. 153-161, June 1991.
- [21] H. Hashemi, “Simulation of the Urban Radio Propagation Channel,” *IEEE Transactions on Vehicular Technology*, vol. VT-28, no. 3, pp. 213-225, Aug. 1979.
- [22] J. C. Sperandio and P. G. Flikkema, “Discrete-time Markov Models for Path Delays in Multipath Channels,” *IEEE International Conference on Universal Personal Communications*, vol. 1, pp. 81-85, Sep. 1996.
- [23] W. C. Y. Lee, *Mobile Communications Engineering*. McGraw Hill Publications, NY, 1982.
- [24] D. Aszety, “On Antenna Arrays in Mobile Communication Systems: Fast Fading and GSM Base Station Receiver Algorithm,” *Ph.D. Dissertation*, Royal Institute of Technology, Stockholm, Sweden, Mar. 1996.

- 
- [25] J. William C. Jakes, ed., *Microwave Mobile Communications*, New York: John Wiley & Sons, 1974.
- [26] R. B. Ertel, "Statistical Analysis of the Geometrically Based Single Bounce Channel Models," unpublished notes, May 1997.
- [27] J. C. Liberti, "Analysis of CDMA Cellular Radio Systems Employing Adaptive Antennas," *Ph.D. dissertation*, Virginia Polytechnic Institute and State University, Sep. 1995.
- [28] J. C. Liberti and T. S. Rappaport, "A Geometrically Based Model for Line of Sight Multipath Radio Channels," *IEEE Veh. Technol. Conf.*, pp. 844-848, Apr. 1996.
- [29] J. P. Kermoal, L. Schumacher, and P.E. Mogensen, "Channel Characterization", *IST-2000-30148 I-METRA-WP2-D2*, v1.2, Oct. 2002.
- [30] J. P. Kermoal, "Measurement, Modeling and Performance Evaluation of the MIMO Radio Channel," *Ph.D. dissertation*, Aalborg University, Denmark, Aug. 2002.
- [31] J. P. Kermoal, L. Schumacher, P.E. Mogensen and K.I. Pedersen, "Experimental investigation of correlation properties of MIMO radio channels for indoor picocell scenario," in *Proc. IEEE Veh. Technol. Conf.*, Boston, USA, vol. 1, pp. 14-21, Sep. 2000.
- [32] L. Schumacher, K. I. Pedersen, and P.E. Mogensen, "From antenna spacings to theoretical capacities – guidelines for simulating MIMO systems," in *Proc. PIMRC Conf.*, vol. 2, pp. 587-592, Sep. 2002.
- [33] J. Salz and J.H. Winters, "Effect of fading correlation on adaptive arrays in digital mobile radio," *IEEE Trans. Veh. Technol.*, vol. 43, pp. 1049-1057, Nov. 1994.
- [34] F. Zhu, Z. Wu and C. R. Nassar, "Generalized Fading Channel Model with Application to UWB," *IEEE Conference on Ultra Wideband Systems and Technologies*, pp. 13-17, May 2002.
- [35] D. Cassioli, M. Z. Win, and A. F. Molisch, "A Statistical Model for the UWB Indoor Channel," *IEEE VTC 2001-Spring*, vol. 2, pp. 1159-1163, May 2001.
- [36] J. D. Parsons, "The Mobile Radio Propagation Channel," Pentech Press Publishers, London, 1992.
- [37] R. S. Thomä, D. Hampicke, A. Richter, G. Sommerkom, A. Schneider, U. Trautwein, and W. Wirnitzer, "Identification of time-variant directional mobile radio channels," *IEEE Transactions on Instrumentation and Measurement*, vol. 49, no. 2, pp. 357-364,



---

Apr. 2000.

- [38] R. Ganesh and K. Pahlavan, "On the Modeling of Fading Multipath Indoor Radio Channels," *IEEE GLOBECOM'89*, vol. 3, pp. 1346-1350, Nov. 1989.
- [39] N. Blaunstein and J. B. Anderson "Multipath Phenomena in Cellular Networks," Artech House Publishers, London, 2002.
- [40] J. S. K. Raj, A. S. Prabu, N. Vikram and J. Scheobel, "Spatial Correlation and MIMO Capacity of Uniform Rectangular Dipole Arrays," *IEEE Antennas and Wireless Propagation Letters*, vol.7, pp. 97-100, 2008.
- [41] M. Shafi, M. Zhang, P. J. Smith, A. L. Moustakes and A. F. Molisch, "The Impact of Elevation Angle on MIMO Capacity," *Proc. IEEE ICC*, pp. 4155-4160, 2006.
- [42] B. Gyselinckx, C. Van Hoof, S. Donnay, "Body area networks, the ascent of autonomous wireless microsystems," in *International Symposium on Hardware Technology Drivers of Ambient Intelligence*, 2004.
- [43] A. J. Paulraj, D. A. Gore, R. U. Nabar, and H. Bölcskei, "An overview of MIMO communications – A key to gigabit wireless," *Proceedings of the IEEE*, vol. 92, no. 2, pp. 198-218, 2004.
- [44] D. Neiryneck, C. Williams, A. Nix and M. Beach, "Exploiting multiple- input multiple-output in the personal sphere," *IET Microw. Antennas Propag.*, vol. 1, no. 6, pp. 1170-1176, 2007.
- [45] S. V. Roy, C. Oestges, F. Horlin and Ph. De Doncker, "Ultra-wideband spatial channel characterization for body area networks," *The second European conference on Antennas and Propagation*, pp.1-5, 2007.
- [46] C. W. Lin, W. H. Lo, R. H. Yan, and S. J. Chung, "Planar Binomial Curved Monopole Antennas for Ultra-Wideband Communication," *IEEE Trans. on Antennas and Propagation*, vol. 55, no. 9, Sep. 2007.
- [47] A. F. Molisch, M. Steinbauer, M. Toeltsch, E. Bonek and R. S. Thoma, "Capacity of MIMO systems based on measured wireless channels," *IEEE Journal on Selected Areas in Communications*, vol. 20, no. 3, pp. 561-569, 2002.

---

## Author's Publications (2003~2008)

### A. Journal

1. Wei-Ju Chang and Jenn-Hwan Tarng, "Effects of Bandwidth on Observable Multipath Clustering in Outdoor/Indoor Environments for Broadband and Ultra-Wideband Wireless Systems," *IEEE Transactions on Vehicular Technology*, vol. 56, no.4, pp. 1913-1923, July 2007.
2. Wei-Ju Chang and Jenn-Hwan Tarng, "Bandwidth Effects – A Validation Study of the Spatial Channel Model Extension (SCME) for 3GPP Long-Term Evolution and IEEE 802.16e Technologies," *International Journal of Electrical Engineering*, vol. 15, no. 1, pp. 9-15, February 2008.
3. Wei-Ju Chang, Jenn-Hwan Tarng and Szu-Yun Peng, "Frequency-Space-Polarization on UWB MIMO Performance for Body Area Network Applications," *IEEE Antenna and Wireless Propagation Letters* (to be published)
4. Wei-Ju Chang, Jenn-Hwan Tarng and Ming-Jiun Shen, "Recursive Determination of the Bandwidth Dependent Parameters of a Modified Cassioli-Win-Molisch Ultra-Wideband Indoor Radio Channel Model," *IEEE Transactions on Wireless Communications* (in revise)

### B. Conference

5. Wei-Ju Chang and Jenn-Hwan Tarng, "Effect of radio bandwidth on multipath clustering," *IEEE Vehicular Technology Conference 2003-Sprint*, March 2003.
6. Wei-Ju Chang and Jenn-Hwan Tarng, "A Novel Method to Estimate Time-of-Arrival of Broadband Signal Propagation in Outdoor Environment," *presented in COST273*, Czech, September 2003.
7. Wei-Ju Chang and Jenn-Hwan Tarng, "A Novel TOA Estimation Method of Broadband Signal Propagation in Outdoor Environment," *IEEE Vehicular Technology Conference 2004-Spring*, March 2004.
8. Wei-Ju Chang and Jenn-Hwan Tarng, "Investigation on Radio Bandwidth Dependency of UWB Indoor Channels," *presented in COST273*, Sweden, June 2004.

- 
9. Jenn-Hwan Tarng, Wei-Ju Chang and Ming-Jiun Shen, “Radio Bandwidth on Indoor UWB Channel Response”, *2004 International Conference on Electromagnetic Applications and Compatibility*, October 2004.
  10. Jenn-Hwan Tarng, Wei-Ju Chang and Ming-Jiun Shen, “Bandwidth Dependency of Ultra-Wideband Indoor Radio Channel Parameters,” *Asia Pacific Symposium of EMC Taipei 2005*, December 2005.
  11. Wei-Ju Chang and Jenn-Hwan Tarng, “Characterization of Wideband Spatio-Temporal Radio Channels for Beyond-3G Systems,” *2006 Cross strait Tri-regional Radio Science and Wireless Technology Conference*, November 2006.

